

## Non-spherical bubble dynamics in a compressible liquid

Q. X. Wang\* & J. R. Blake

School of Mathematics, the University of Birmingham, B15 2TT, United Kingdom

\*wangqx@bham.ac.uk

### ABSTRACT

In this paper, an approximate theory is developed for non-linear and non-spherical bubbles in a compressible liquid by using the method of matched asymptotic expansions. The perturbation is performed to second-order in terms of a small parameter, the bubble-wall Mach number. The inner flow near the bubble can be approximated as incompressible leading to the use of Laplace's equation, whereas the outer flow far away from the bubble can be described by the linear wave equation. A modified boundary integral method is developed to obtain the evolving bubble shapes. The numerical model agrees well with the Herring equation for spherical bubbles. Numerical analyses are further performed for non-spherical oscillating acoustic bubbles.

### 1. INTRODUCTION

Cavitation bubble dynamics has been studied extensively for about a century. Traditional research activities on violent bubble dynamics have generally been associated with cavitation on ship propellers, fluid machinery and piping systems, as well as underwater explosions. They continue to remain as important application areas.

Recent research on micro-cavitation bubbles subjected to ultrasound plays a key role in numerous medical procedures, including sonoporation and ultrasound lithotripsy. It also has major applications in industrial aqueous systems, including ultrasonic cleaners and processors, environmental remediation or enhanced crystallization.

We are concerned with the modelling of cavitation in a liquid subjected to an acoustic wave. In this phenomenon, the compressibility of liquid should be considered for describing the propagation of an acoustic wave, since the more commonly used incompressible formulation neglects the finite speed of propagation of the pressure wave. In addition, we know from spherical bubble studies that admitting compressibility into the Rayleigh-Plesset equation alters the peak internal pressures.

Spherical bubbles in compressible fluids was first considered in connection with an underwater explosion [1]. Keller [2] later formulated an equation for a spherical bubble using the wave equation and incompressible Bernoulli equation.

Prosperetti & Lezzi [3] studied spherical bubbles in compressible fluids using matched asymptotic expansions to the second-order in terms of the bubble-wall Mach number. They found a one-parameter family of equations to describe this motion. This one-parameter family of equations includes the well-known Herring and Keller equations. They [4] further carried out the third-order analysis for the problem. It was noticed that the second-order correction to the incompressible results captures to a large extent the effect of compressibility, with the next term having only a minor influence.

In this paper non-spherical bubble dynamics in a compressible liquid is studied. The fluid domain is divided into the inner region near the bubble and the outer region far away from the bubble. A weakly compressible theory is developed using matched asymptotic expansions. A modified boundary integral method is developed to obtain the evolving bubble shapes.

### 2. Mathematical formulation

Consider a cavitation bubble with typical radius of  $O(\mu\text{m})$  in an acoustic wave due to high frequency ultrasound  $O(10^{2-3})$  kHz. In this situation, the bubble dynamics can be modelled approximately based on potential flow theory. We assume that the bubble radius is small compared to the wavelength of the acoustic wave. The wavelength  $\lambda$  is  $\lambda=c/f \geq 10\text{mm}$ , when the acoustic frequency  $f \leq 150\text{kHz}$ , where  $c$  is the sound speed in water ( $c=1500\text{m/s}$ ).

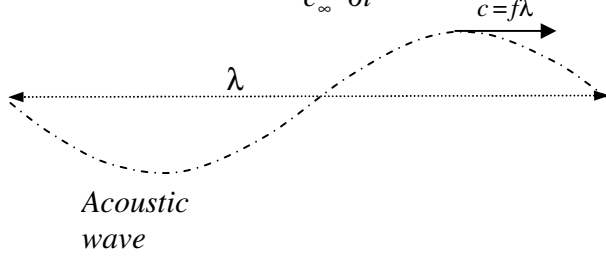
The reference length  $R_s$  is chosen as the equilibrium radius of the bubble, the reference density  $\rho_\infty$  is the density in the undisturbed liquid, and the reference pressure  $p_\infty$  is the pressure in the undisturbed liquid, often taken to be atmospheric pressure. We use the reference velocity  $U = \sqrt{p_\infty / \rho_\infty}$ , as the driving pressure is normally measured as fractions or multiples of atmospheric pressure. We thus introduce the following non-dimensional quantities, indicated by asterisks,

$$\mathbf{r} = R_s \mathbf{r}^*, \quad t = \frac{R_s}{U} t^*, \quad \varphi = R_s U \varphi^*, \quad (2.1a, b, c)$$

**Outer region:**

Scale:  $(x, y, z) = O(\lambda)$

Governing eq.:  $\nabla^2 \phi - \frac{1}{c_\infty^2} \frac{\partial^2 \phi}{\partial t^2} = 0$



**Inner region:**

Scale:  $(x, y, z) = O(R_s)$

Governing eq.:  $\nabla^2 \phi = 0$

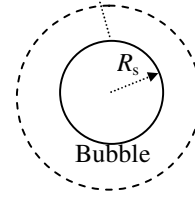


Figure 1. A representation of the weakly compressible model for a micro-cavitation bubble subjected to a plane acoustic wave, with speed of sound  $c_\infty$  and the wavelength  $\lambda$  being much larger than the equilibrium radius of the bubble  $R_s$ .

$$c = c_\infty c_*, \quad p = p_\infty (1 + p_*). \quad (2.1d, e)$$

Here  $\phi$  is the velocity potential. The sound speed  $c$  is normalized by its value at the undisturbed liquid  $c_\infty$ . In the following discussion we refer to dimensionless quantities unless specified otherwise.

A Cartesian-coordinate system is chosen, with the origin at the centre of the bubble at  $t_*=0$ , and the  $z_*$ -axis is along the direction of the acoustic wave. The liquid flow is governed by the equation of mass conservation,

$$\nabla_*^2 \phi_* + \frac{\epsilon^2}{c_*^2} \left( \frac{\partial h_*}{\partial t_*} + \nabla_* \phi_* \cdot \nabla_* h_* \right) = 0, \quad (2.2a)$$

and the Bernoulli equation,

$$\frac{\partial \phi_*}{\partial t_*} + \frac{1}{2} |\nabla_* \phi_*|^2 + h_* = 0. \quad (2.2b)$$

Here the parameter,

$$\epsilon = \frac{U}{c_\infty}, \quad (2.3)$$

is the bubble wall Mach number, which is assumed to be small in the present study. The small parameter  $\epsilon$  can also be interpreted as the ratio of the typical scale of the bubble radius  $R_s$  over the wavelength  $\lambda$  of the acoustic wave.

We assume that thermal effects in the liquid itself are insignificant. The sound speed  $c_*$  and enthalpy  $h_*$  of the liquid can be given approximately as follows,

$$c_*^2 = 1 + \epsilon^2 (n-1) h_*. \quad (2.4a)$$

$$h_* = p_* - \frac{1}{2} \epsilon^2 p_*^2 + o(\epsilon^2). \quad (2.4b)$$

Substituting (2.4) into (2.2) yields

$$\nabla_*^2 \phi_* + \frac{\epsilon^2}{c_*^2} \left( \frac{\partial p_*}{\partial t_*} + \nabla_* \phi_* \cdot \nabla_* p_* \right) = O(\epsilon^4), \quad (2.5a)$$

$$\frac{\partial \phi_*}{\partial t_*} + \frac{1}{2} |\nabla_* \phi_*|^2 + p_* = O(\epsilon^2). \quad (2.5b)$$

The kinematic material boundary condition on the bubble surface is,

$$\frac{d\mathbf{r}_*}{dt_*} = \nabla_* \phi_* \quad \text{on } S. \quad (2.6)$$

Assuming that the expansion and contraction of the bubble gas is adiabatic, the liquid pressure  $p_L$  on the bubble surface is given by,

$$p_{L*} = p_{v*} + p_{g0*} \left( \frac{V_{0*}}{V_*} \right)^\gamma - \sigma_* \left( \frac{1}{R_{1*}} + \frac{1}{R_{2*}} \right), \quad (2.7)$$

where  $p_{v*}$  is the partial pressure of vapour of the bubble,  $p_{g0*} = p_{g0}/p_\infty$  is the equilibrium partial pressure of the non-condensable gas content of the bubble;  $V_*$  is the bubble volume and  $V_{0*}$  is its initial value, and  $\gamma$  is the ratio of the specific heats of the gas content;  $R_{1*}$  and  $R_{2*}$  are the principal radii of curvature and  $\sigma_* = \sigma/(R_s P_\infty)$  is the surface tension coefficient.

Assuming the acoustic wave is a plane propagating wave along the  $z_*$ -axis, yields the condition at infinity of

$$\phi|_{r_* \rightarrow \infty} = \phi_{a*} = f_*(\omega_* t_* - k_* z_*) + g_*(\omega_* t_* + k_* z_*). \quad (2.8)$$

where the wave number  $k_*$  and frequency  $\omega_*$  of the acoustic wave can be obtained from their corresponding dimensional values  $k$  and  $\omega$ , respectively,  $k_* = R_s k$ ,  $\omega_* = R_s \omega / U$ . For a travelling harmonic plane wave, we have

$$\varphi_*|_{r_* \rightarrow \infty} = f(k_* z_* - \omega_* t_*) = b_* \cos(k_* z_* - \omega_* t_* + \theta_0). \quad (2.9)$$

### 3. Matched asymptotic expansion

The inner region near the bubble where  $(x, y, z) = O(R_s)$ , and the outer region far away from the bubble where  $(x, y, z) = O(\lambda)$ , are illustrated in figure 1. The inner expansions for the potential  $\varphi_*$  and pressure  $p_*$  are as follows,

$$\varphi_*(\mathbf{r}_*, t_*) = \varphi_0(\mathbf{r}_*, t_*) + \varepsilon \varphi_1(\mathbf{r}_*, t_*) + \dots, \quad (3.1a)$$

$$p_*(\mathbf{r}_*, t_*) = p_0(\mathbf{r}_*, t_*) + \varepsilon p_1(\mathbf{r}_*, t_*) + \dots. \quad (3.1b)$$

Substitution of (3.1) into (2.5a, b) yields the inner field equations,

$$\nabla_*^2 \varphi_i = 0 \quad \text{for } i = 0, 1. \quad (3.2)$$

The general solutions of Laplace's equation (3.2) are given as follows,

$$\begin{aligned} \varphi_i(\mathbf{r}_*, t_*) &= f_i(t_*) + g_i(t_*) z_* \\ &+ \int_S \left( \frac{\partial \varphi_i(\mathbf{q}, t_*)}{\partial n} G(\mathbf{r}_*, \mathbf{q}) - \varphi_i(\mathbf{q}, t_*) \frac{\partial G(\mathbf{r}_*, \mathbf{q})}{\partial n} \right) dS(\mathbf{q}) \end{aligned} \quad \text{for } i=0, 1, \quad (3.3)$$

where the unknown functions  $f_i(t_*)$ ,  $g_i(t_*)$  for  $i = 0, 1$  are to be determined by the matching between the inner and outer expansions;  $S$  is the bubble surface,  $\mathbf{n}$  is the unit outward normal on the surface,  $\mathbf{q}$  is the integration variable on the bubble surface  $S$ , and the free space Green's function is

$$G(\mathbf{r}_*, \mathbf{q}) = \frac{1}{4\pi} \frac{1}{|\mathbf{r}_* - \mathbf{q}|}. \quad (3.4)$$

The outer limit of the two lowest order inner solutions is as follows,

$$\begin{aligned} (\varphi_*)^o &= (\varphi_0)^o + \varepsilon (\varphi_1)^o \\ &= f_0(t_*) + g_0(t_*) z_* + \frac{1}{4\pi} \frac{m_0(t_*)}{r_*} + \varepsilon f_1(t_*) + \varepsilon g_1(t_*) z_* + O(\varepsilon^2), \end{aligned} \quad (3.5)$$

where

$$m_0(t_*) = \int_S \frac{\partial \varphi_0(\mathbf{q}, t_*)}{\partial n} dS(\mathbf{q}). \quad (3.6)$$

Denoting the outer expansions in terms of the outer variable  $\tilde{\mathbf{r}} = \varepsilon \mathbf{r}_*$  as follows,

$$\varphi_* = \varphi_0(\tilde{\mathbf{r}}, t_*) + \varepsilon \varphi_1(\tilde{\mathbf{r}}, t_*) + \dots, \quad (3.7a)$$

$$p_* = P_0(\tilde{\mathbf{r}}, t_*) + \varepsilon P_1(\tilde{\mathbf{r}}, t_*) + \dots. \quad (3.7b)$$

Substituting (3.7) into (2.5a, b) yields the equations for the two lowest order outer solutions

$$\tilde{\nabla}^2 \varphi_i - \frac{\partial^2 \varphi_i}{\partial t_*^2} = 0 \quad \text{for } i = 0, 1, \quad (3.8)$$

where the operator  $\tilde{\nabla}$  is defined in terms of  $\tilde{\mathbf{r}}$ .

The leading outer solution is the incident acoustic wave

$$\varphi_0 = f_*(\omega_*(t_* - \tilde{z})) + g_*(\omega_*(t_* + \tilde{z})). \quad (3.9)$$

The general solution of the second-order outer solution  $\varphi_1$  can be obtained as follows

$$\varphi_1 = \frac{F_1(t_* - \tilde{r})}{\tilde{r}}, \quad (3.10)$$

where  $F_1$  is an arbitrary function having a second-order derivative.

The inner limits of the two lowest order outer expansions (3.9, 3.10) can be obtained as follows,

$$\begin{aligned} (\varphi)^i &= f_*(\omega_* t_*) + g_*(\omega_* t_*) \\ &+ \varepsilon \omega_* z_* (-f_*'(\omega_* t_*) + g_*'(\omega_* t_*)) \\ &+ \frac{F_1(t_*)}{r_*} - \varepsilon F_1'(t_*) + O(\varepsilon^2). \end{aligned} \quad (3.11)$$

Using Van Dyke's matching principle (Van Dyke, 1975) with (3.5) and (3.11) yields

$$f_0(t_*) = f_*(\omega_* t_*) + g_*(\omega_* t_*), \quad (3.12a)$$

$$g_0(t_*) = 0, \quad (3.12b)$$

$$F_1(t_*) = \frac{m_0(t_*)}{4\pi}, \quad (3.12c)$$

$$f_1(t_*) = -F_1'(t_*) = -\frac{m_0'(t_*)}{4\pi}, \quad (3.12d)$$

$$g_1(t_*) = \omega_* (-f_*'(\omega_* t_*) + g_*'(\omega_* t_*)). \quad (3.12e)$$

Combining (3.9, 3.10, 3.12d) yields the first two outer solution terms,

$$\begin{aligned} \phi &= f_*(\omega_*(t_* - \tilde{z})) + g_*(\omega_*(t_* + \tilde{z})) + \varepsilon \frac{m_0(t_* - \tilde{r})}{4\pi \tilde{r}} + O(\varepsilon^2). \end{aligned} \quad (3.13)$$

The outer flow becomes a direct problem to second order. The first-order outer solution is the incident acoustic wave, and the second-order outer solution is due to a point source whose strength is equal to the rate of change of the bubble

volume.

#### 4. The theoretical basis for the computational model: second order theory

The combined two lowest order inner solutions,  $\varphi_*(\mathbf{r}_*, t_*) = \varphi_0(\mathbf{r}_*, t_*) + \varepsilon \varphi_1(\mathbf{r}_*, t_*)$ , yield the following set of equations for the potential,

$$\nabla_*^2 \varphi_* = O(\varepsilon^2), \quad (4.1a)$$

$$\frac{d\mathbf{r}_*}{dt_*} = \nabla_* \varphi_* + O(\varepsilon^2) \text{ on } S, \quad (4.1b)$$

$$\frac{\partial \varphi_*}{\partial t_*} + \frac{1}{2} |\nabla_* \varphi_*|^2 + p_{L*} = O(\varepsilon^2) \text{ on } S, \quad (4.1c)$$

$$\begin{aligned} \varphi_*|_{r_* \rightarrow \infty} &= f_0(t_*) + \varepsilon f_1(t_*) + \varepsilon g_1(t_*) z_* \\ &+ \frac{1}{4\pi} \frac{m_0(t_*)}{r_*} + O(\varepsilon^2). \end{aligned} \quad (4.1d)$$

Assuming the bubble is in an equilibrium state before the arrival of the acoustic wave, the initial condition on the bubble surface is given by,

$$\varphi_{n*}|_{t_*=0} = \varepsilon g_1(0) \mathbf{n} \cdot \mathbf{k} \text{ on } r_* = R_{0*}. \quad (4.2)$$

We choose the coordinates  $\mathbf{r}_b$  moving with a (time dependent) uniform stream at infinity, in which the flow velocity vanishes at infinity

$$t_b = t_*, \quad \mathbf{r}_b = \mathbf{r}_* + \varepsilon (f_*(\omega_* t_*) - g_*(\omega_* t_*)) \mathbf{k}. \quad (4.3)$$

In addition we make the following decomposition

$$\varphi_* = f_0(t_b) + \varepsilon f_1(t_b) + \varepsilon g_1(t_b) z_b + \Phi. \quad (4.4)$$

Substituting (4.3, 4.4) into (4.1) yields

$$\nabla_b^2 \Phi = O(\varepsilon^2), \quad (4.5a)$$

$$\frac{d\mathbf{r}_b}{dt_b} = \nabla_b \Phi + O(\varepsilon^2) \text{ on } S, \quad (4.5b)$$

$$\begin{aligned} \frac{d\Phi}{dt_b} &= 1 + \frac{1}{2} |\nabla_b \Phi|^2 \\ &- \left( p_{v*} + p_{g0*} \left( \frac{V_{0*}}{V_*} \right)^\gamma - \sigma_* \left( \frac{1}{R_{1*}} + \frac{1}{R_{2*}} \right) \right) \\ &- \omega_* (f_*'(\omega_* t_b) + g_*'(\omega_* t_b)) + \varepsilon \frac{1}{4\pi} m_0''(t_b) \\ &+ \varepsilon \omega_*^2 (f_*''(\omega_* t_b) - g_*''(\omega_* t_b)) z_b + O(\varepsilon^2), \end{aligned} \quad (4.5c)$$

$$\Phi|_{r_b \rightarrow \infty} = \frac{1}{4\pi} \frac{m_0(t_b)}{r_b} + O(\varepsilon^2), \quad (4.5d)$$

$$\Phi_{n*}|_{t_b=0} = 0 \text{ on } r_* = R_{0*}. \quad (4.5e)$$

Note (4.7) has been used in deriving (4.5c).

Using the definition  $m_0(t_*)$  in (3.6) and (4.4) leads to,

$$m_0(t_b) = \int_S \frac{\partial \Phi}{\partial n} dS + O(\varepsilon). \quad (4.6)$$

There are three additional terms associated with the acoustic wave contribution in the dynamic condition on the bubble surface (4.5c). The first term of  $O(1)$ ,  $-\omega_* (f_*'(\omega_* t_b) + g_*'(\omega_* t_b))$ , represents the local acoustic pressure at the bubble centre.

The second term,  $\varepsilon \frac{1}{4\pi} m_0''(t_b)$ , is associated with an outward propagating acoustic wave due to the bubble's oscillations. The first two terms yield only spherical wave field effects.

However, the third term,  $\varepsilon \omega_*^2 (f_*''(\omega_* t_b) - g_*''(\omega_* t_b)) z_b$ , is associated with the inertial force effect due to the acoustic wave and breaks the spherical symmetry.

The initial boundary value problem defined by (4.5) can be solved numerically using a boundary integral method (BIM) coupled with a mixed-Eulerian-Lagrangian method (MEL). The numerical model for a singly-connected bubble can be found in [5-7].

#### 5. Comparisons with previous studies

A comparison is made for the case where  $p_{g0*}=5.0$ ,  $\gamma=1.25$ ,  $R_{0*}=0.4696$ . and  $b_*=0.0$  (without an acoustic wave). The amplitude of the oscillating bubble radius reduces slightly with time, with the maximum values (peaks) of radius decreasing with time while the minimum values (troughs) increase with time. This is as expected, because acoustic wave generated by the bubble motion radiates energy to infinity with a resulting loss of energy in the bubble system. The MEL computational result agrees well with that of the KHE over four oscillations and are nearly undifferentiated.

#### 6. Analysis of bubble behaviour when subjected to a weak acoustic wave

When subjected to a weak acoustic wave, a bubble usually oscillates for many cycles in a singly connected form. Jets form at the two poles of the bubble surface during the latter stage of the bubble's lifetime, where previously the bubble is approximately spherical. We will

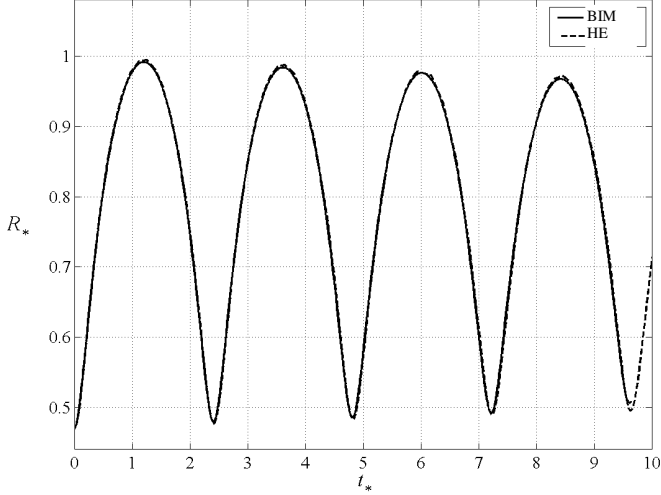


Figure 2. Comparison for dimensionless radius histories of the spherical gas bubble using the Herring equation (HE) and the boundary integral method (BIM). The parameters for the case are  $R_{0*}=0.4696$ ,  $p_{g0*}=5.0$ ,  $\gamma=1.25$  and  $b_*=0.0$ .

only describe the resonant case when the acoustic frequency equals the natural frequency of the bubble.

The case considered is characterized by  $R_{0*}=1.0$ ,  $R_{t0*}=1.0$  and  $p_{g0*}=1.0$ .  $b_*=0.1$ ,  $\omega_*=\omega_n$ , where  $\omega_n$  is natural frequency of the bubble. Figure 3a shows the histories of the bubble volume  $\frac{3}{4\pi}V_*$  and the local acoustic pressure  $p_{a*}=a_*\sin(\omega_n t_*)$ . Driven by the acoustic wave, the bubble volume oscillates with time, its phase is approximately  $\pi/2$  behind that of the acoustic pressure. The acoustic pressure is negative (a tension) when the bubble expands, and vice versa. The work done by the acoustic pressure on the internal gas is thus positive during both expansion and collapse phases, and the bubble absorbs acoustic energy continuously. As the result, the oscillation amplitude of the bubble volume increases with time monotonically and rapidly, with its maximum values (peaks) increasing with time while the minimum values (troughs) decrease.

Figure 3b shows the bubble shapes during the last (6<sup>th</sup>) collapse phase. The bubble is approximately spherical at the start of the collapse phase. Two jets are formed at the two poles at the end of this phase; with the jet in the wave direction having greater momentum.

## 7. Bubble behaviour when subjected to a strong acoustic wave

When subjected to a strong acoustic wave, a bubble oscillates for only a very few cycles in singly connected form, due to the strong inertial effect of the acoustic wave. The bubble absorbs energy rapidly from the acoustic wave,

and therefore usually undergoes a relatively long expansion phase to a large maximum volume, followed by an extensive but shorter collapse phase. A bubble jet is often formed along the wave direction towards the end of the collapse phase, developing rapidly and impacting on the opposite bubble surface in the collapse phase.

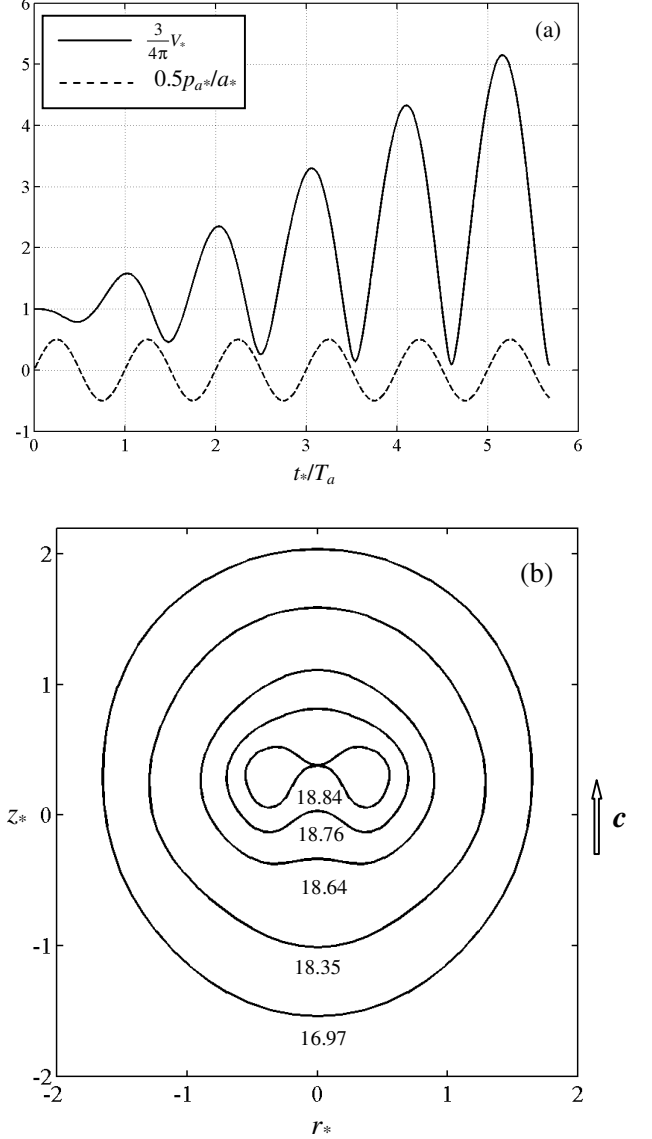


Figure 3. Time record of the acoustic bubble characterized by  $b_*=0.1$ ,  $\omega_*=\omega_n$ : (a) the bubble volume  $\frac{3}{4\pi}V_*$  and acoustic pressure at the bubble centre  $0.5p_{a*}/a_*$  (b) Bubble shapes during the last (6<sup>th</sup>) collapse phase. The direction of propagation of the wave is indicated by  $c$ .

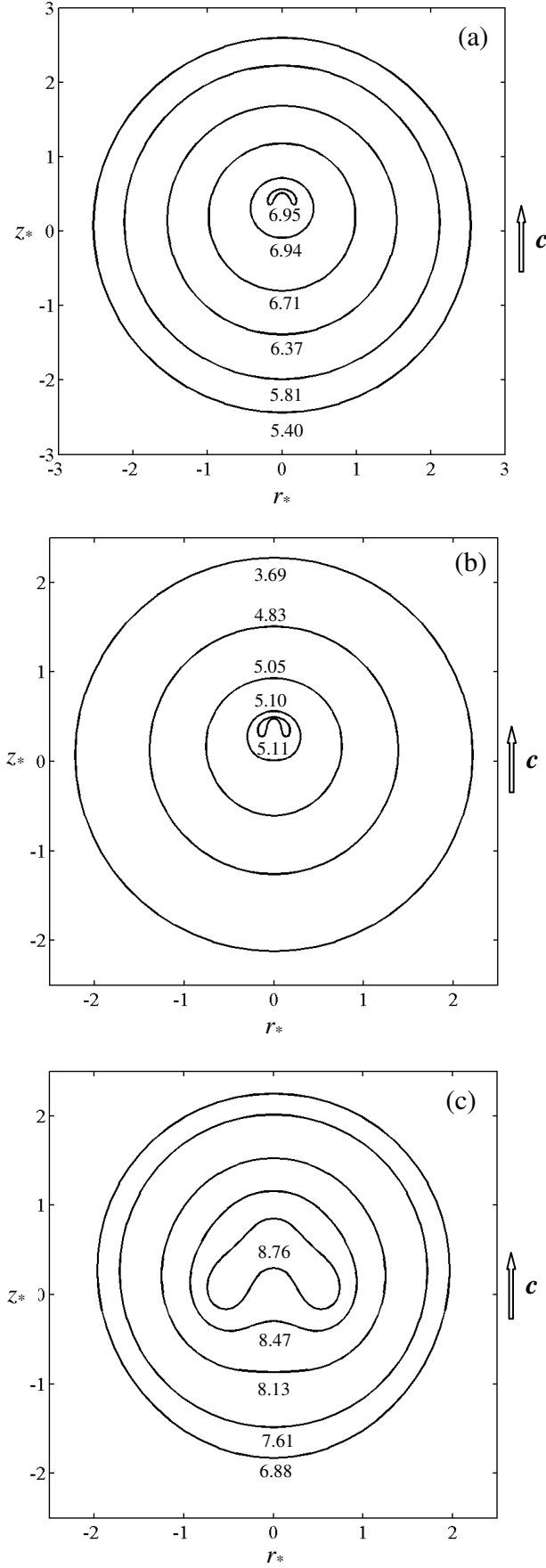


Figure 4. (a) Bubble shapes during the last collapse phase for the bubble characterized by (a)  $b^* = 1.0$ ,  $\omega^* = \omega_{n^*}$ , (b)  $b^* = 1.5$ ,  $\omega^* = 0.6667\omega_{n^*}$ , (c)  $b^* = 0.6667$ ,  $\omega^* = 1.5\omega_{n^*}$ .

As shown in Figure 4 shown the bubble shapes during (a) the third collapse phase for a sub-resonant case at  $b^* = 1.5$ ,  $\omega^* = 0.6667\omega_{n^*}$ , (b) the second collapse phase for a resonant case at  $b^* = 1.0$ ,  $\omega^* = \omega_{n^*}$ , and (c) the third collapse phase for a super-resonant case at  $b^* = 0.6667$ ,  $\omega^* = 1.5\omega_{n^*}$ . The bubble is approximately spherical shortly before the end of the collapse phase. The bottom of the bubble surface becomes flatter near the end of the collapse phase and a jet is observed to form along the wave direction. The jet velocity for the resonant case is about 600 m/s.

## 8. Summary and conclusions

Bubble dynamics caused by ultrasound waves have wide and important applications in medical ultrasonics and sonochemistry. In this study, compressible effects are incorporated into a model based on the boundary integral method, which incorporates greater physical detail into modelling bubble behaviour than previously available.

A compressible theory is developed using the method of matched asymptotic expansions. The perturbation is performed to second-order in terms of the bubble-wall Mach number, with the first-order solutions being pure incompressible flow effect and the second-order solutions linear in the Mach number. The inner flow for the first two orders near the bubble can be approximated as incompressible. The outer flow for the first two orders far away from the bubble can be described by the linear wave equation and is shown as a direct problem. Thus the non-spherical bubble dynamics in a weakly compressible liquid is modelled approximately by Laplace equation's with the compressible effects appearing only in the far field condition, which is obtained from the matching between the inner and outer expansions.

A modified boundary integral formulation associated with the mixed-Eulerian-Lagrangian method (MEL) is explored in this study. The primary advantage of this method is its computational efficiency. This model is evaluated against a spherical bubble in weakly compressible liquids; and excellent agreement is obtained with the Keller-Herring equation (KHE) for the bubble radius evolution up to four oscillations. More extensive simulations are conducted for a non-spherical oscillating bubble in a compressible liquid caused by an acoustic wave.

A series of mechanisms and features of non-spherical dynamics of acoustic cavitation bubbles have been identified in this study, which are summarized as follows.

1. Compared to the earlier incompressible flow modeling, there are three additional effects associated with the acoustic wave: (i) a local acoustic pressure at the bubble centre, (ii) an acoustic radiation term due to the acoustic

wave generated by the bubble oscillation, (iii) an inertial force effect associated with the acoustic wave. The first two effects lead to spherical wave behaviour whereas the last effect leads to non-spherical wave behaviour.

2. The inertial force effect of the acoustic wave appears out of phase with the bubble volume. It is positive when the bubble assumes a large volume and vice versa. The accumulated inertial effect is along the wave direction.

3. The bubble Kelvin impulse is generally along the wave direction with the bubble normally migrating in the same direction.

4. The time dependent shapes of acoustic bubbles depend on the strength of the acoustic wave. When subjected to a weak acoustic wave, a bubble usually oscillates for many cycles in a singly connected form. Jets form at the two poles of the bubble surface during the latter stage of the bubble's lifetime, where previously the bubble is approximately spherical.

5. Resonant oscillations occur when the acoustic frequency equals the natural frequency of the bubble. In resonant oscillations, the bubble absorbs energy from the acoustic wave almost continuously through its lifetime, and therefore the oscillation amplitude increases with time rapidly, with the maximum values (peaks) of the bubble volume also increasing with time while the minimum values (troughs) decrease. Resonant oscillations are associated with most rapid non-spherical deformation of the bubble shape.

6. When subjected to a strong acoustic wave, a bubble oscillates for only a very few cycles in singly connected form, due to the strong inertial effect of the acoustic wave. The bubble absorbs energy rapidly from the acoustic wave, and therefore usually undergoes a relatively long expansion phase to a large maximum volume, followed by an extensive but shorter collapse phase. A bubble jet is often formed along the wave direction towards the end of the collapse phase, developing rapidly and impacting on the opposite bubble surface in the collapse phase or during the early stage of the subsequent rebounding phase.

The theoretical and computational results developed in this paper for highly non-spherical bubble behaviour reveal a number of new phenomena that need to be investigated experimentally.

## References

1. Herring, C. 1941 The theory of the pulsations of the gas bubbles produced by an underwater explosion. *US Nat. Defence Res. Comm. Report*.
2. Keller, J. B. & Kolodner, I. I. 1956 Damping of underwater explosion bubble oscillations. *J. Applied Phys.* **27**(10), 1152-1161.
3. Prosperetti, A. & Lezzi, A. 1986 Bubble dynamics in a compressible liquid. Part. 1. First-order theory. *J. Fluid Mech.* **168**, 457-478.
4. Lezzi, A. & Prosperetti, A. 1987 Bubble dynamics in a compressible liquid. Part. 2. Second-order theory. *J. Fluid Mech.* **185**, 289-321.
5. Wang, Q. X., Yeo, K. S., Khoo, B. C. & Lam, K. Y. 1996b Strong interaction between buoyancy bubble and free surface. *Theoret. and Comput. Fluid Dynamics* **8**, 73-88.
6. Wang, Q. X., Yeo, K. S., Khoo, B. C. & Lam, K. Y. 1996a Nonlinear interaction between gas bubble and free surface. *Computers & Fluids* **25**(7), 607-628.
7. Wang, Q. X. & Blake, J. R. 2010 Non-spherical bubble dynamics in a compressible liquid. Part 1. Travelling acoustic wave. *J. Fluid Mech.* **659**, 191-224.

## Bubble behaviour near a two fluid interface

D.M. Leppinen\*, School of Mathematics,  
University of Birmingham

G.A. Curtiss, Numerical Algorithms Group,  
Oxford

Q. X. Wang, School of Mathematics,  
University of Birmingham

J. R. Blake, School of Mathematics,  
University of Birmingham

\*D.M.Leppinen@bham.ac.uk

### ABSTRACT

This paper investigates the behaviour of a rapidly expanding bubble in the close vicinity of a two liquid interface with a density jump, the extremes of which as the density ratio tends towards infinity and zero represent rigid boundary and free surface behaviour. Applications for this occur in industrial heterogeneous sonochemical mixing processes and in biomedical procedures such as shockwave lithotripsy, laser ablation and sonoporation. The exterior fluids are assumed incompressible, irrotational and inviscid. A boundary integral method is employed to solve the resulting equations of motions, using the vortex ring method for toroidal behaviour as proposed by Lundgren & Mansour [1]. The method is verified by comparison with existing physical and numerical experiments. The numerical treatment used herein is illustrated for a single bubble only, in both the simply connected and toroidal phases. The results demonstrate significant new features in the aspherical motions of the bubble. Results near the null Kelvin impulse state demonstrate the bubble migration and jet direction observed in the experiments of Chahine & Bovis [2] are due to the buoyancy of the cavitation bubble. Further numerical investigations examine bubble behaviour near the null impulse state for bubbles in both the denser and the lighter layer. Close standoff distance experiments illustrate the retardation of surface spiking as the ratio of densities increases. The extension to the toroidal phase of the bubble lifetime demonstrates how the threading jet will interact with the two fluid interface after impact, particularly in cases where the bubble is located in the less dense layer and the subsequent jetting is in the direction of the interface.

### NOMENCLATURE

$F$  : density weighted potential  
 $G$  : free space Green's function  
 $g$  : acceleration of gravity  
 $h$  : standoff distance  $h = z_c / R_{\max}$   
 $p$  : pressure field in liquid  
 $p_b$  : bubble pressure  
 $p_\infty$  : far field pressure

$(r, z)$  : cylindrical coordinates  
 $R_{\max}$  : maximum possible bubble size  
 $t$  : time  
 $V$  : bubble volume  
 $z_c$  : bubble centroid at  $t = 0$   
 $\mathbf{n}$  : normal vector  
 $\mathbf{u}_i$  : velocity field in layer  $i$   
 $(\mathbf{b}, \mathbf{c})$  : surface points on bubble in layer 1  
 $(\mathbf{d}, \mathbf{e})$  : surface points on bubble in layer 2  
 $(\mathbf{p}, \mathbf{q})$  : surface points on density interface  
 $(\mathbf{x}_0, \mathbf{x})$  : surface points for Green's function  
 $\Delta_p$  : pressure scale with  $\Delta_p = p_\infty - p_v$   
 $\delta$  : buoyancy parameter with  $\delta = \rho_1 g R_{\max} / \Delta_p$   
 $\gamma$  : ratio of specific heats  
 $\varepsilon$  : strength parameter with  $\varepsilon = p_0 / \Delta_p$   
 $\phi_i$  : velocity potential in layer  $i$   
 $\sigma$  : surface tension  
 $\rho_i$  : density in layer  $i$   
 $\rho$  : density ratio with  $\rho = \rho_1 / \rho_2$

### 1. INTRODUCTION

The influence of rigid and free boundaries on the dynamics of bubbles has been researched extensively, both experimentally and theoretically. Experiments by Benjamin and Ellis [3] have shown that the presence of a solid boundary caused the formation of a liquid jet through the bubble, forming a toroidal bubble. This behaviour has been observed in many other experiments since, including Brujan et al. [4], Phillip & Lauterborn [5], Tomita and Shima [6] and Lauterborn & Bolle [7]. Similar behaviour is also observed when a bubble collapses near a free surface. In such conditions bubble jetting may be directed away from the surface, with a counter-jet forming out of the free surface. Experiments using spark generated bubbles by Gibson and Blake [8] under free fall conditions and by



Chahine & Bovis [2] in standard gravity, showed this counter-jet to be greatly influenced by the standoff distance. Bubbles formed very close to the surface generate severe vertical surface spikes, and those at greater distances create much smaller and smoother deformations to the surface. Numerical investigations into both of these phenomena have been undertaken using boundary integral methods to great effect. Simply connected simulations were first carried out by Lenoir [9], Taib [10] and Blake, Taib and Doherty [11] into cavitation collapse near rigid boundaries. These results showed jet direction in the absence of gravity to be directed towards the wall, and that the expansion phase of the bubbles is of importance for the later collapse phase, in spite of the high level of sphericity observed about the maximum bubble volume. Simulations of behaviour near free surfaces were also carried out by Taib [10] and Blake, Taib and Doherty [12] with some success. More accurate implementations have since modelled pre-toroidal behaviour near free surfaces with a high degree of accuracy by Wang et al. [13], Pearson [14] and Robinson et al. [15]. This paper seeks to investigate the behaviour of high pressure cavitation bubbles in the vicinity of a two fluid interface, that is, the interface between two immiscible liquids of different densities. Where appropriate this is continued into the toroidal phase using the vortex ring method of Lundgen & Mansour [1]. Previously Klaseboer & Khoo [16] have used a boundary integral approach to examine the dynamics of a single bubble near a density interface where the authors decoupled the normal velocity of the fluid-fluid interface from the discretised matrix equations using geometrical arguments derived from the equal density case. This does not decrease the time required to calculate the Green's function block matrices, yet it does significantly decrease the size of the matrix to be inverted. Their results showed various types of behaviour in the presence of gravity, including jetting towards and away from the interface, and bubble pinching near the null impulse line, in agreement with the model presented herein. A further advancement has been presented to account for a linearly elastic fluid in the uncavitated layer, by means of a displacement parameter on the fluid-fluid interface Klaseboer & Khoo [17]. The results obtained are in agreement with experiments by Brujan et al. [18-19].

In the current work we extend the results of Klaseboer & Khoo [16] by implementing a mathematical model to examine the evolution of multiple bubbles on either side of the interface without making any unnecessary assumptions about the fluid flow. In Section 2 we introduce the mathematical model, with details of the numerical implementation given in Section 3. The model validation is briefly discussed in Section 4 and results are presented in Section 5. The overall conclusions are made in Section 6.

## 2. MATHEMATICAL MODEL

The problem we are considering is sketched in Figure 1(a) with a layer of fluid of density  $\rho_1$  underlying a layer of fluid of density  $\rho_2$  with  $\rho_1 < \rho_2$ . In each layer the fluid is assumed to be inviscid, incompressible and irrotational so that the velocity field can be written as the gradient of a potential with

$$\mathbf{u}_i = \nabla \phi_i \quad (1)$$

for  $i = 1, 2$  where

$$\nabla \cdot \mathbf{u}_i = \nabla^2 \phi_i = 0 \quad (2)$$

and

$$\nabla \times \mathbf{u}_i = \mathbf{0}. \quad (3)$$

There is at least one bubble in either the upper or lower layer, with an arbitrary number of additional bubbles. The bubble is initially spherical with a centroid a distance  $z_c$  above or below the interface. Our objective is to examine the interaction of the bubbles with the density interface and with each other.

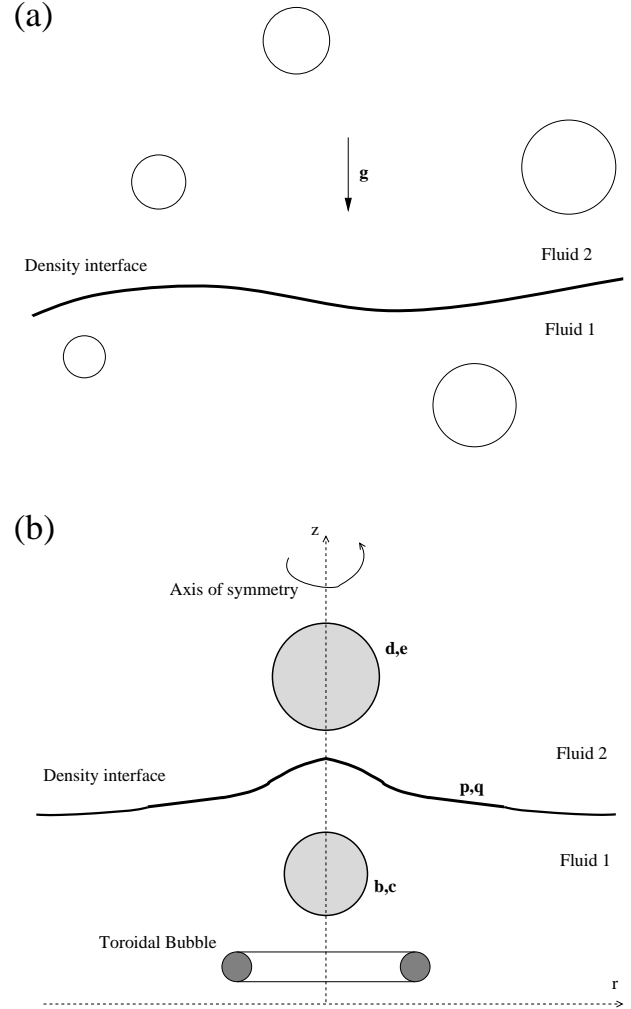


**Figure 1. (a) A Sketch of bubbles interacting with a density interface. (b) The axisymmetric geometry used in the current method.**

With the above assumptions Bernoulli's equation is valid everywhere in both exterior fluids which gives

$$\frac{\partial \phi_i}{\partial t} + \frac{|\mathbf{u}_i|^2}{2} + \frac{p}{\rho_i} + g(z - z_0) = \frac{p_\infty}{\rho_i} \quad (4)$$

where  $t$  is time,  $p$  is pressure,  $g$  is the acceleration of gravity,  $z$  is the vertical coordinate of a fluid particle with reference to

the initial vertical coordinate of the interface  $z_0$  and  $p_\infty$  is the far field pressure at  $z_0$ . The exterior fluid layers are taken as isothermal. Furthermore it is assumed that no mass or heat transfer will occur across the gas/liquid boundaries. Thus the bubble gases obey an adiabatic law. The pressure inside each bubble is given by

$$p_b = p_v + p_0 \left( \frac{V_0}{V} \right)^\gamma \quad (5)$$

where  $p_v$  represents the condensable gas vapour pressure,  $V, V_0$  are the bubble volume and initial reference volume respectively,  $p_0$  is the initial reference pressure for the bubble at reference volume and  $\gamma$  is the ratio of specific heats of the incompressible gas (taken as 1.4 in this paper).

The pressure of the surrounding liquid at the bubble surface is given by the Young-Laplace condition as

$$p = p_b - \sigma_{b,i} \nabla \cdot \mathbf{n}_b \quad (6)$$

where  $\sigma_{b,i}$  is the surface tension of a bubble in fluid  $i$  and  $\mathbf{n}_b$  is the outward pointing unit normal to the bubble.

The pressure jump across the density interface is also calculated using the Young-Laplace condition as

$$p = p_b - \sigma_I \nabla \cdot \mathbf{n}_1 \quad (7)$$

where  $\sigma_I$  is the surface tension of the density interface and  $\mathbf{n}_1$  is the unit normal pointing from fluid 1 into fluid 2. In this paper  $p_\infty$  is taken as constant, and the early bubble behaviour observed is the result of an initially high internal gas pressure,  $p_0 \gg p_v$ . This is valid for spark and laser generated bubbles, where the initial pressure may reach many thousands of atmospheres.

We proceed by nondimensionalising our equations using the following scales: the density of the lower layer,  $\rho_1$ , for density; the difference in the far field pressure and the condensable gas vapour pressure,  $\Delta_p = p_\infty - p_v$  for pressure; the maximum radius a bubble would reach in an infinite fluid of density  $\rho_1$ ,  $R_{\max}$  for length;  $R_{\max}(\rho_1 / \Delta_p)^{1/2}$  for time;  $(\Delta_p / \rho_1)^{1/2} / R_{\max}$  for potential;  $R_{\max} \Delta_p$  for surface tension. Thus along a bubble interface in fluid 1 the Bernoulli equation becomes

$$\frac{\partial \phi_1}{\partial t} + \frac{|\mathbf{u}_1|^2}{2} = 1 - \varepsilon \left( \frac{V_0}{V} \right)^\gamma - \delta(z - z_0) + \sigma_{b,1} \nabla \cdot \mathbf{n}_b \quad (8)$$

where  $\varepsilon = p_0 / \Delta_p$  and  $\delta = \rho_1 g R_{\max} / \Delta_p$  and all variables are now dimensionless.

The corresponding result in fluid 2 is

$$\frac{\partial \phi_2}{\partial t} + \frac{|\mathbf{u}_2|^2}{2} = \frac{1}{\rho} \left( 1 - \varepsilon \left( \frac{V_0}{V} \right)^\gamma - \delta(z - z_0) + \sigma_{b,2} \nabla \cdot \mathbf{n}_b \right) \quad (9)$$

where  $\rho = \rho_1 / \rho_2$ .

Along the density interface we use equations (4) and (7) to obtain

$$\left( \frac{\partial \phi}{\partial t} + \frac{|\mathbf{u}_1|^2}{2} \right) - \rho \left( \frac{\partial \phi_2}{\partial t} + \frac{|\mathbf{u}_2|^2}{2} \right) = \delta \varepsilon (1 + \rho) - \sigma_I \nabla \cdot \mathbf{n}_1 \quad (10)$$

### 3. NUMERICAL IMPLEMENTATION

The general problem consider in Figure 1(a) is fully three-dimensional. For computational convenience we consider the axisymmetric problem sketched in Figure 1(b) where **(b,c)** refer to points on a bubble surface in fluid 1, **(d,e)** refer to points on a bubble surface in fluid 2 and **(p,q)** refer to points on the interface between fluids 1 and 2. The substantial derivatives on all surfaces are given by

$$\frac{D}{Dt} = \frac{\partial}{\partial t} + \mathbf{u} \cdot \nabla, \quad (11)$$

where  $\mathbf{u} = \mathbf{u}_i$  on the bubble surface in fluid  $i$  and  $\mathbf{u} = (\mathbf{u}_1 + \mathbf{u}_2) / 2$  on the two fluid interface. Particles on the bubble surfaces and the density interface are treated as material points and are advected according to

$$\frac{d\mathbf{b}}{dt} = \mathbf{u}_1, \quad \frac{d\mathbf{d}}{dt} = \mathbf{u}_1, \quad \frac{d\mathbf{p}}{dt} = (\mathbf{u}_1 + \mathbf{u}_2) / 2. \quad (12)$$

For convenience we define

$$F = (\varphi_1 + \varphi_2)(1 - \rho) + (\varphi_1 - \varphi_2)(1 + \rho) \quad (13)$$

as the density-weighted potential along the density interface which satisfies the evolution equation

$$\frac{DF}{Dt} = (1 - \rho) \mathbf{u}_1 \cdot \mathbf{u}_2 - 2(1 + \rho) \delta \varepsilon + 2\sigma_I \nabla \cdot \mathbf{n} \quad (14)$$

Along the bubble interfaces in fluid 1 we have

$$\frac{D\phi_1}{Dt} = \frac{|\mathbf{u}_1|^2}{2} + 1 - \varepsilon \left( \frac{V_0}{V} \right)^\gamma - \delta(z - z_0) + \sigma_{b,1} \nabla \cdot \mathbf{n}_b \quad (15)$$

and along the bubble interfaces in fluid 2 we have

$$\frac{D\phi_2}{Dt} = \frac{|\mathbf{u}_2|^2}{2} + \frac{1}{\rho} \left( 1 - \varepsilon \left( \frac{V_0}{V} \right)^\gamma - \delta(z - z_0) + \sigma_{b,2} \nabla \cdot \mathbf{n}_b \right). \quad (16)$$

Our numerical procedure is as follows. We place a discrete series of nodal points **(b,d,p)** along the bubble surfaces in fluid 1 and 2, and along the density interface respectively. We then timestep (using a variable order Runge-Kutta scheme) equations (12) to update the surface locations and equations (14)-(16) to update the nodal potentials. The nodal velocities are calculated using  $\mathbf{u}_i = \nabla \phi_i$  where we use the boundary integral technique to calculate the normal gradient of the velocity potentials and splining techniques to calculate the tangential derivatives. In particular if  $\nabla^2 \phi = 0$  in some domain  $D$  with boundary  $\partial D$  then we can write

$$2\pi\varphi(\mathbf{x}_0) = \int_{\partial D} \left( G(\mathbf{x}_0, \mathbf{x}) \frac{\partial \phi(\mathbf{x})}{\partial n} - \phi(\mathbf{x}) \frac{\partial G(\mathbf{x}_0, \mathbf{x})}{\partial n} \right) dS \quad (17)$$

where  $G(\mathbf{x}_0, \mathbf{x}) = 1/|\mathbf{x}_0 - \mathbf{x}|$  is the free space Green's function and  $\frac{\partial G(\mathbf{x}_0, \mathbf{x})}{\partial n}$  is the normal derivative of the Green's function with respect to the outward normal of the fluid domain and  $\mathbf{x}_0, \mathbf{x}$  are fixed and variable points on the boundary respectively. In our implementation all of the surfaces are represented by quintic splines and are smooth. Equation (17) is appropriate in both fluid 1 and fluid 2. In fluid 1  $\partial D$  is the union of the surfaces of all bubbles located in fluid 1 and of the interface separating fluid 1 and 2. Similarly, in fluid 2  $\partial D$  is the union of the surfaces of all bubbles located in fluid 2 and of the interface separating fluid 1 and 2. The central portion of the density interface is represented using nodal points. The truncated interface is then extended to infinity using a least squares type approximation as detailed by Curtiss [20] with all integrals evaluated analytically along the infinite extension.

The procedure for discretising and solving the boundary integral equation (17) are well known and our particular implementation is discussed by Curtiss [20]. We note that we have used the vortex ring method of Lundgren and Mansour [1] to carry our integration into the toroidal bubble regime. Briefly, all quantities of interest along the central portion of the density interface and along the bubble surfaces are represented using quintic splines based upon an arclength formulation. The logarithmic singularities associated with the boundary integral method are removed analytically and all of the resultant integrals are approximated using high-order (typically 20) Gaussian quadrature. In summary, when equation (17) is discretised along each of the bubble surfaces in fluid 1 and 2, and along the density interface between the fluids, we obtain the following system of equations

$$\begin{bmatrix} G_{bc} & 0 & -G_{bq} & \frac{\rho}{1+\rho} DG_{bq} \\ 0 & G_{de} & G_{dq} & \frac{-1}{1+\rho} DG_{dq} \\ G_{pc} & G_{pe} & 0 & \frac{\rho-1}{1+\rho} DG_{pq} - 2\pi I_{pq} \\ G_{pc} & -G_{pe} & -2G_{pq} & DG_{pq} + 2\pi \frac{1-\rho}{1+\rho} I_{pq} \end{bmatrix} \begin{bmatrix} \frac{\partial \phi_1}{\partial n_1}(b) \\ \frac{\partial \phi_1}{\partial n_2}(d) \\ \frac{\partial \phi_2}{\partial n_2}(p) \\ (\phi_1 + \phi_2)(p) \end{bmatrix} = \begin{bmatrix} 2\pi I_{bc} + DG_{bc} & 0 & -G_{bq} & \frac{-1}{2(1+\rho)} DG_{bq} \\ 0 & 2\pi I_{de} + DG_{de} & G_{dq} & \frac{-1}{2(1+\rho)} DG_{dq} \\ DG_{pc} & DG_{pe} & 0 & \frac{-1}{1+\rho} DG_{pq} \\ DG_{pc} & -DG_{pe} & -2G_{pq} & 2\pi \frac{1}{1+\rho} I_{pq} \end{bmatrix} \begin{bmatrix} \phi_1(b) \\ \phi_2(d) \\ F(p) \end{bmatrix} \quad (18)$$

where  $G$  is used to indicate the discretised Green's function and  $DG$  the discretised normal derivative of the Green's function. The block matrix structure is used to emphasise the

bubble/bubble, bubble/interface and interface/interface contributions to the overall result with reference to the notation introduced in Figure 1(b). The RHS of equation (18) is known at any time step and the resultant set of equations can be inverted to determine the normal velocities  $\frac{\partial \phi_1(b)}{\partial n}$ ,  $\frac{\partial \phi_2(d)}{\partial n}$ ,  $\frac{\partial \phi_2(p)}{\partial n}$  and the sum  $(\phi_1 + \phi_2)(p)$  and hence to determine the velocity along all interfaces. Thus we can update the surface locations and potentials at each timestep.

#### 4. VALIDATION

The interaction between single/multiple bubbles and a density interface can be examined by time-stepping equations (14-17) with the interfacial velocities determined by inverting equation (19) and using splining techniques to calculate tangential velocities. The current numerical implementation has been validated by comparison with the case of  $\rho=1$  with  $\sigma_I$  (i.e. the case of a Rayleigh-Plesset bubble in an infinite ambient liquid) and with previous experimental results for the interaction of a bubble with a free surface (i.e. the case of  $\rho=0$ ) and a rigid boundary (i.e. the case of  $\rho=\infty$ ) and for the case of a water-white spirit interface with  $\rho=0.76$ . Full validation details are available in the thesis by Curtiss [20].

Consider figure 2, with  $\rho=1$  in the absence of surface tension with the bubble initially at a standoff of  $h=1$  away from the interface. In this case the bubble should depend indentially to a bubble in an infinite fluid. The numerical results from the boundary integral simulation are in exact agreement with the corresponding solution to the Rayleigh-Plesset equation. This test case was helpful in determining the appropriate truncation length for the infinite density interface.

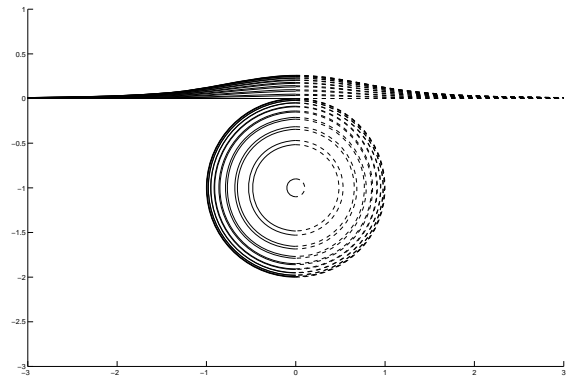


**Figure 2. Comparison between the boundary integral method (left) and the solution to the Rayleigh-Plesset equation (right) for  $\rho=1$  and  $\varepsilon=1$ .**

In the limit of  $\rho=0$  we recover a bubble collapsing near a free surface. Comparison is made with the frequently cited experiments of Gibson and Blake [5] in figure 3 for a bubble initiated at the close standoff of  $h=0.56$ . In this case there is a

s lender free surface jet which is travelling upwards and a thin downward bubble jet which pierces the lower surface of the bubble leading to the formation of a toroidal bubble. The simulation continues well into the toroidal phase beyond the final experimental frame. It is known that the features of the free surface jetting and the bubble jetting are strongly dependent on the standoff distance  $h$ . We have further validated our numerical model with the numerical results presented by Wang et al. [13] and Pearson [14].

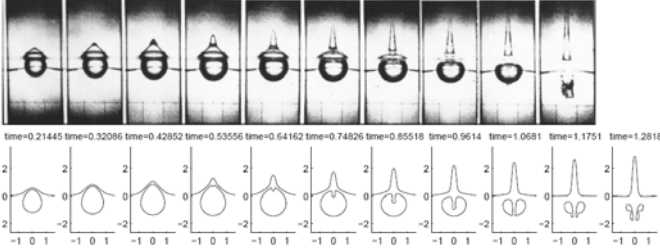


**Figure 3. Comparison between an experiment by Gibson and Blake [8] of the behaviour of a bubble near a free surface with  $h=0.56$  and the corresponding numerical results**

Arguably the best validation of the numerical implementation is with reference to the experiments. The numerical method has also been validated against the experimental results of Brujan et al. [4] for a bubble with  $h = 1.1$  near to a rigid boundary. The limit  $\rho \rightarrow \infty$  corresponds to a rigid boundary and we implement this numerically by setting  $\rho = 100$ . We can also use the method of images by placing equal strength bubbles on opposite sides of an interface with  $\rho = 1$ . Both comparisons are made in figure 4 and it is clear that the numerical method is accurately modeling the bubble dynamics. Observe that in this case the bubble jet is directed

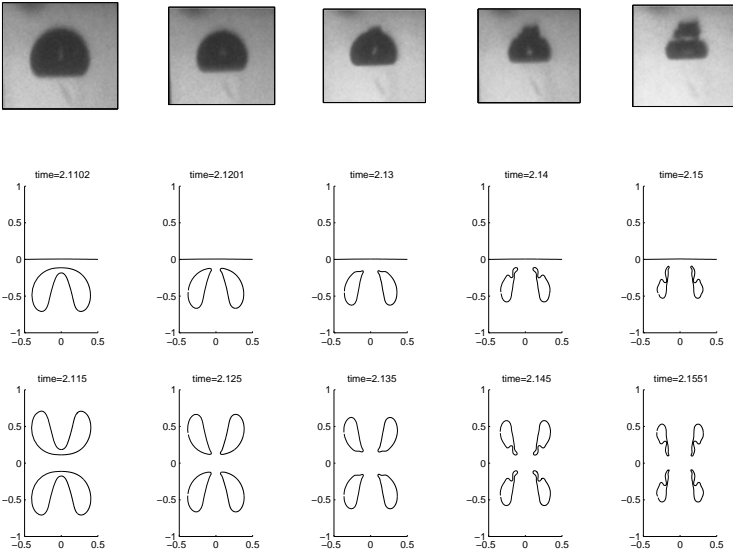


**Figure 4. Comparison between the experimental results of Brujan et al. [4] for  $h=1.1$  for a bubble near a rigid boundary: experimental results (top), numerical results with  $\rho=100$  (middle), numerical results with  $\rho=1$  (bottom).**

$\rho=100$  (middle), numerical results with image system (bottom).

Arguably the best validation of the numerical implementation is with reference to the experiments of Chahine and Bovis [2] who considered the interaction of bubble with a water/white spirit interface with a non-trivial value of  $\rho=0.76$  as seen in figure 5. In this case a spark-generated centimetre-sized bubble is formed in the water layer. Figure 5 compares two of these experiments with the current boundary integral simulations acting under gravity with a buoyancy parameter of  $\delta=0.0147$ . With the shallow standoff of  $h=0.87$ , the simulation is halted after one oscillation as a non-axial jet impact occurs. In the deeper standoff case of  $h=2.2$ , a buoyancy driven jet forms, leading to an axial jet impact and is hence simulated further using the toroidal bubble model. In both cases excellent agreement is seen between the experiment and the simulation.

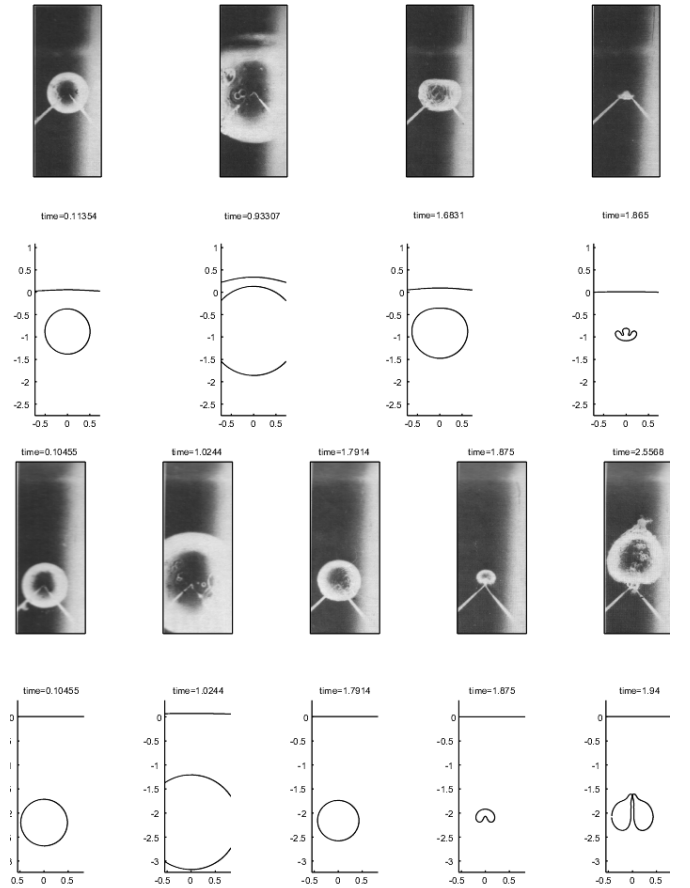


**Figure 5. Comparison between the experimental of Chahine and Bovis [2] for a bubble near a water/white spirit interface and the numerical results:  $h = 0.87$  (top) and  $h = 2.2$  (bottom).**

## 5. RESULTS

The numerical model above has been used to examine the interaction of a bubble (or bubbles) with a density interface. The

direct output from equations (12) is the time-evolution of all of the free surface shapes. In addition, information concerning the pressure field and the velocity field in fluids 1 and 2 can be obtained using equations (4), and (17) as detailed by Curtiss [20].

Blake [21] describes how the Kelvin Impulse can be used to predict the displacement of a bubble in close proximity to a boundary. The results show that bubbles should be attracted to a solid boundary and repelled by a free surface. At some intermediate density ratio it would seem logical that the bubble would neither be attracted nor repelled by the boundary. Figure 6 plots the location of the bubble centroid for a range of density ratios and standoff distances. Results in the left hand figure are presented for  $\rho = 0.2, 0.4, 0.6, 0.8$  and results in the right hand figure are presented for  $\rho = 1.2, 1.6, 2, 3, 5$ . In all cases the strength parameter is  $\varepsilon = 100$  and gravity and surface tension are ignored. The graphs are orientated so that the denser fluid is always at the base and hence the interface is above the bubble for  $\rho < 1$  and below for  $\rho > 1$ . Observe that at the later collapse stages of the simulations when the bubble jetting occurs, typically leading to the formation of a toroidal bubble, the centroid migration is indeed in accordance with the Kelvin Impulse predications. Observe that the centroid migration is reduced as the standoff is increased and as the density ratio approaches 1.

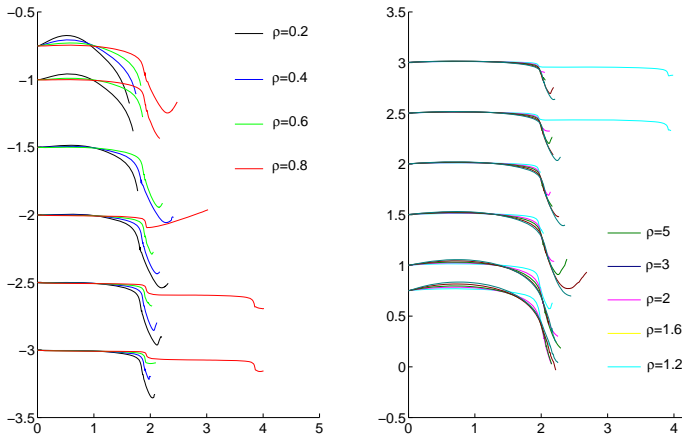
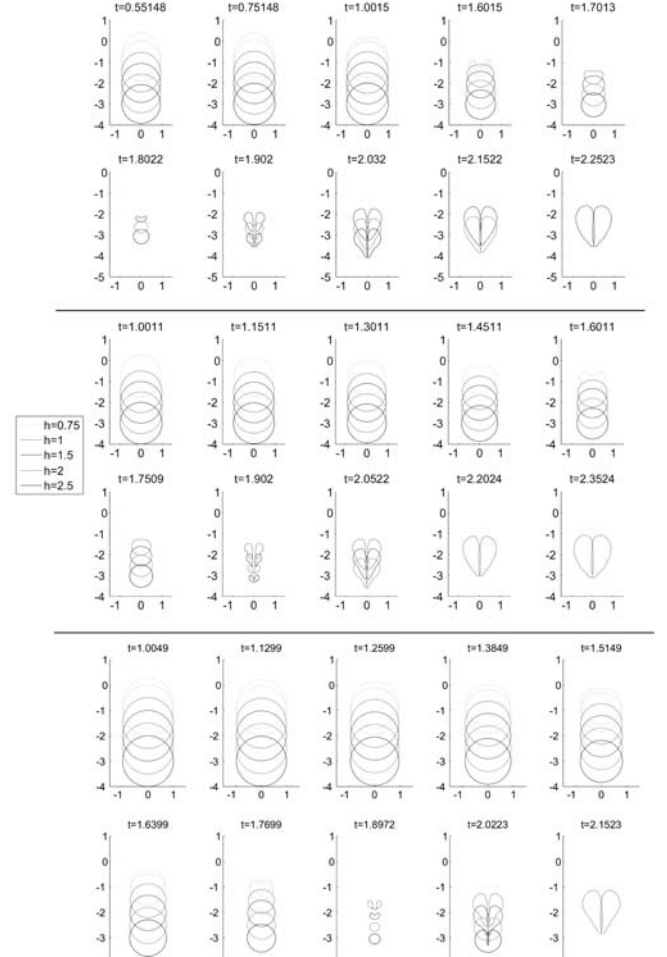


**Figure 6. The location of the bubble centroid as a function of time as the standoff distance and density ratio are varied.**

The displacement of the bubble centroid is primarily affected by the non-spherical jetting phenomena. This is apparent in all simulations, evidenced by the sudden alteration to the centroid location during the collapse phase of the bubble. The effect the density ratio has on the time to jetting may also be readily observed by this behaviour, with simulations with density ratios closest to unity displaying a prolonged existence before this onset. During the toroidal phase in several simulations, there is a late change in the direction of the movement of the bubble centroid. This is due to the rear of the bubble expanding more spherically than the front, as the front is dragged into an elongated shape by the threading jet as is clearly demonstrated in figures 7 and 8. These show the bubble shapes

at various time intervals for  $\rho = 0.2, 0.4, 0.6$  and  $\rho = 1.6, 2, 5$  respectively.

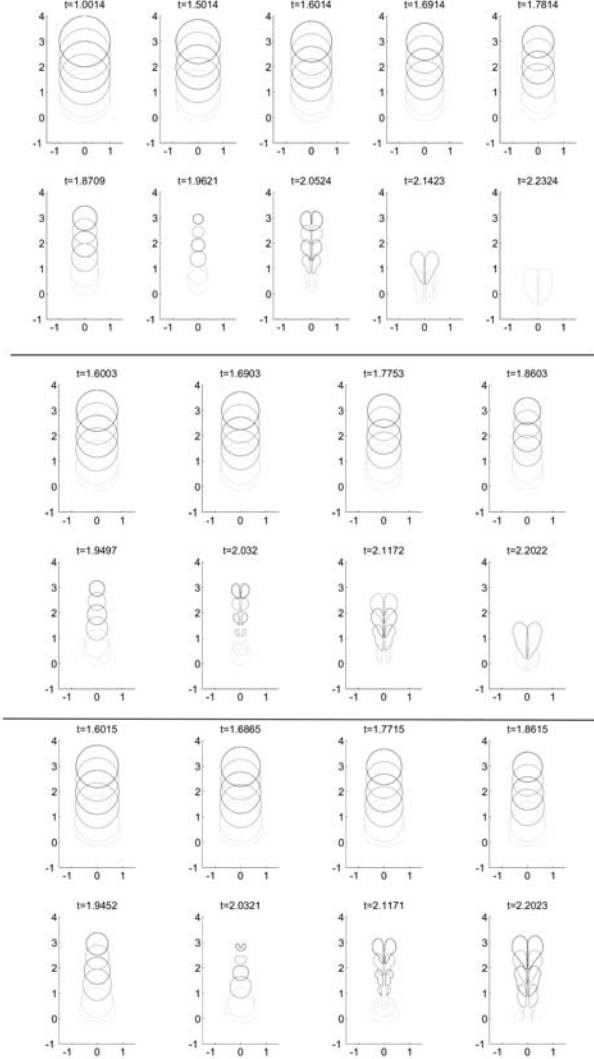
It is of particular interest to observe the difference in toroidal behaviour displayed as the standoff distance and density varies. For example, the bubble toroid with  $\rho = 2, h = 3$  forms a more slender snout than at shallower standoff distances. This is repeated for  $\rho = 0.4$ , yet for  $\rho = 0.6$  the bubble jet failed to impact on the opposing wall in the standoff case  $h = 3$ .



**Figure 7. Bubble shapes for  $\rho = 0.2$  (top),  $\rho = 0.4$  (middle) and  $\rho = 0.6$  (bottom) .**

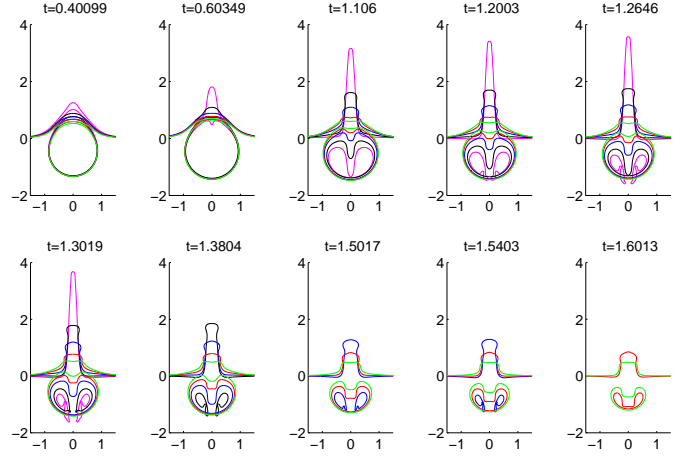
In the simulations contained in figure 8, one observes more variation in both the singly and doubly connected phases. Unlike the simulations in figure 7, the bubbles with  $\rho = 1.6, 2, 5$ , at standoff distances below 1.5, migrate sufficiently far to become entrained into the interface. Such entrainment results in the flattening of the lower side of the bubble, and a subsequent delay in the time to jet formation. This flattening increases with  $\rho$  as anticipated by the known behaviour near a rigid wall. Such behaviour then impacts on the toroidal phases, with bubbles at greater standoff distances developing a slender protrusion at the fore, whilst at lower standoff distances the development of the frontal lobe is inhibited, and a disturbance is

seen to propagate about the bubble toward the rear. mentioned the attraction toward the interface is significant accelerated during the jetting phase, as may be seen in figure. Indeed the translation in the centroids in the shallower stanc cases end below the initial location of the two fluid interface.



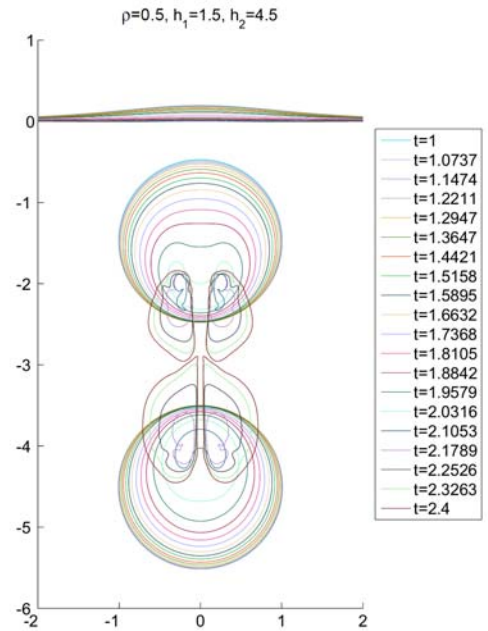
**Figure 8. Bubble shapes for  $\rho = 1.6$  (top),  $\rho = 2$  (middle) and  $\rho = 5$  (bottom).**

Figure 9 shows the evolution of the density interface and bubble shape for the case of one bubble with a standoff distance of  $h = 0.5$  for  $\rho = 0, 0.1, 0.2, 0.3$  and  $0.4$ . The case of  $\rho = 0$  corresponds to the interaction of a bubble with a free surface where an intense upwards jet is formed on the density interface with a corresponding counter-jet on the bubble surface. As the density ratio increases away from the free surface case, the intensity of the free surface jet and the counter-jet decreases. The bubbles become toroidal when the counter-jet pierces the lower face of the bubble. The simulations proceed into the toroidal regime until they become numerically unstable. While it is not shown here, simulations for  $\rho > 1$  approach the known limit for the interaction of a bubble with a rigid boundary in the limit as  $\rho \rightarrow \infty$ .



**Figure 9. The evolution of the bubble and fluid-fluid interface for  $\rho = 0$  (magenta),  $0.1$  (black),  $0.2$  (blue),  $0.3$  (red) and  $0.4$  (green).**

The numerical model that we have constructed can have any number of bubbles on either side of the interface. Figure 10 follows the evolution of two bubbles on the same side of a density interface with  $\rho = 0.5$  where the bubbles initially have standoff distances of  $1.5$  and  $4.5$  respectively. Each bubble has the same strength parameter  $\varepsilon = 100$  so that initially the bubbles expand spherically to their maximum radius and then they collapse. As they collapse the bubbles strongly interact with each other. While the density interface remains predominantly horizontal throughout jetting occurs in both bubbles during the collapse and then re-expansion phase and ultimately both bubbles become toroidal. The relative strength of the bubble-bubble interaction and the bubble-interface interactions depends on the standoff distances and the density ratio.



**Figure 10. Shape contours for two bubbles in lower layer.**

An interesting interaction with one bubble on each side of the density interface is shown for  $\rho = 1.3$  in figure 11 when standoff distance of the bubble in the lower layer is 0.75 and standoff distance of the bubble in the upper layer is 1.5. deformation of both the upper and lower bubble is significant at this value of  $\rho$  than would be the case if either the bubbles was absent. The bubble-bubble interaction and bubble-interface interaction depends on the value of  $\rho$  increases as the standoff distances decrease. For the considered the bubble in the upper layer is strongly deformed the interaction. The upper bubble rapidly becomes toroidal the bubble jet impacting upon the density interface deforming the lower bubble. This suggests a possible mechanism for the enhancement of mixing across a density interface.

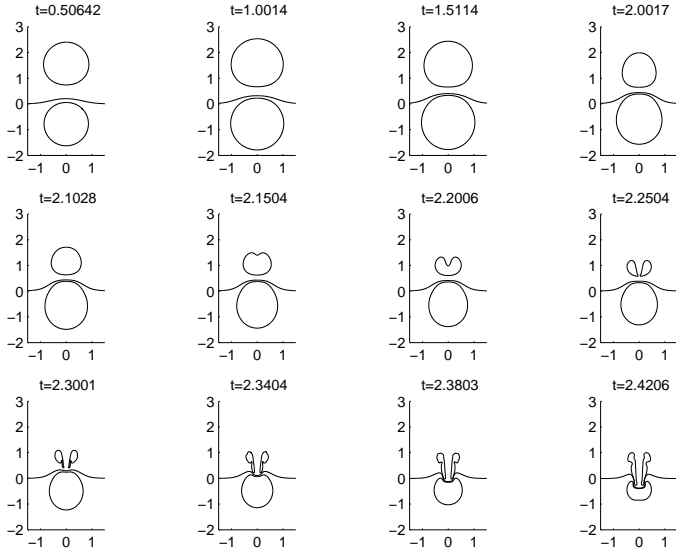


**Figure 11. Two bubble interaction about a density interface with  $\rho = 1.3$ , with bubbles in the opposite side of the interface.**

The case of  $\rho = 1.3$  with one bubble above (with standoff distance 1.5) and two bubbles below the density interface with standoff distances of 1.5 and 4.5 respectively is shown in Figure 12. As expected for this value of  $\rho$  it is the bubble in the upper layer which is most strongly deformed. The downward liquid jet in the upper bubble deflects the density interface downward and deforms the middle bubble. The lower bubble in the dense layer interacts with the bubble above it to form a strong upward axial jet ultimately becoming toroidal.

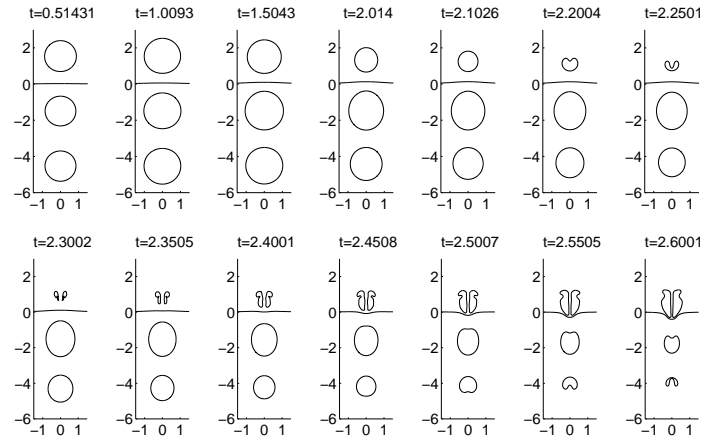


**Figure 12. Three bubble interaction with a density interface.**

## 6. CONCLUSIONS

We have implemented an axisymmetric multi-bubble numerical model to examine the interaction of bubbles with a density interface. The model is based on the boundary integral method and it has been validated against previous experimental results. A range of interesting physical phenomena have been identified in figures 3 to 1 with further results detailed in the thesis by Curtiss [20]. The model is able to examine bubbles well into the toroidal regime and across the complete range of interfacial density ratios.

## ACKNOWLEDGMENTS

Geoffrey Curtiss kindly acknowledges the financial support of EPSRC, The Numerical Algorithms Group and the Smith Institute throughout his PhD Studies.

## REFERENCES

- 1 Lundren, T.S. & Mansour, N.N. (1979), 'Vortex ring bubbles', *J. Fluid Mech.*, **224**, 177-195.
- 2 Chahine, G.L. & Bovis, A. (1980), 'Oscillation and collapse of a cavitation bubble in the vicinity of a two-liquid interface', Springer series in electrophysics 4 - cavitation and inhomogeneities in underwater acoustics, 23-29.
- 3 Benjamin, T.B., & Ellis, A.T. (1966) 'The collapse of cavitation bubbles and the pressures thereby produced against solid boundaries', *Phil. Trans. R. Soc. Lond. A*, **260**, 221-240.
- 4 Brujan, E. A., Keen, G.S., Vogel, A. & Blake, J.R. (2002), 'The final stages of collapse of a cavitation bubble close to a rigid boundary', *Phys. Fluids*, **14**, 85-92.
- 5 Philip, A. & Lauterborn, W. (1998) 'Cavitation erosion by single laser-produced bubbles', *J. Fluid Mech.*, **361**, 75-116.
- 6 Tomita, Y. & Shima, A. (1986) 'Mechanisms of impulsive pressure generation and damage pit formation by bubble collapse', *J. Fluid Mech.*, **169**, 535-564.

- 7 Lauterborn, W. & Bolle, H. (1975), 'Experimental investigations of cavitation-bubble collapse in the neighbourhood of a solid boundary', *J. Fluid Mech.*, **72**, 391-399.
- 8 Gibson, D.C. & Blake, J.R., 'Growth and collapse of a vapour cavity near a free surface', *J. Fluid Mech.*, **111**, 123-140.
- 9 Lenoir, M. (1976), 'Calcul numerique de l'implosion d'une bulle de cavitation au voisinage d'une paroi ou d'une surface libre', *J. Mechanique*, **15**, 725-751.
- 10 Taib, B. B. (1985) Boundary integral method applied to cavitation bubble dynamics', PhD Thesis, University of Wollongong.
- 11 Blake, J. R., Taib, B.B., & Doherty, G. (1986), 'Transient cavities near boundaries. Part 1. Rigid Boundary', *J.Fluid Mech.*, **170**, 479-497.
- 12 Blake, J. R., Taib, B.B., & Doherty, G. (1986), 'Transient cavities near boundaries. Part 2. Free Surface', *J.Fluid Mech.*, **181**, 197-212.
- 13 Wang, Q. X., Yeo, K. S., Khoo, B.C., & Lam, K.Y. (2005), 'Vortex ring modeling of toroidal bubbles', *Theor & Comp. Fluid Dyn*, **19**, 1-15.
- 14 Pearson, A. (2003) Hydrodynamics of jet impact in a collapsing bubble. PhD Thesis, The University of Birmingham.
- 15 Robinson, P.B., Blake, J.R., Kodama, T., Shima, A. & Tomita, Y. (2001) 'Interaction of cavitation bubbles with a free surface', *J. Appl. Phys.*, **89**, 8225-8237.
- 16 Klaseboer, E. & Khoo, B. C. (2004). 'Boundary integral equations as applied to an oscillating bubble near a fluid-fluid interface', *Comp. Mech.*, **33**, 129-138.
- 17 Klaseboer, E. & Khoo, B. C. (2004). 'An oscillating bubble near an elastic material', *J. Appl. Phys.*, *Comp. Mech.*, **96**, 5808-5818.
- 18 Brujan, E. A., Nahen, K.P. & Vogel, A. (2001) 'Dynamics of laser-induced caviation bubbles near an elastic boundary', *J. Fluid Mech.*, **433**, 251-281.
- 19 Brujan, E. A., Nahen, K.P. & Vogel, A. (2001) 'Dynamics of laser-induced caviation bubbles near elastic boundaries: Influence of the elastic modulus', *J. Fluid Mech.*, **433**, 283-314.
- 20 Curtiss, G. A. (2009) Non-linear, , non-spherical bubble dynamics near a two fluid interface. PhD Thesis, University of Birmingham.
- 21 Blake, J.R. (1988) 'The Kelvin impulse: Application to cavitation bubble dynamics', *J. Austral. Math. Soc.*, **30**, 127-146.



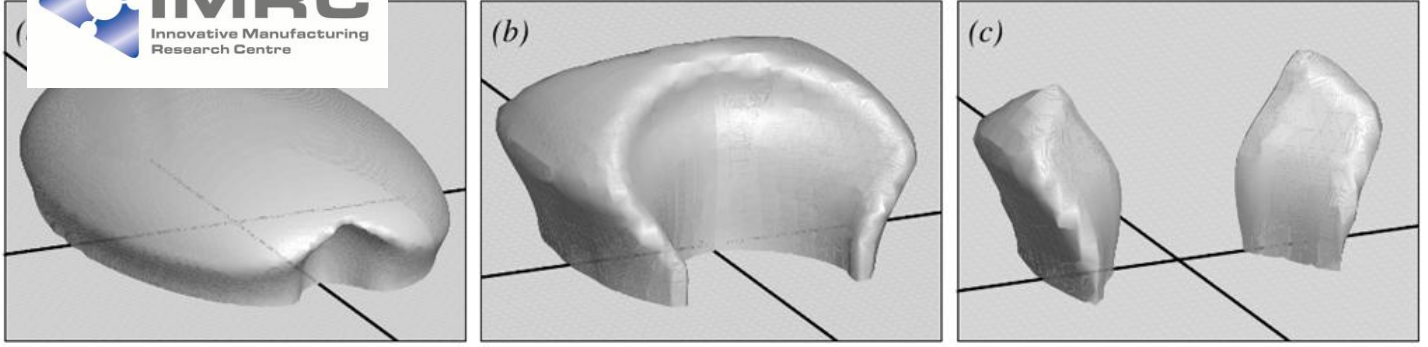


Figure 8: Ellipsoidal vapor-bubble collapse: bubble shape during near-wall ellipsoidal vapor-bubble collapse

Figure 5: Spherical vapor-bubble collapse: initial situation and bubble shape after cavity development for configuration A, B and C. Figure 3: Evolution of the normalized bubble radius  $R^* = R_i / D$  with respect to normalized time  $t^* = t / D$

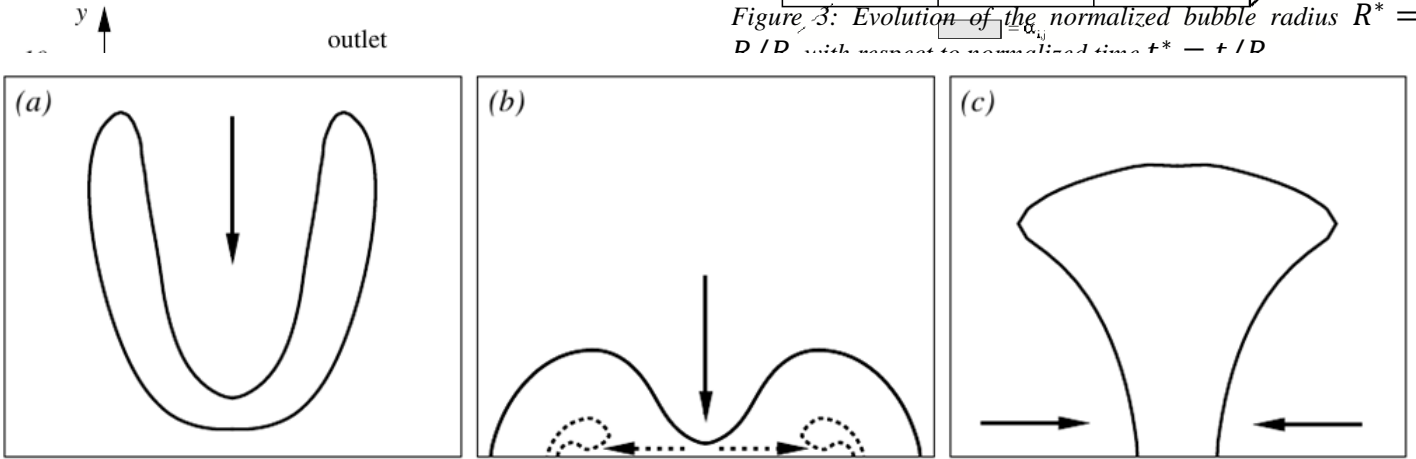


Figure 6: Spherical vapor-bubble collapse: liquid jets during near-wall vapor-bubble collapse (frame size in  $\mu\text{m}$ ): (a) Wall-normal re-entrant jet for configuration A (296x244), (b) primary wall-normal re-entrant jet (solid line) and secondary wall-parallel outward-pointing jet (dashed line) for configuration B (352x292), and (c) wall-parallel inward-pointing jet for configuration C (128x104). Arrows indicate the jet orientation.

Figure 4: Sketch of the problem. Three configurations with

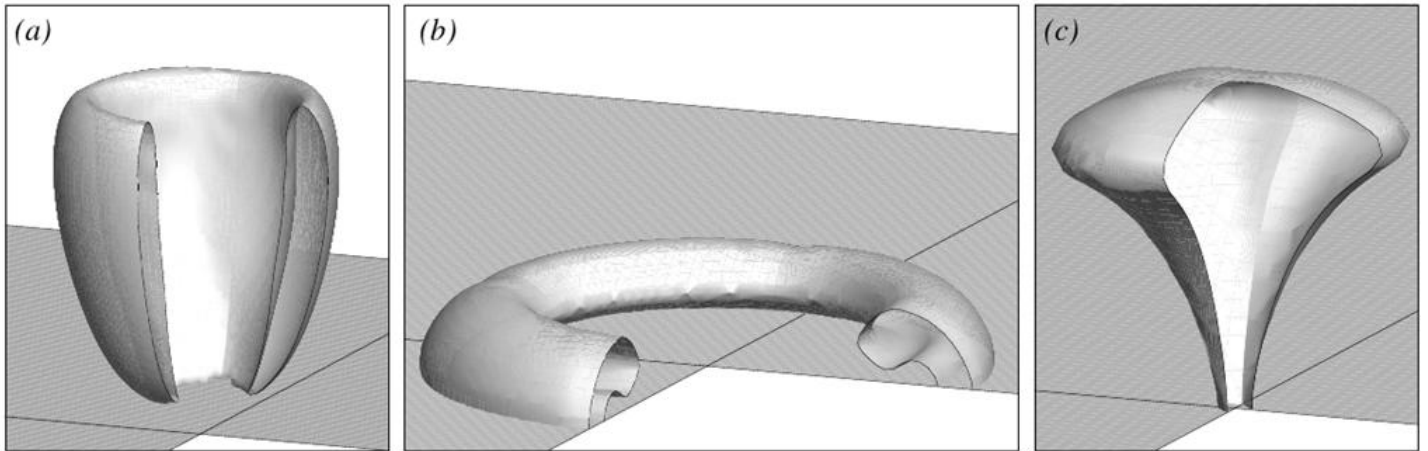


Figure 7: Spherical vapor-bubble collapse: cuts through an iso-surface of zero level-set (interface) showing the shape of the bubble during the stage of liquid jets.

## Numerical investigation of cavitation bubble dynamics near walls

Eric Lauer\*

Xiangyu Hu

Stefan Hickel

Nikolaus A. Adams

Technische Universität München, Munich, Germany

\* Eric.Lauer@aer.mw.tum.de

### ABSTRACT

We present a sharp-interface multi-fluid flow approach including an efficient evaporation/condensation model. The model assumes that phase change is in thermal non-equilibrium, and is much slower than the hydrodynamic interaction described by the interfacial Riemann problem. This extension gives us the opportunity to look at a wide range of problems with phase-change, including cavitating flows. Of high practical interest is the collapse of cavitation bubbles near walls. We investigate the differences in collapse evolution for detached and attached bubbles. It is shown that the maximum wall pressure strongly depends on the symmetry of the collapse mechanisms. Asymmetric attached bubbles lead to significantly different topology changes during collapse than symmetric bubbles but exhibit roughly the same range of maximum pressures.

### 1. INTRODUCTION

Cavitation is known as one of the major reasons for damages in hydraulic applications. The collapse of cavitation bubbles is the main cause of erosion on marine propellers or on blades in turbo-machinery. On the other hand, the destructive effects of cavitation can be exploited in medical application such as the shock wave lithotripsy.

Two fundamental mechanism are observed in the cavitation bubble collapse process. First Rayleigh [1] described the release of shock waves upon bubble collapse, second Kornfeld & Suvorov [2] observed the development of a re-entrant jet in non-spherical bubble collapse like it occurs close to solid walls. Both, the impact of shock waves and of the re-entrant jet on a surface might lead to erosion.

Progress in high-speed photography allowed more detailed experimental investigations. Lindau & Lauterborn [3] visualized the propagation of shocks and the generation of the re-entrant jet for the bubble collapse close to a solid wall. Furthermore they show the formation of a counter jet during the rebound, indicating that there is still a lack in understanding of the mechanisms in cavitation-bubble collapse. However, more detailed experimental measurements are difficult due to small spatial and temporal scales. Thus numerical simulation might help to get a better understanding, but cavitating flow is still a challenging problem for modern computational fluid dynamics.

In this paper we present a sharp-interface method, which is based on an earlier approach of Hu et al. [4]. The material interface is accurately resolved on arbitrary Cartesian grids and

therefore a good insight into interface movement and deformation is provided.

We suppose that compressible effects such as shock wave propagation are important in vapor and water at least at the final stages of a bubble collapse. Viscosity and surface tension are neglected in this paper, since Johnsen & Colonius [5] show that their influence on the relevant stages of a vapor bubble collapse is small. Due to very small time scales, heat diffusion is also of no importance [6].

We apply the Euler equation for both fluids separately using a standard finite-volume scheme, which is modified by considering computational cells being cut by the interface. The discretized governing equations are updated conservatively. The method solves the difficulty of conservation for front-tracking methods and treats topological changes naturally by combining the interface description and geometric operations with a level-set technique.

Interactions between both fluids at the interface are taken into account by solving the Riemann problem at the interface and introducing a conservative exchange term. While the original model deals only with momentum and energy exchange over the interface, the new approach includes the effect of phase-change phenomena such as evaporation and condensation.

After first results obtained on one-dimensional equidistant Cartesian grids [7], we now present the three-dimensional version of our method working on arbitrary Cartesian grids.

The objective of this work is to contribute to the clarification of wall-attached cavitation-bubble collapse. Three different configurations of spherical cavitation bubbles are investigated. Depending on the initial wall position, we find a different collapse behavior. We observe wall-normal, as well as wall-parallel jets. The main focus is on the effect of initial bubble shape on extreme events (maximum wall pressure, regions with high potential of bubble rebound).

In a last step, we focus on the significance of initial bubble asymmetries on the collapse dynamics by considering an initially ellipsoidal vapor bubble attached to a wall. This scenario leads to significantly different topology changes during collapse, but maximum wall pressures are roughly in the same range as for spherical bubbles.

### 2. GOVERNING EQUATIONS

We consider the three-dimensional Euler equations in conservative form

$$\frac{\partial \mathbf{U}}{\partial t} + \nabla \cdot \mathbf{F}(\mathbf{U}) = 0, \quad (1)$$

with the solution vector  $\mathbf{U} = [\rho, \rho u_1, \rho u_2, \rho u_3, E]$ . Density  $\rho$ , momentum  $\rho \mathbf{u}$  and energy  $E$  are the conserved variables. The flux vector is given as

$$\mathbf{F}_i(\mathbf{U}) = \begin{pmatrix} \rho u_i \\ \rho u_i u_1 + \delta_{i1} p \\ \rho u_i u_2 + \delta_{i2} p \\ \rho u_i u_3 + \delta_{i3} p \\ u_i (E + p) \end{pmatrix}, \quad (2)$$

where  $\mathbf{u}$  is the velocity vector.

## 2.1 Ideal gas

For an ideal gas, the pressure is determined from

$$E = \frac{1}{\gamma - 1} p + \frac{1}{2} \rho \mathbf{u}^2. \quad (3)$$

The ideal gas equation of state is

$$T = \frac{p}{R\rho}, \quad (4)$$

with the specific gas constant  $R$ . We model vapor as an ideal gas and we assume  $\gamma = 1.335$  and  $R = 461.5 \text{ J kg}^{-1} \text{ K}^{-1}$ .

## 2.2 Water-like fluids

For water-like fluids we apply Tait's equation of state. The temperature  $T$  is assumed to be constant, and pressure  $p$  and total energy  $E$  are functions of density only

$$p = B \left( \frac{\rho}{\rho_0} \right)^\gamma - B + A, \quad (5)$$

$$E = \frac{1}{\gamma - 1} (p + B - A) + B - A + \frac{1}{2} \rho \mathbf{u}^2.$$

The additional coefficients  $B$ ,  $A$  and  $\rho_0$  are taken as constants. For water we set  $B = 3310 \text{ bar}$ ,  $A = 1 \text{ bar}$ ,  $\rho_0 = 1 \text{ bar m}^{-3}$  and  $\gamma = 7.15$ . Since the total energy is only a function of density and velocity, energy evolution is omitted from Eq.(1) and (2).

## 3. OVERVIEW OF THE METHOD

### 3.1 Mathematical basics

The computation domain  $\Omega$  is divided by the interface  $\Gamma(t)$  into two different subdomains  $\Omega_1(t)$  and  $\Omega_2(t)$ . The volume

$\Omega_1(t)$  accounts for the region occupied by a first fluid and  $\Omega_2(t)$  refers to the region occupied by a second fluid. We solve Eq. (1) for the fluid occupying the sub-domain  $\Omega_m(t)$  ( $m = 1, 2$ ) on a three-dimensional grid with spacings  $\Delta x(i), \Delta y(j), \Delta z(k)$ . Integrating Eq. (1) over the space-time volume  $V \cap \Omega_m(t)$  of a computational cell  $(i, j, k)$  we obtain the following finite volume discretization

$$\int_n^{n+1} dt \int_{V \cap \Omega_m(t)} dxdydz \left( \frac{\partial \mathbf{U}_m}{\partial t} + \nabla \cdot \mathbf{F}(\mathbf{U}_m) \right) = 0, \quad (6)$$

where  $\mathbf{U}_m$  is the the solution vector of the considered fluid. The fluid volume  $V \cap \Omega_m(t)$  can be expressed through  $\alpha_m(t) \Delta x \Delta y \Delta z$  where  $\alpha_m(t)$  is the time dependent fluid volume fraction of the considered cell and fluid  $m$  with  $\alpha_1(t) + \alpha_2(t) = 1$ . Applying Gauss theorem we obtain

$$\int_n^{n+1} dt \int_{V \cap \Omega_m(t)} dxdydz \frac{\partial \mathbf{U}_m}{\partial t} + \int_n^{n+1} dt \int_{\partial(V \cap \Omega_m(t))} dxdydz \mathbf{F}(\mathbf{U}_m) \cdot \mathbf{n} = 0 \quad (7)$$

where  $\partial(V \cap \Omega_m(t))$  are the cell faces. Defining the interface through  $\Gamma(t) = V \cap \partial \Omega_m(t)$ , the term  $\partial(V \cap \Omega_m(t))$  can be expressed as the combination of two elements.

The first element is the sum of the surfaces obtained by intersecting the interface with the cell faces, which can be expressed in the following form  $A_m^{11} \Delta y \Delta z$ ,  $A_m^{12} \Delta y \Delta z$ ,  $A_m^{21} \Delta x \Delta z$ ,  $A_m^{22} \Delta x \Delta z$ ,  $A_m^{31} \Delta x \Delta y$ ,  $A_m^{32} \Delta x \Delta y$  where  $A_m^{pq}$  represents the so called cell face aperture described in Fig. 1 and with  $A_1^{pq} + A_2^{pq} = 1$ . The second element represents the portion of the interface  $\Delta \Gamma(t)$  within the cell  $(i, j, k)$ . After introducing the volume averaged solution

$$\bar{\mathbf{U}} = \frac{1}{\alpha_m(t)V} \int_{\alpha_m(t)V} \mathbf{U} dxdydz, \quad (8)$$

Eq. (7) can be rewritten

$$\begin{aligned}
& V(\alpha_m^{n+1} \bar{U}m_{n+1} - \alpha_m^n \bar{U}m_n) \\
& = \int_n^{n+1} dt \Delta y \Delta z [A_m^{12}(t) Fm_{12} - A_m^{11}(t) Fm_{11}] \\
& + \int_n^{n+1} dt \Delta x \Delta z [A_m^{22}(t) Fm_{22} - A_m^{21}(t) Fm_{21}] \\
& + \int_n^{n+1} dt \Delta x \Delta y [A_m^{32}(t) Fm_{32} - A_m^{31}(t) Fm_{31}] \\
& + \int_n^{n+1} dt X_m(\Delta \Gamma(t)),
\end{aligned} \tag{9}$$

where  $\alpha_m \bar{U}m$  and  $\bar{U}m$  are the vector of the conserved quantities in the cut cell and the vector of volume averaged conservative variables respectively.  $F_m^{pq}$  is the average flux across a cell face and  $X_m$  is the average mass, momentum and energy exchange across the interface. For full cells, which are not cut by the interface, volume fractions and cell face apertures become unity, the corresponding interface surface fraction vanishes and Eq.(9) simplifies to

$$\begin{aligned}
V(\bar{U}m_{n+1} - \bar{U}m_n) & = \int_n^{n+1} dt \Delta y \Delta z [Fm_{12} - 1 \\
& + \int_n^{n+1} dt \Delta x \Delta z [Fm_{22} - Fm_{21}] \\
& + \int_n^{n+1} dt \Delta x \Delta y [Fm_{32} - Fm_{31}]
\end{aligned} \tag{10}$$

recovering a standard finite volume scheme on a three-dimensional Cartesian grid. Being effective only in the cells that are cut by the interface, this immersed interface method can be seen as a local modification of the standard finite volume scheme close to the interface.

## 3.2 Geometry of the interface

Cell face apertures  $A_m^{pq}(t)$ , volume fractions  $\alpha_m(t)$  and interface area  $\Delta \Gamma(t)$  are determined from a levelset field  $\Phi$ , i.e., a signed distance function from a local point of the domain to the immersed interface. The zero-levelset contour ( $\Phi = 0$ ) describes the interface between the two fluids. Cells that are completely inside the other fluid are blocked through a zero value for the cell face apertures and consequently they will not have any contributions during the computation. The levelset field allows for the treatment of arbitrary geometries and can deal with

moving and strongly deforming interfaces, where the levelset field is updated following Fedkiw et al. [8] and the volume fractions and face apertures are reconstructed at each time step.

## 3.3 Interface interaction

The interface interaction term  $X_m(\Delta \Gamma)$  contains two elements accounting for the contributions of pressure and mass transfer across the interface

$$X_m(\Delta \Gamma) = X_m^p + X_m^t. \tag{11}$$

In the presence of viscosity, interface friction can be taken into account by introducing a no-slip correction on the interface. In case of high temperature differences between both fluids or large time scales, an additional heat transfer term would be needed as well, but both terms are neglected in this paper.

### 3.3.1 Pressure term $X_m^p$

Following an approach proposed by Hu et al.[4], the evolution of the interface is determined by the interface condition given by a two-material Riemann problem

$$\Re(U_1, U_2) = 0 \text{ on } \Gamma. \tag{12}$$

To obtain the momentum and energy exchanges across the interface, the Riemann problem is solved in every cut cell in interface normal direction. For problems with only weak or moderate shocks and expansion waves, simple non-iterative approximate Riemann solvers such as those of Toro [9] are sufficient for reasonable results, otherwise more accurate iterative solvers are needed. In this paper, the interface condition is obtained by the interface interaction method of Hu & Khoo [10].

After solving the Riemann problem for the interface pressure  $p_i$  and the interface normal velocity  $u_i$ , we obtain the contributions of the term  $X_m^p$  to momentum and energy equation

$$X_m^p = \begin{pmatrix} 0 \\ p_i \Delta \Gamma (n_m \cdot \hat{i}) \\ p_i \Delta \Gamma (n_m \cdot \hat{j}) \\ p_i \Delta \Gamma (n_m \cdot \hat{k}) \\ p_i \Delta \Gamma (n_m \cdot u_i) \end{pmatrix}. \tag{13}$$

The overall conservation property is accurately satisfied since  $n_1 = -n_2$ , i.e., the transfer quantities for the two fluids have the same magnitude but opposite sign.

### 3.3.2 Mass transfer term $X_m^t$

In case of vapor-liquid interactions with phase change, we apply a mass transfer term  $X_m^t$  at the interface. It covers not only

the mass transfer across the interface but also the momentum and energy exchange due to evaporation or condensation. The subscript for differentiating between the two different fluids at an interface  $m$ , is set to  $m = v, li$  to identify vapor and liquid respectively.

To model the phase change at the interface, we apply the thermal non-equilibrium assumption proposed by Fujikawa & Akamatsu [11]. During the phase-change process the pressure is in equilibrium at the vapor pressure and the temperature has a discontinuity at the phase interface. An expression for the rate of evaporation and condensation  $\dot{m}$  can be found in the book of Schrage [12]

$$\dot{m} = \frac{\lambda}{\sqrt{2\pi R_v}} \left( \frac{p_s(T_{li})}{\sqrt{T_{li}}} - \frac{p_v}{\sqrt{T_v}} \right). \quad (14)$$

Here,  $R_v$  is the specific gas constant in the vapor phase;  $\lambda$  is the accommodation coefficient for evaporation or condensation (assumed constant), equal to the ratio of vapor molecules sticking to the phase interface to those impinging on it;  $T_v$  and  $T_{li}$  are the temperatures of the vapor and the liquid at the phase interface, respectively;  $p_v$  is the actual vapor pressure at the interface, and  $p_s(T_{li})$  is the equilibrium (saturation) vapor pressure at temperature  $T_{li}$  and is obtained from the Clausius-Clapeyron equation

$$p_s(T_{li}) = p_0 \exp \left[ \frac{L_v}{R_v} \left( \frac{1}{T_0} - \frac{1}{T_{li}} \right) \right], \quad (15)$$

where  $L_v$  is the latent heat of vaporization, and  $p_0$  and  $T_0$  are given by a reference saturation state. With Eq.(14), the phase-change induced interface velocity is

$$\Delta q^* = \frac{\dot{m}}{\rho_{li}}, \quad (16)$$

where  $\rho_{li}$  is the density of the liquid at the interface. In cavitating flow,  $\Delta q^*$  is usually small and much smaller than the advection velocity of the interface (Brennen 1995), which suggests that the change rates of pressure and temperature caused by the latent heat are insignificant. Therefore, one can assume that the phase change is much slower than the hydrodynamic interface interaction. As heat conduction in the bulk is also neglected, one can obtain  $p_v$ ,  $\rho_{li}$ ,  $T_{li}$  and  $T_v$  from the solution of the Riemann problem Eq.(11).

The mass transfer term  $X_m^t$  follows

$$X_m^t = X_{li}^t = \begin{pmatrix} \dot{m} \Delta \Gamma \\ \dot{m} \Delta \Gamma (\mathbf{v} \cdot \hat{\mathbf{i}}) \\ \dot{m} \Delta \Gamma (\mathbf{v} \cdot \hat{\mathbf{j}}) \\ \dot{m} \Delta \Gamma (\mathbf{v} \cdot \hat{\mathbf{k}}) \\ \dot{m} \Delta \Gamma \left( e_v + \frac{1}{2} |\mathbf{v}|^2 \right) + p_l \Delta q^* \Delta \Gamma \end{pmatrix}, \quad (17)$$

where  $\mathbf{v}$  is the velocity of the liquid at the interface in case of evaporation and the velocity of the vapor in case of condensation, respectively.

Note that the energy exchange is usually of no importance for the liquid since the introduced temperature change is negligible.

### 3.4 Small-cell mixing

The intersection between the immersed interface and the Cartesian grid can give rise to small cells, for which a stable fluid state may not be reached based on the time step calculated according to the full cell size. On the other hand, accounting for the real size of these small cells while computing the time step according to the CFL condition can lead to extremely small time step sizes.

In order to ensure numerical stability without excessively decreasing the time step size, a conservative mixing procedure is introduced, where the conserved quantities of small cells are mixed with larger neighbor cells. The procedure follows the approach proposed by Hu et al. [4]. Modifications are introduced in order to account for non uniform grid spacing. The number of target cells adopted for the mixing is also increased and now includes all the possible neighbor cells available in a three dimensional field.

The mixing procedure is applied only to cut cells with a volume fraction below a certain threshold, which in our computations is set to  $\alpha_m = 0.6$ . Increasing this threshold leads to a better numerical stability but at the same time makes the method more diffusive and vice versa. Each fluid will be considered separately ( $m = 1, 2$ ).

Seven mixing target cells are determined from the local normal vector on the interface. For each mixing target cell a weight  $\beta_m$  is defined

$$\begin{aligned} \beta_m^x &= |\mathbf{n}_m \cdot \hat{\mathbf{i}}|^2 \alpha_{imix,j,k} \\ \beta_m^y &= |\mathbf{n}_m \cdot \hat{\mathbf{j}}|^2 \alpha_{i,jmix,k} \\ \beta_m^z &= |\mathbf{n}_m \cdot \hat{\mathbf{k}}|^2 \alpha_{i,j,kmix} \\ \beta_m^{xy} &= |(\mathbf{n}_m \cdot \hat{\mathbf{i}})(\mathbf{n}_m \cdot \hat{\mathbf{j}})| \alpha_{imix,jmix,k} \\ \beta_m^{xz} &= |(\mathbf{n}_m \cdot \hat{\mathbf{i}})(\mathbf{n}_m \cdot \hat{\mathbf{k}})| \alpha_{imix,j,kmix} \\ \beta_m^{yz} &= |(\mathbf{n}_m \cdot \hat{\mathbf{j}})(\mathbf{n}_m \cdot \hat{\mathbf{k}})| \alpha_{i,jmix,kmix} \\ \beta_m^{xyz} &= |(\mathbf{n}_m \cdot \hat{\mathbf{i}})(\mathbf{n}_m \cdot \hat{\mathbf{j}})(\mathbf{n}_m \cdot \hat{\mathbf{k}})|^{2/3} \alpha_{mixi,jmix,k} \end{aligned} \quad (18)$$

To avoid double mixing between two cells, the weighting factor is set to zero whenever the cell's volume fraction is larger than that of the target cell. The weights are subsequently normalized to ensure consistency

$$\sum_{trg} \beta_m^{trg} = 1, \quad (19)$$

where  $trg$  stands for  $trg = \{x, y, z, xy, \square z, yz, xyz\}$ .

The mixing flux  $M_m^{trg}$  is calculated for each mixing direction

$$M_m^{trg} = \frac{\beta_m^{trg}}{\alpha_m V \beta_m^{trg} + \alpha_m^{trg} V} \cdot [(\alpha_m^{trg} V^{trg} \bar{U}_m^{trg}) \alpha_m V - (\alpha_m V \bar{U}_m) \alpha_m^{trg} V^{trg}]. \quad (20)$$

Conservativity is maintained by a flux formulation, consistent with non-uniform Cartesian grids

$$\bar{U}_m = (\bar{U}_m)^* + \frac{M_m^{trg}}{\alpha_m V}, \quad (21)$$

$$\bar{U}_m^{trg} = (\bar{U}_m^{trg})^* + \frac{M_m^{trg}}{\alpha_m^{trg} V^{trg}}, \quad (22)$$

where  $(\bar{U}_m)^*$  and  $(\bar{U}_m^{trg})^*$  are the volume averaged conserved variables of the cut cell and of the target cell before mixing. This procedure is applied accordingly for all cut cells and mixing target cells at the end of each Runge-Kutta substep.

It is interesting to see how the present mixing procedure deals automatically with vanished and newly created empty cells. In the first case, the residual conservative quantities are all transported to the target cells, whereas for the second case the conservative quantities in a newly created small cell are derived directly from its target cells.

### 3.5 Extending procedure

In order to allow for using unmodified, central interpolation stencils in the finite volume reconstruction scheme close to the interface, for both fluids the volume averaged variables are extended to the opposite site of the interface by

$$\frac{\partial \bar{U}_m}{\partial t_f} - \mathbf{n} \cdot \bar{U}_m = 0, \quad (23)$$

where  $t_f$  is a pseudo-time.

## 4. NUMERICAL RESULTS

### 4.1 Free spherical vapor-bubble collapse

The evolution of an empty spherical bubble in an incompressible liquid, without viscous effects and surface tension, is described by a modified form of the Rayleigh-Plesset equation [13]

$$R\ddot{R} + \frac{3}{2}\dot{R}^2 = \frac{p_L - p_{li}}{\rho_{li}}, \quad (24)$$

where  $R$  is the radius of the bubble,  $\dot{R}$  is the velocity of the bubble surface,  $\ddot{R}$  its acceleration,  $\rho_{li}$  the liquid density,  $p_{li}$  the liquid pressure at infinity, and  $p_l$  is the pressure of the liquid at the bubble surface. For analysis one assumes that the pressure at the surface is constant and equal to the saturation pressure of vapor, i.e.  $p_l = p_{sat} = 2340\text{Pa}$ . Rayleigh [1] was the first to integrate this equation of motion to evaluate the bubble collapse time

$$t_{Rayleigh} \approx 0.915 R_0 \sqrt{\frac{\rho_{li}}{p_{li} - p_{sat}}}, \quad (25)$$

where  $R_0$  is the initial bubble radius.

Following Sezal [14], we compare this analytical result with a numerical simulation of a vapor bubble at saturation pressure in water. The initial bubble radius is  $R_0 = 0.4\text{mm}$ . We take advantage of the symmetry of the full bubble problem and consider only one-eighth of the bubble in a domain with a length of  $5\text{mm}$  in all directions. The grid spacing is equidistant in the bubble region with 96 computational cells over the initial bubble radius. Grid stretching is applied in the far-field. Outlet boundary conditions are imposed at the far-field bounds of the computational domain by setting gradients across the boundary to zero. Compressibility is taken into account for both phases and the initial material states are

$$\begin{aligned} \text{vapor: } p &= p_{sat} = 0.0234\text{bar}, T = 293\text{K}, \\ \text{water: } p &= p_{li} = 1\text{bar}, T = 293\text{K}. \end{aligned} \quad (26)$$

Initial velocity is zero everywhere. The initial densities are given by the corresponding equation of state. The accommodation coefficient is set to  $\lambda = 0.1$ . Figure 3 shows the evolution of the normalized bubble radius  $R^* = R/R_0$  over normalized time  $t^* = t/R_{Rayleigh}$ . The bubble radius  $R$  is calculated based on the bubble volume.

The good agreement with the theory demonstrates the ability of our method to predict the collapse dynamics of a single bubble. Small differences at later times (see also Sezal [14]), are most likely due to compressibility effects in the liquid that are not included within the theory and have also been observed in experiments [15].

## 4.2 Near-wall spherical vapor-bubble collapse

We investigate the collapse of a vapor bubble near a solid wall. As shown in Fig. 4, the initial bubble radius is 400  $\mu\text{m}$  and we consider three different wall positions A, B and C. We take advantage of symmetries and compute only one quarter of the bubble. The grid spacing is equidistant in the bubble region with 100 computational cells over the initial bubble radius. Grid stretching is applied in the far-field. Outlet boundary conditions are imposed at  $x, y, z = 10 \text{ mm}$ . Data are mirrored on the (X-Y)- and (Y-Z)-plane for visualization. Both fluids have a common temperature of 293.0 K which is the saturation temperature corresponding to the initial vapor pressure of 0.0234 bar and initial liquid pressure is 100 bar. The accommodation coefficient is taken as  $\lambda = 0.01$  since Marek & Straub [16] show that  $\lambda$  decreases with increasing liquid pressure.

For all configurations, the vapor bubble shrinks slowly during the initial period. The rapid stage of the bubble collapse starts with the development of a cavity, followed by the formation of a liquid jet. Two fundamentally different scenarios at the early stages of bubble collapse can be found. For a detached bubble or a bubble cut in the lower hemisphere, the collapse is initiated at the top of the bubble (Fig. 5 a,b). A fast liquid re-entrant jet develops and penetrates through the bubble in wall-normal direction (Fig. 6 a,b). For an attached bubble cut in the upper hemisphere, the collapse is initiated between wall and interface (Fig. 5 c) and a liquid jet develops radially towards the bubble center (Fig. 6 c).

The appearance of a secondary jet can be only observed with configuration B since the wall normal re-entrant jet is deflected at the wall and interacts with the remaining bubble ring (Fig. 6 b, dashed lines). This secondary jet is radially symmetric and develops from the symmetry axis outwards in wall-parallel direction. For configuration A no secondary jet develops as the residual bubble ring is not attached to the wall. Figure 7 gives a three-dimensional visualization of the bubble shape during the stage of the three different liquid jets.

The first occurrence of extreme pressure magnitudes coincides with jet breakdown. For cases A and B with a wall-normal re-entrant jet, the observed maximum wall pressures are of comparable magnitude of about 100 times the initial pressure. Slightly larger values for the detached bubble can be attributed to a larger jet velocity. Looking at wall-parallel radial jets, one has to distinguish between the outward-pointing secondary jet of configuration B and the inward pointing primary jet of configuration C. In the latter case, the liquid is gradually compressed while being transported towards the symmetry axis, where maximum pressure occurs. The maximum pressure after inward-pointing, wall-parallel jet breakdown is about six times larger than that for a wall-normal jet. For the outward-running, wall-parallel secondary jet of configuration B, extremely low pressure is observed inside the jet as an expansion of the liquid further decreases the pressure of the high-velocity jet. After the jet breaks down, the liquid pressure increases, but remains significantly smaller than for the inward-pointing jet.

During the final stage of the bubble collapse, two different scenarios occur. For cases A and C, the residual vapor bubble is

detached after jet breakdown. Thus, the maximum pressure due to final bubble collapse occurs away from the wall. The emitted shock wave impinges on the wall with reduced magnitude, and the wall pressure does not reach the level observed for jet breakdown. The second scenario can be found for configuration B. After primary and secondary jet breakdown, a residual vapor ring remains at the wall. This ring is surrounded by high pressure which initiates the final collapse radially towards the symmetry axis. Liquid is compressed towards the center region resulting in large pressure with a maximum at the symmetry axis of about 400 times the initial pressure.

## 4.3 Near-wall ellipsoidal vapor-bubble collapse

The ideal situation of spherical vapor bubbles hardly applies to technical applications, where cavitation bubbles are most likely non-spherical. A moderate increase of geometrical complexity by considering an ellipsoidal vapor bubble near a solid wall allows for an initial estimate on the effect of geometry variations on bubble collapse. As it was found previously that configuration C of a spherical vapor bubble leads to the largest wall pressure, we consider a similar configuration with the ellipsoidal bubble. The equivalent full (non-cut) ellipsoid is rotationally symmetric about the x-axis and has the same volume as the spherical bubble of the previous section. We set the length of the semi-major axis to  $a = 3/2 R_{\text{sphere}} = 600 \mu\text{m}$ , where  $R_{\text{sphere}} = 400 \mu\text{m}$  is the initial radius of the corresponding sphere. The volume is kept constant by choosing  $b = \sqrt{2/3} R_{\text{sphere}} \approx 326.6 \mu\text{m}$  as the length of the semi-minor axis. We use the initial material states given in § 4.2 and similar grid spacing. Again, only one quarter of the problem is simulated due to the sectional symmetry of the setup. For presentation, data are extended to the full domain.

For the ellipsoidal bubble the contact angle varies along the circumference. Where the contact angle is small, we expect weak expansion and therefore strong acceleration of the interface. As the contact angle is always below  $90^\circ$  the overall behavior resembles that of configuration C. Along the semi-major axis with smallest contact angle, a jet has already developed in Fig. 8 (a).

Figure 8 (b) shows two different wall-parallel jets. The first jet corresponds to that found already for the spherical bubble. This rotationally symmetric jet leads to a cavity between wall and interface along the circumference of the bubble. The second jet is a consequence of the initial asymmetry. It penetrates into the bubble along the semi-major axis, similarly as a wall-parallel re-entrant jet. It dominates the further bubble collapse as its velocity is larger than that of the first jet.

The axial jet first breaks through the bubble area in the symmetry plane (Fig. 8 c) and two bubble fragments are generated. When the axial jet breaks down, the pressure increases rapidly to more than 100 times the initial pressure. The high pressure between the two bubble fragments initiates the collapse of the residual vapor bubble. The maximum wall pressure is reached at final collapse of the remaining bubble parts. With more than 600 times the initial pressure, the wall pressure is of similar magnitude as for the spherical bubble although the collapse mechanisms are significantly different.

## 5. CONCLUSIONS

We have presented a conservative sharp-interface model for multi-fluid flows, working on arbitrary Cartesian grids. Introducing a phase change model, based on a non-equilibrium assumption at the phase interface, we treat evaporation and condensation.

Computational results for the collapse of a spherical vapor bubble close to a solid wall have been discussed for three different bubble-wall configurations. For a detached bubble and a bubble cut by the wall in its lower hemisphere, we found the appearance of the well known wall-normal re-entrant jet. For the latter configuration, also a secondary radial and wall-parallel jet was found. If the bubble is attached, but cut by the wall in its upper hemisphere, the developing jet is wall-parallel and compresses the liquid towards the axis of symmetry. Additional results for the collapse of an ellipsoidal vapor bubble have shown, that the collapse mechanisms is highly dependent on initial asymmetries in the bubble shape.

## ACKNOWLEDGMENTS

Financial support has been provided by the German Research Council (Deutsche Forschungsgemeinschaft - DFG). Computational resources have been provided in large part by the Leibniz Rechenzentrum Munich.

## REFERENCES

- [1] RAYLEIGH, L. (1917) On the pressure developed in a liquid during the collapse of a spherical cavity. *Phil. Mag.* **34**, 94-98.
- [2] KORNFELD, M. & SUVOROV, L. 1944 On the destructive action of cavitation. *J. Appl. Phys.* **15**, 495-506.
- [3] LINDAU, O. & LAUTERBORN, W. 2003 Cinematographic observation of the collapse and rebound of a laser-produced cavitation bubble near a wall. *J. Fluid Mech.* **479**, 327-348.
- [4] HU, X. Y., KHOO, B. C., ADAMS, N. A. & HUANG, F. L. 2006 A conservative interface method for compressible flows. *J. Comp. Phys.* **219**, 553-578.
- [5] JOHNSON, E. & COLONIUS, T. 2009 Numerical simulations of non-spherical bubble collapse. *J. Fluid Mech.* **629**, 231-262.
- [6] SZERI, A. J., STOREY, B. D., PEARSON, A. & BLAKE, J. R. 2003 Heat and mass transfer during the violent collapse of nonspherical bubbles. *Phys. Fluids* **15**(9), 2576-2586.
- [7] HU, X. Y., ADAMS, N. A., JOHNSON, E. & IACCARINO, G. 2008 Modeling full-Mach-range cavitating flow with sharp interface model. *Proceedings of the 2008 Summer Program CTR*, Stanford, CA.
- [8] FEDKIW, R., ASLAM, T., MERRIMAN, B. & OSHER, S. 1999 A non-oscillatory Eulerian approach to interfaces in multimaterial flows (the ghost fluid method). *J. Comp. Phys.* **152**, 457-492.
- [9] TORO, E. F. 1997 *Riemann Solvers and Numerical Methods for Fluid Dynamics: A Practical Introduction*. Springer.
- [10] HU, X. Y., KHOO, B. C., ADAMS, N. A. & HUANG, F. L. 2006 A conservative interface method for compressible flows. *J. Comp. Phys.* **219**, 553-578.
- [11] FUJIKAWA, S. & AKAMATSU, T. 1980 Effects of the non-equilibrium condensation of vapour on the pressure wave produced by the collapse of a bubble in a liquid. *J. Fluid Mech.* **97**, 481-512.
- [12] SCHRAGE, R. W. 1953 *A Theoretical Study of Interphase Mass Transfer*. Columbia University Press.
- [13] YOUNG, F. R. 1999 *Cavitation*. Imperial College Press.
- [14] SEZAL, I. H. 2009 *Compressible Dynamics of Cavitating 3-D Multi-Phase Flows*. PhD thesis, Technische Universität München, Verlag Dr.Hut.
- [15] HUNG, C. F. & HWANGFU, J. J. 2010 Experimental study of the behaviour of mini-charge underwater explosion bubbles near different boundaries. *J. Fluid Mech.* **651**, 55-80.
- [16] MAREK, R. & STRAUB, J. 2001 Analysis of the evaporation coefficient and the condensation coefficient of water. *Int. J. Heat Mass Transfer* **44**, 39-53.



# **The effect of liquid temperature on cavitation bubble collapse**

H. Söhnholz, T. Kurz, W. Lauterborn

The temperature dependence of single bubble collapse in water is investigated experimentally. Single bubbles are produced by focussing a pulsed laser into a cuvette containing heated water at controlled temperature. The bubble collapse is investigated optically using a camera with short exposure time and acoustically with a hydrophone. The temperature of the surrounding liquid has a strong influence on the bubble dynamics, because the vapor pressure increases significantly with temperature. It is found in the experiments that the high vapor content inside the bubble (compared to the amount of non-condensable gas) results in a milder bubble collapse. A solid wall placed near the bubble induces aspherical collapse which involves the formation of shock waves and a liquid jet. The aspherical collapse is strongly dependent on the stand-off distance bubble-wall. Again, the water temperature has an effect on shock wave emission and jet formation with the emitted shock wave amplitudes being smaller at elevated temperatures.

## **Collapse Detection in Compressible 3-D Cavitating Flows and Assessment of Erosion Criteria**

Michael Mihatsch\*, Steffen J. Schmidt, Matthias Thalhamer, Nikolaus A. Adams  
Institute of Aerodynamics and Fluid Mechanics, Technische Universität München  
Boltzmannstr. 15, D-85748 Garching, Germany

Romuald Skoda, Uwe Iben  
Robert Bosch GmbH, Corporate Research and Advance Engineering - CR/ARH,  
Postfach 106050, D-70049 Stuttgart, Germany

\* Michael.Mihatsch@aer.mw.tum.de

### **ABSTRACT**

The objective of the present investigation is the numerical prediction of the potential of a flow to inflict the surface damage by cavitation. For this purpose, physical criteria are derived that detect and quantify relevant flow phenomena. In particular, we present a numerical approach to trace isolated collapses of vapor clouds during the numerical simulation of the flow. The suggested “collapse detector” provides the frequency of collapses, their positions and resulting maximum pressures as well as the maximum condensation rate of each event. These data, together with the maximum wall pressure, allow for an automatic indication of erosion-sensitive areas.

The employed flow solver CATUM (CAvitation Technische Universität München) is a density-based 3-D finite volume method equipped with a Low-Mach-number consistent flux function. All fluid components (liquid, vapor, saturated mixture) are either modeled by closed-form equations of state or by look-up tables.

To assess the novel approach we simulate two suitable nozzle-target flows for which experimental data are available. The investigated configurations differ by their characteristic length and time scales as well as by the working fluids (water and a Diesel-like test fluid). A comparison of numerically predicted collapse events with the experimentally observed areas of cavitation erosion substantiates the proposed methodology. The obtained data represent a time-history of collapse events together with their position and strength and may be used to estimate erosion rates.

### **1. INTRODUCTION**

Hydrodynamic cavitation and cavitation erosion are well known phenomena in naval engineering, hydraulic machinery, fuel injection systems and process engineering [1, 2]. Distinctive examples include cavitation on the suction side of propeller blades and cavitation within micro boreholes of diesel injectors. The basic mechanisms of hydrodynamic cavitation are flow-induced evaporation due to the pressure drop of an accelerated liquid and inertia controlled recondensation of liquid-embedded vapor bubbles due to pressure recovery. The collapse-like recondensation results in the generation of shock waves that are

supposed to constitute the main mechanism of cavitation erosion. These shocks propagate approximately with the speed of sound  $c \approx O(10^3)$  m/s of the liquid and their intrinsic time scale is about 2 orders of magnitude smaller than the time scale of the underlying shear flow.

Since the simulation of erosive collapses in cavitating flows requires the resolution of both time scales, time step-sizes on the order of nanoseconds are inevitable and millions of time steps have to be computed to cover the characteristic time interval of the shear flow. It is neither reasonable to store the enormous amount of data generated by such a simulation, nor is it feasible to evaluate manually the data with respect to collapse characteristics and erosion aggressiveness. Instead, new approaches have to be developed that allow for automatic detection and evaluation of aggressive collapse events predicted by 3-D unsteady simulations of cavitating flows.

### **2. UNDERLYING NUMERICAL MODEL**

We employ our flow simulation code CATUM (CAvitation Technische Universität München [3]), which is a density based finite volume method employing a Low-Mach-number consistent flux function and an explicit time marching procedure. The spatial reconstruction of the velocity field is a WENO-3 procedure; density and internal energy are reconstructed by monotonic TVD limiters (“minmod”). Time marching is performed through an explicit low storage 4-step Runge-Kutta method with an optimized stability region. The combination of both methods results in a 2<sup>nd</sup> order numerical approach in space and time for smooth flow, and it ensures a sharp representation of discontinuous flow features such as shocks and contact waves. In this investigation we focus on the simulation of inertia-driven effects and wave dynamics and we neglect viscous effects. Hence, the governing equations are the compressible Euler equations.

The working fluids can be characterized by closed-form equations of state, or for complex fluids by look-up tables. In order to allow for the simulation of shock formation and wave propagation, the compressibility of the fluids (liquid and vapor) is taken into account. Hence, the numerical time step is necessarily proportional to the ratio of the smallest length scale

(minimum grid size) and the fastest signal speed ( $\sim$  speed of sound of the liquid).

The phase transition model is based on local equilibrium assumptions for pressure, temperature and specific Gibbs functions. We have observed that this assumption is justified since most of technically relevant hydrodynamic cavitation processes occur close to the equilibrium vapor pressure. Although this observation is questionable for incipient cavitation, it applies to developed cavitating flows, such as investigated within the presented research work. Previous investigations [4] show that CATUM is able to predict even delicate flow features, such as irregular break-up patterns of partial cavities of developed cavitating flows.

We adopt body-fitted hexahedral grids to discretize the flow field. The data structure is based on local blocks and a pre-processor load balance strategy is utilized to obtain approximately linear scaling on multi-processor systems.

### 3. MODELING AND IMPLEMENTATION OF EROSION INDICATORS AND COLLAPSE DETECTORS

Shock waves initiated by violent cloud collapses can generate intense pressure peaks on the order of several thousand bars. If such a shock wave is emitted sufficiently close to a solid surface, its impact on the solid material may result in dynamic loads that result in material fatigue. Hence, instantaneous maximum loads may provide an indication of locations where erosion is likely to occur. Therefore, monitoring the maximum pressure of each computational cell during the whole simulation is one efficient approach to detect erosion sensitive areas within the flow field and especially along solid walls. Although this procedure was applied successfully in previous investigations [5-6], it has several obvious limitations: The approach neither provides information about the frequency of collapse events, nor does it allow to distinguish between stagnation pressures and instantaneous maximum loads with durations of only a few microseconds. However, even this limited amount of achievable information allows for the indication of erosion-sensitive areas.

A considerable improvement of the maximum pressure approach is presented and evaluated in a companion paper [7]. Here, the amount of time instants where a predefined threshold value of the pressure (or the force) is exceeded is used to estimate the erosion probability.

Our recent development focuses on a more detailed approach that we denote as “collapse detector”. The concept involves the derivation of a set of physical criteria to detect collapses of isolated clouds and to characterize the strength of the generated shock waves as predicted by our numerical simulations. Figure 1 shows a schematic of consecutive stages of a cloud collapse. In the lower part of this figure the average divergence of the velocity field around the collapsing cloud is depicted.

The onset of condensation results in the formation of a velocity field that is approximately directed towards the center of the cloud – similarly to an elementary sink flow. Thus, the divergence of the velocity field is negative and decreasing. Since we assume that the specific Gibbs functions remain in equilibrium, and due to disregarding solved or dissolved gas, the pressure within the cloud remains approximately constant.

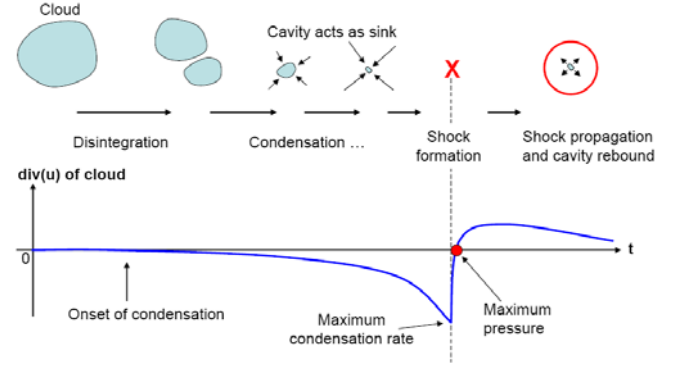


**Figure 1:** Sketch of consecutive stages of the collapse of a vapor cloud together with the temporal evolution of the divergence of the velocity field.

Hence, the surrounding liquid is further accelerated towards the center of the cloud until the vapor completely condenses at the last stage of the collapse. At this instant in time, the inertia of this sink flow results in a massive increase of the pressure. The maximum pressure is reached when the mass flow towards the center vanishes. At that point, the divergence changes its sign and the negative radial pressure gradient leads to an outward directed velocity field. Consequently, the pressure at the center decreases and may even lead to a re-evaporation of the liquid (rebound of the cavity). These considerations motivate the following definition of a numerical “collapse detector”:

- \* We denote as “candidates” such computational cells where the vapor volume content condenses completely during the last time step. If the surrounding cells of a “candidate” contain liquid only, an isolated collapse is detected.
- \* Once a collapse is detected, the maximum pressure is generated at that instant in time when the divergence of the velocity field changes its sign.
- \* The strength of the collapse is characterized by its maximum (negative) divergence and its maximum pressure.

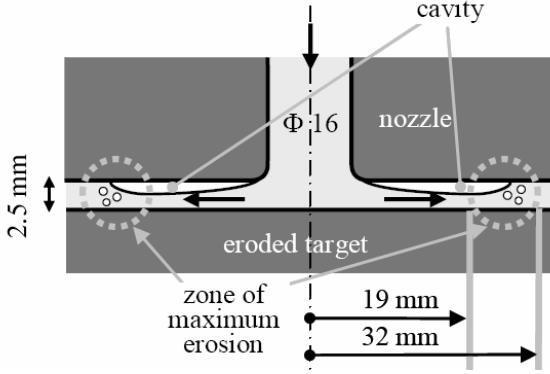
The main advantages of the “collapse detector” as compared to the maximum pressure approach are as follows:

- \* The collapse detector automatically distinguishes between collapse-induced maximum pressures and high pressures at stagnation points or due to wave interaction.
- \* The number of collapse events as well as their positions and strength provide important information about a possible stress profile the material is exposed to. This information can be used to estimate erosion rates.

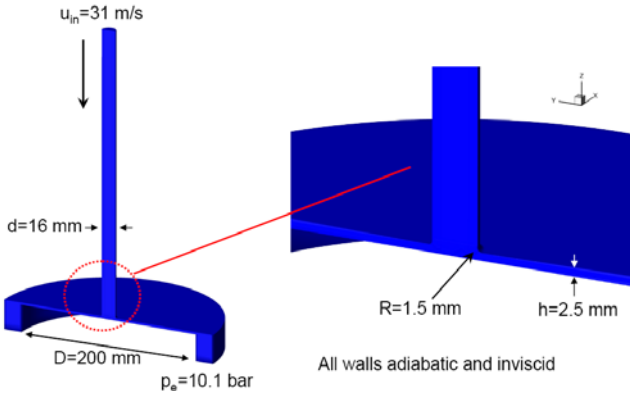
Special emphasis is put on those collapse events that occur close to solid surfaces. Since the detected minimum divergence is comparable to the detected maximum pressure for the investigated test cases, we focus on the presentation of the maximum collapse pressure exclusively. However these two quantities may not necessarily be equivalent in other test cases.

#### 4.1 AXISYMMETRIC NOZZLE-TARGET FLOW

We simulate an experimentally investigated nozzle-target flow [8] to evaluate the numerical predictability of erosion-sensitive areas. The experimental setup results in an axisymmetric stagnation flow as shown in Figure 2. At the exit of the nozzle the fluid accelerates along a small radius and forms a radial cavitation pocket. Collapse-induced erosion is observed experimentally within an annulus at the surface of the target disc. The remaining devices are manufactured out of highly resistant material.



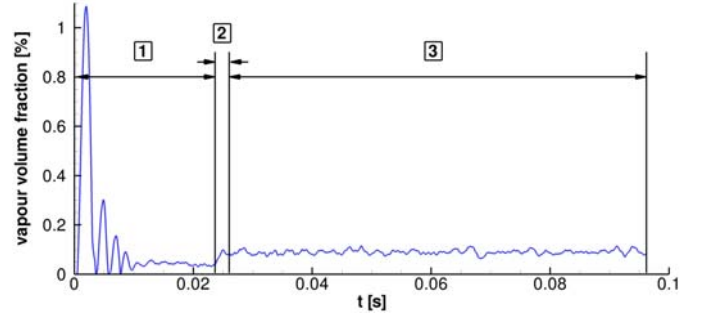
**Figure 2:** Sketch of the experimental setup [8].



**Figure 3:** Cut through the numerical domain and imposed boundary conditions. The grid consists of  $5 \cdot 10^5$  cells in 56 blocks and the numerical time step-size is  $\Delta t \approx 2.8 \cdot 10^{-8}$  s. The simulation is performed for the whole  $360^\circ$  domain.

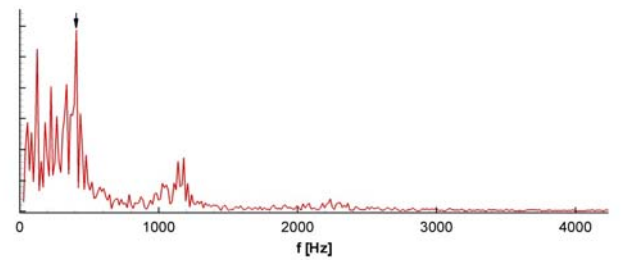
Figure 3 shows a cut through the computational domain. In accordance with the experiment, water at approximately room temperature enters the nozzle with the inlet velocity  $u_{in} = 31$  m/s. An asymptotic pressure boundary condition  $p_e = 10.1$  bar is imposed at the exit of a circular reservoir attached at a radial distance of 100 mm. All solid boundaries are treated as inviscid adiabatic walls. The computational grid consists of  $5 \cdot 10^5$  body-fitted hexahedrons structured in 56 blocks. The thermodynamic properties of liquid water are specified by a modified Tait law, saturated two-phase regions are modeled by polynomial fits of the IAPWS [9] data and pure vapor is modeled by an adopted ideal gas law.

Figure 4 shows the time history of the vapor volume within the computational domain. The time intervals 1 and 2 correspond to a grid-sequencing-technique where the numerical solution is initially obtained on a coarse grid (interval 1) and interpolated to the fine grid. Only a short time interval (interval 2) is required until the solution on the fine grid establishes. The analyzed part of the simulation (time interval 3) consists of  $2.5 \cdot 10^6$  time steps with a time step-size of  $\Delta t \approx 2.8 \cdot 10^{-8}$  s. This corresponds to a simulated physical time interval of  $7 \cdot 10^{-2}$  s. The computation required 3920 CPU-hours (70 hours on 56 cores, Intel Nehalem-EP based 8-way nodes).



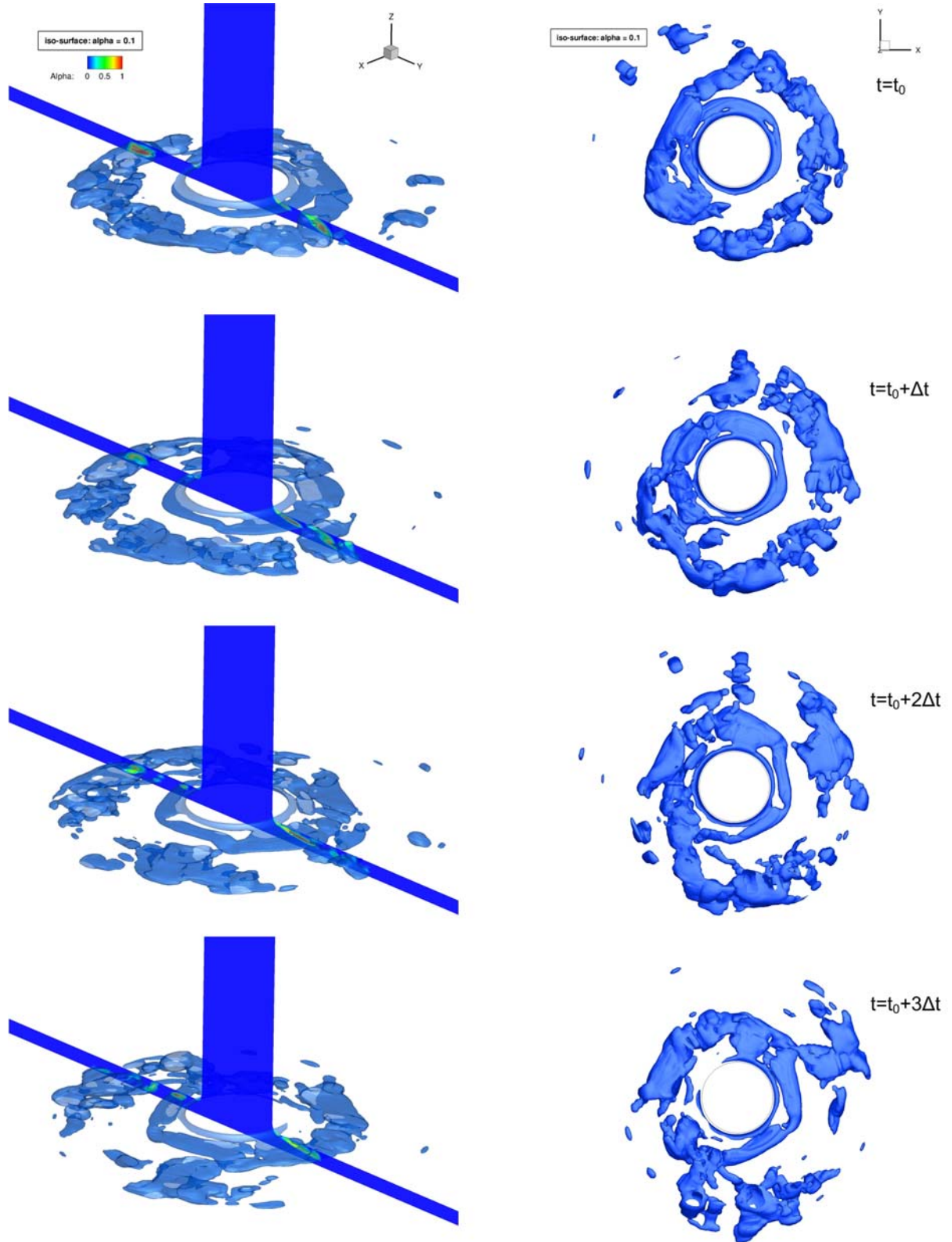
**Figure 4:** Time history of the vapor volume fraction referred to the volume of the whole computational domain. Interval 1: Preliminary calculation on a coarse grid. Interval 2: Interpolation to the fine grid. Interval 3: Analyzed part of the simulation on the fine grid.

Figure 6 shows instantaneous vapor structures at 4 equidistant instants in time ( $\Delta t = 8.4 \cdot 10^{-5}$  s). Blue iso-surfaces correspond to a vapor volume fraction  $\alpha = 0.1$ . We observe the onset of sheet-cavitation at the rounding of the nozzle outlet. The fragmentation of the sheet and its transient shedding is strongly non-uniform in circumferential direction. The collapse of the vapor structures is enforced by the positive radial pressure gradient.



**Figure 5:** FFT of the time history of the vapor volume fraction.

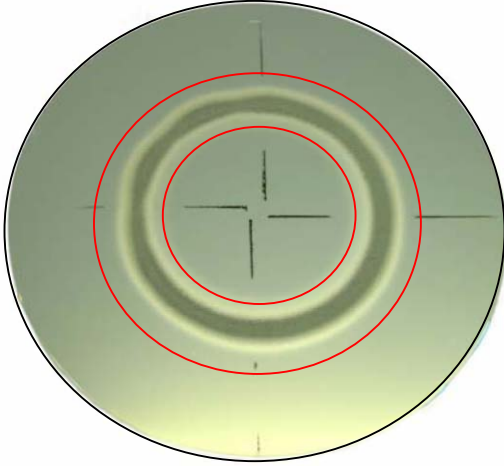
Figure 5 depicts the spectrum of the integrated vapor volume. The dominant frequency is 408 Hz (arrow), which corresponds to the radial shedding. Lower frequencies might be circumferential modes. The highest well defined frequencies at 1139 Hz and 1182 Hz are supposed to be related to the collapse of small clouds.



**Figure 6:** Iso-surfaces of the vapor volume fraction ( $\alpha = 0.1$ ) at 4 equidistant instants in time ( $\Delta t = 8.4 \cdot 10^{-5}$  s). Left side: perspective view with an additional axial cut plane showing the contour of the vapor volume fraction. Right side: top view.

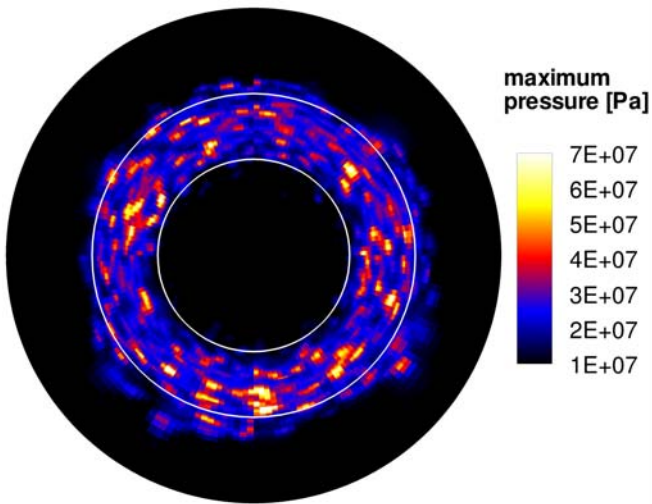


Figure 7 shows a photograph (from an angle) of an eroded target disc. The damage exhibits an almost perfect circular shape. Red circles indicate the area where damage was found in the experiment [8].



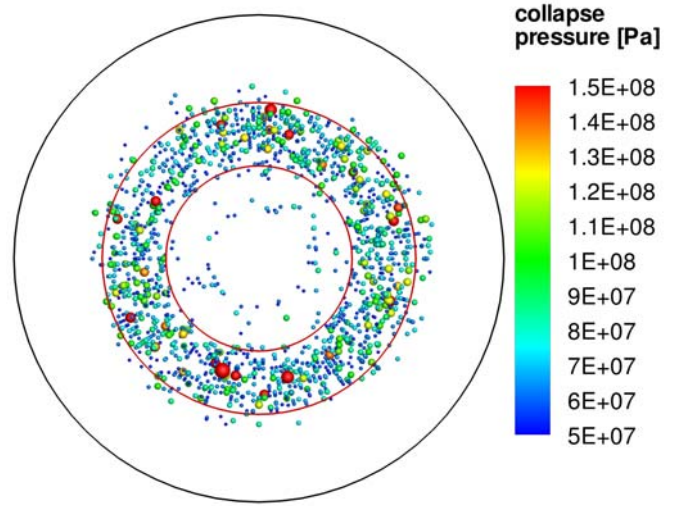
**Figure 7:** Photograph of an eroded target from the experiment – slightly perspective view [8]. According to experimental observation [8], erosion damage occurs within  $r=19$  mm and  $r=31$  mm (red circles).

Figure 8 shows the maximum pressure for each computational cell on the target disc recorded during the analysis interval (interval 3). Only pressures about one order of magnitude higher than the stagnation pressure are shown, the highest recorded value is  $1.56 \cdot 10^8$  Pa. We observe a convincing analogy of the cell-wise maximum pressure and the experimentally detected areas of erosion damage. However, further investigations using much longer analysis intervals are required to improve the statistical relevance of the prediction.

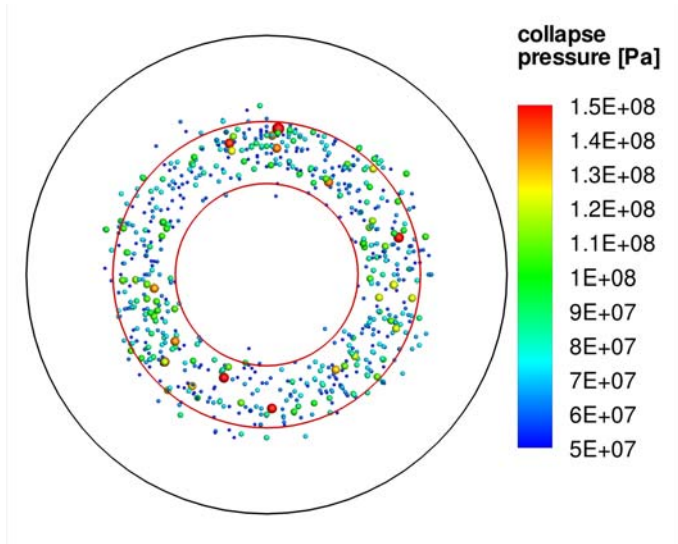


**Figure 8:** Maximum pressure observed in the simulation on the target during the analysis interval ( $\Delta t=7 \cdot 10^{-2}$  s).

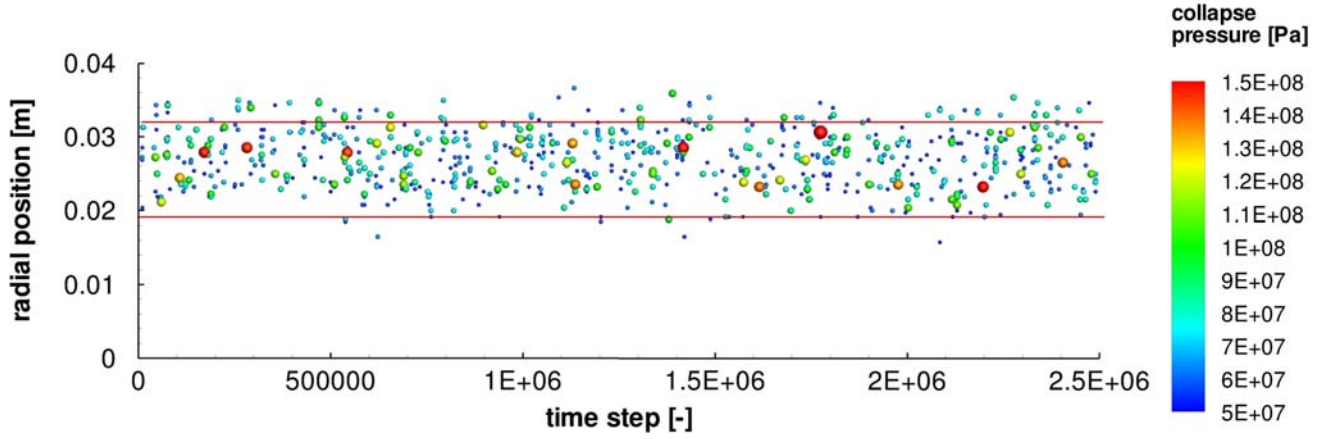
Figure 9 shows the detected collapses within the gap between the nozzle and the target disc. The collapses are indicated as spheres that are plotted at the position of their occurrence. The diameter of each sphere and its color represent the collapse pressure. Most of the collapses are found within the marked area. In Figure 10 only collapses in a distance of 1 mm to the target are visualized since near-wall collapses are supposed to be particularly erosive. Compared to Figure 9 the agreement with the experiment is even improved.



**Figure 9:** Visualization of all collapses detected during the analysis interval ( $\Delta t=7 \cdot 10^{-2}$  s). Each collapse is represented by a sphere at the position of its occurrence. Size and color represent the collapse pressure.



**Figure 10:** Visualization of all collapses detected during the analysis interval ( $\Delta t=7 \cdot 10^{-2}$  s) at a distance of  $\leq 1$  mm to the target. Each collapse is represented by a sphere at the position of its occurrence. Size and color represent the collapse pressure.



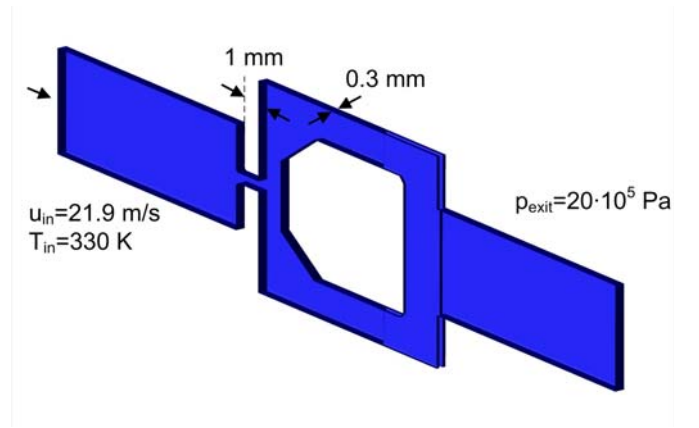
**Figure 11:** Time history of collapses detected at a distance of  $\leq 1$  mm to the target during the analysis interval ( $\Delta t = 7 \cdot 10^{-2}$  s). The diagram shows the radial position of each detected collapse against the time of its occurrence. Size and color of the collapses represent the collapse pressure.

Figure 11 shows the radial positions of all collapses within a distance of 1 mm to the target plotted against the time of their occurrence. It can be seen that all violent collapses (red and yellow spheres) are located within the marked area. The lower bound at  $r=19$  mm is perfectly captured by the simulation while the upper bound might be slightly overestimated. Assuming that the positions of collapses are statistically distributed in circumferential direction, this time history represents a possible load profile the material might be exposed to over a long time period.

#### 4.2 PLANAR NOZZLE-TARGET FLOW

As a second test case we simulate a planar nozzle-target flow as depicted in Figure 12. The setup was experimentally investigated in [10-11] and [12]. A cavitating jet is directed onto a blunt target body that is located at 1 mm downstream of the nozzle exit. The aluminum target is fixed at a centered position by a C-shaped holder, which occupies one third of the depth of the channel. For optical accessibility, the setup is mounted between two quartz glass windows.

According to the experiment, a Diesel-like test fluid at a temperature of 330 K enters the domain with an inlet velocity of 21.9 m/s. At the exit of the numerical domain an asymptotic pressure boundary condition of 20 bars is applied. All solid boundaries are modeled as inviscid adiabatic walls. In this case, the thermodynamic properties of the working fluid are defined by look-up tables. The computational domain consists of  $1.7 \cdot 10^6$  body fitted hexahedrons structured in 110 blocks. Again, a grid-sequencing-technique is applied to obtain an initial solution. The analyzed part of the simulation consists of  $3.5 \cdot 10^6$  time steps with a time step-size of  $\Delta t \approx 1.2 \cdot 10^{-9}$  s, resulting in a physical time interval of  $4.2 \cdot 10^{-3}$  s. The computation consumed 9212 CPU-hours (82 hours on 112 cores, Intel Nehalem-EP based 8-way nodes). The inherent three dimensional character of the cavitating flow behind the nozzle exit requires a full 3-D simulation. Concerning the nozzle flow itself, a 2-D investigation is performed and analyzed by [7].



**Figure 12:** Numerical setup of the planar nozzle-target flow and imposed boundary conditions. The grid consists of  $1.7 \cdot 10^6$  cells in 110 blocks and the numerical time step-size is  $\Delta t \approx 1.2 \cdot 10^{-9}$  s.

In Figure 13 the experimental setup is shown before (left) and after a runtime of 10 hours (right) for two successive runs with target bodies of different surface roughness. The rear parts of both flanks of the target body are seriously damaged (arrows). In case of initially rough surfaces, erosion damage is observed at the front part of the flank, while this is not the case for the initially smooth target. Independently of the specific surface properties, the erosion aggressiveness of the flow is higher on the rear part of the flank than on the front part. Additionally, two gray spots indicated by red circles show the formation of erosive damage on the quartz glass side walls.

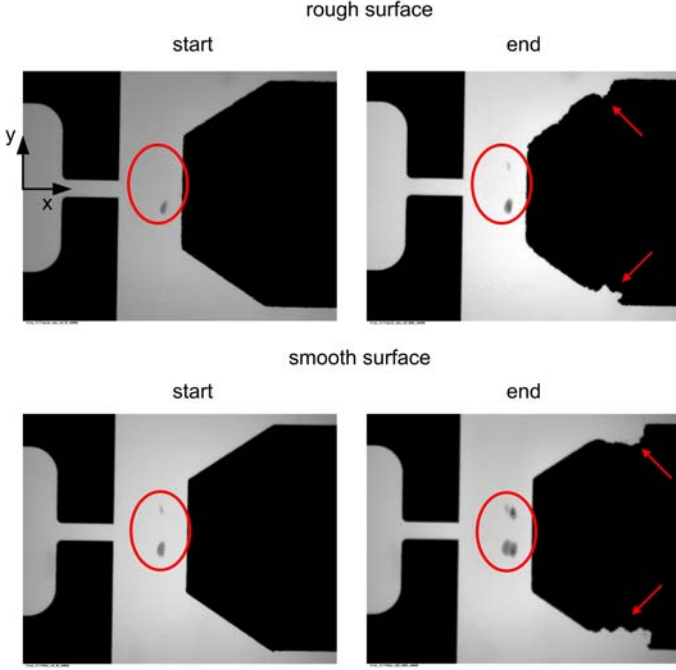


**Figure 13:** Experimental setup at the beginning and at the end of two consecutive runs. The surface roughness of the aluminum target strongly differs for both runs. Circles indicate erosion damage at the quartz glass side walls; arrows mark serious damage of the target body observed in both runs. Only the body with rough surface is damaged at the front part of the flanks.

Figure 14 shows instantaneous two-phase structures at 3 consecutive time instants with  $\Delta t = 1.2 \cdot 10^{-4}$  s - blue iso-surfaces correspond to a vapor volume fraction of  $\alpha = 0.1$ . One observes a stable sheet cavitation originating from the inlet of the nozzle. The shear layer downstream of the nozzle exit leads to the break-up of the cavity and to the formation of isolated vapor structures. The flow field behind the nozzle is highly transient in all spatial directions and predominantly asymmetric. The violent collapse of these patterns is enforced by a strong positive pressure gradient towards the stagnation point in front of the target body. Additional collapses occur at the flanks of the aluminum target. Both types of collapses will be analyzed with respect to their erosion aggressiveness in the following subsection.

We focus our analysis on the domains “1” and “2” as depicted in Figure 15. Domain “1” corresponds to the flank of the target and domain “2” contains the stagnation-point region. For presentation purposes the 3-D data generated by the collapse detector is post-processed as follows. We assume comparable distributions of collapses on the upper and on the lower half of the target, as well as in channel-depth direction. Thus, we project all collapses to the upper half of the setup and neglect the channel-depth position by  $(x, y, z) \rightarrow (x, |y|)$ . The resulting 2-D data are plotted against time to indicate a time history of collapse events (similar to Figure 11).

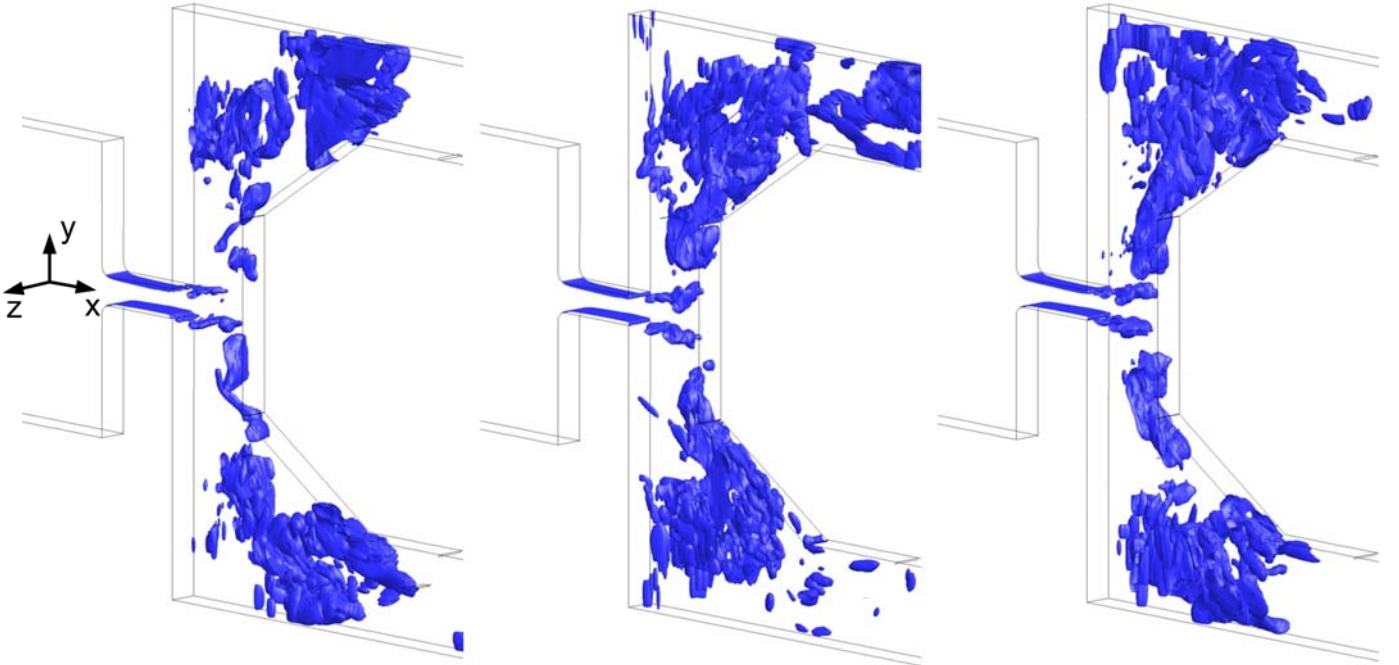


**Figure 14:** Perspective view of iso-surfaces of the vapor volume fraction ( $\alpha = 0.1$ ) at 3 equidistant instants in time ( $\Delta t = 1.2 \cdot 10^{-4}$  s).



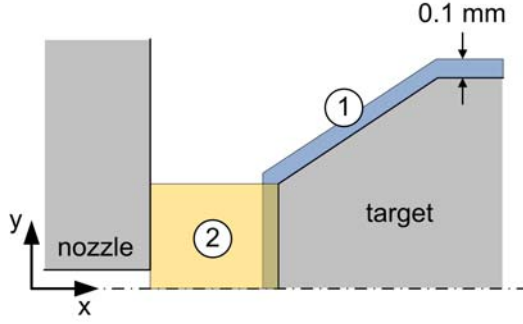


**Figure 15:** Schematic of the nozzle-target setup and definition of domains “1” and “2”.

Figure 16 shows a time history of all collapses detected within a distance of less than 0.1 mm away from the target body (domain “1” as specified in Figure 15).

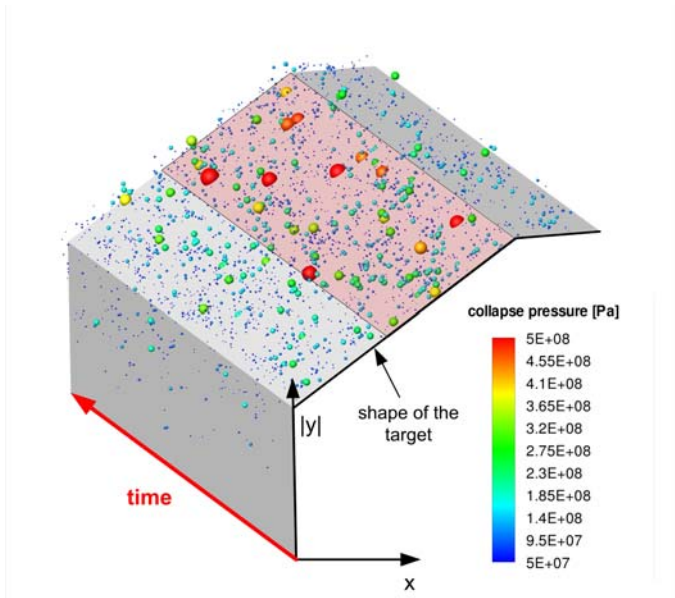


**Figure 16:** Time history of those collapses that are less than 0.1 mm away from the target (domain “1”); x-axis: x-coordinate; y-axis: absolute value of the y-coordinate; z-axis: time of the collapse event.

One observes that all strong collapses ( $p_{\text{collapse}} > 4 \cdot 10^8$  Pa) are detected within the downstream part of the flank of the target (marked area). The size of the predicted area is slightly overestimated as compared to the region of the experimentally observed serious damage. However, the statistical relevance of the prediction might be improved by extending the analysis interval. Although the front part of the flank is affected by a comparable number of collapses, the collapse pressure of the observed events is significantly reduced as compared to events occurring on the rear part. Again, this time history could be used to approximate a stress profile to which the material might be exposed to over a long time period. Currently we do not take into account the erosion-induced modification of the target

geometry. Since we know that this effect can be of great importance, we like to point out that a more appropriate experimental counterpart to the present investigation would be a pitting test.

The strongest collapses of the entire flow field are detected within domain “2”, especially ahead and slightly upstream of the stagnation point. To underline the high aggressiveness of the flow within domain “2” as compared to domain “1”, Figure 17 shows only those collapses where the resulting maximum pressure exceeds  $4 \cdot 10^8$  Pa.

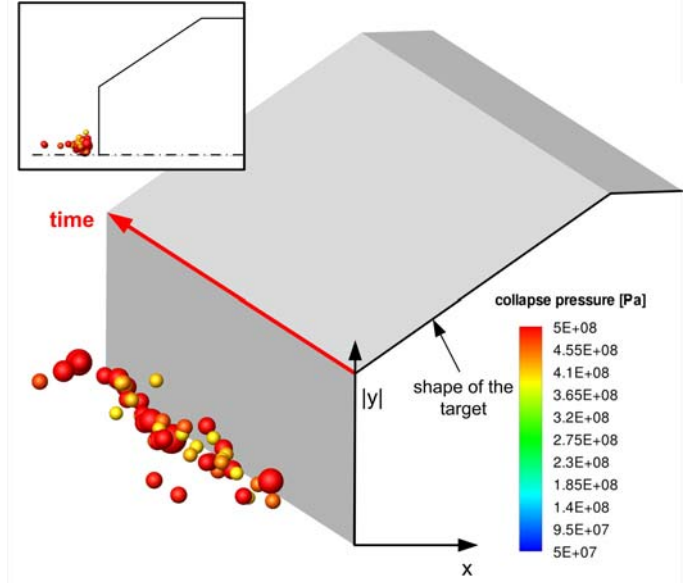


**Figure 17:** Time history of collapses close to the stagnation-point (domain “2”). The visualization shows only violent collapses with a collapse pressure  $> 4 \cdot 10^8$  Pa; x-axis: x-coordinate; y-axis: absolute value of the y-coordinate; z-axis: time of the collapse event.

Taking the frequency of occurrence of violent collapses into account, this position is predicted to have high erosion potential. However, it is important to note that the effective maximum pressure at the target surface is approximately one order of magnitude smaller (due to the fast decay of the collapse intensity). Thus, we assume that the collapses related to the stagnation point flow do not result in significant erosion of the target body. It is much more reasonable to relate these collapses to the observed damage of the supposedly durable quartz glass windows. Both numerical predictions agree well with the experimental observations.

## 5. CONCLUSION

We present a novel approach referred as “collapse detector” for the numerical prediction of erosion-sensitive areas. Based on a set of physical criteria we detect and characterize isolated collapses of vapor structures within unsteady cavitating flows. The collapse detector is implemented into our flow solver CATUM, which enables the simulation of cloud collapses and the subsequent formation and propagation of shocks due to the

compressible treatment of the working fluids. By comparison of our results with two entirely different experiments we demonstrate the ability of the proposed methodology to predict the position of cavitation erosion. Additionally, we provide information about the relative strength and the time history of collapse events.

Currently, the significance of solved gas and its effect on cavitation erosion are investigated. Further research will focus on the comparison of our numerical predictions to experimental pitting tests, as well as the application of our collapse data to a material law as proposed by [13].

Moreover, we will apply our recently developed techniques to simulations of planar throttle flows as experimentally investigated in [10-11] and [12]. An investigation of the influence of the inlet-geometry, the pressure level, and the fluid temperature as performed in [7] is planned.

## ACKNOWLEDGMENTS

We like to thank Jean-Pierre FRANC for providing detailed information on his experimental setup (axisymmetric nozzle-target flow) as well as for fruitful discussions and suggestions.

## REFERENCES

- [1] Brennen, C.E., *"Cavitation and Bubble Dynamics"*, Oxford University Press, New York, 1995
- [2] Franc, J.-P., Michel, J.-M., *"Fundamentals of Cavitation"*, Kluwer Academic, Dordrecht, 2004
- [3] Schnerr, G.H., Sezal, I.H., Schmidt, S.J., *"Numerical Investigation of Three-dimensional Cloud Cavitation with Special Emphasis on Collapse Induced Shock Dynamics"*, Physics of Fluids, Vol. 20, Issue 4, 040703, 2008.
- [4] Schmidt, S.J., Thalhamer, M., Schnerr, G.H., *"Inertia Controlled Instability and Small Scale Structures of Sheet and Cloud Cavitation"* Proc. 7th CAV 2009 - 7th International Symposium on Cavitation, Ann Arbor, Michigan, USA, 16.8.- 21.8.2009, paper 17, CD-ROM publication, 2009.
- [5] Schmidt, S.J., Sezal, I.H., Schnerr, G.H., Thalhamer, M., *"Numerical Analysis of Shock Dynamics for Detection of Erosion Sensitive Areas in Complex 3-D Flows"*, Proc. WIMRC Cavitation Forum 2008, pp. 107-120, July 7 - 9, 2008, Warwick, UK, 2008.
- [6] Schmidt, S.J., Mihatsch, M., Thalhamer M., Egerer, C., Hickel, S., Adams, N.A., *"Assesment of Erosion Sensitive Areas via Compressible Simulation of Unsteady Cavitating Flows"*, International Workshop on ADVANCED EXPERIMENTAL AND NUMERICAL TECHNIQUES FOR CAVITATION EROSION PREDICTION, Grenoble, France, 1.3-2.3.2011, Post-Workshop CD.
- [7] Skoda, R., Iben, U., Morozov, A., Mihatsch, M., Schmidt, S., Adams, N., *"Numerical simulation of collapse induced shock dynamics for the prediction of the geometry, pressure and temperature impact on the cavitation erosion in micro channels"*, WIMRC Cavitation Forum 2011, Warwick, UK.
- [8] Franc, J.P., Riondet, M., *"Incubation Time and Cavitation Erosion Rate of Work-Hardening Materials. CAV2006"*, Wageningen, The Netherlands, September 2006
- [9] The International Association for the Properties of Water and Steam, <http://www.iapws.org/>
- [10] Iben, U., Morozov, A., Wolf, F., *"Laser-pulsed interferometry applied to high-pressure fluid flow in micro channels"*, Exp. Fluids, Vol. 50, pp. 597-611, 2011
- [11] Iben, U., Morozov, A., Winkelhofer, E., Skoda, R., *"Optical investigations of cavitating flow phenomena in micro channels using a nano second resolution"*, WIMRC Cavitation Forum 2011, Warwick, UK.
- [12] Winkelhofer, E., Kull, E., Kelz E., Morozov, A. *"Comprehensive Hydraulic and Flow Field Documentation in Model Throttle Experiments under Cavitation Conditions"*, ILASS-Europe 2001, Switzerland
- [13] Karimi, A., Leo, W., R., *"Phenomenological Model for Cavitation Erosion Rate Computation"*, Materials Science and Engineering, 95 (1987) 1-14

## **Assessment of the Prediction Capability of a Thermodynamic Cavitation Model for the Collapse Characteristics of a Vapor-Bubble Cloud**

Steffen J. Schmidt\*, Michael Mihatsch, Matthias Thalhamer and Nikolaus A. Adams

Institute of Aerodynamics and Fluid Mechanics  
Technische Universität München  
Boltzmannstr. 15, D-85748 Garching, Germany  
\*steffen.schmidt@aer.mw.tum.de

### **ABSTRACT**

A large number of numerical approaches have been developed for simulating cavitating flows. One model, which is recently applied within the CFD community, is the thermodynamic equilibrium approach. With this approach, the density and the internal energy are the only quantities necessary for specifying the mixture of liquid and vapor in a computational cell. The objective of the present investigation is to demonstrate that with thermodynamic equilibrium approaches even poorly resolved cloud-collapse events (typical for current CFD capabilities applied to complex systems) may provide important information for the prediction of erosion sensitive areas - provided that the temporal resolution of the numerical method is sufficiently high. By performing a sensitivity analysis of the main collapse characteristics with regard to the grid resolution we obtain an uncertainty estimation of the applied methodology.

### **1. INTRODUCTION**

The design of hydraulic machines such as ship propellers, turbines, pumps, injection systems and throttles requires model testing. In particular, the assessment of the probability of cavitation erosion is a severe challenge. However, model tests can be very costly and they may not always provide a perfect representation of the suggested real-scale machinery. A promising way to reduce costs would be reliable CFD simulations. However, the uncertainty of numerical approaches is often too big to provide a secure validation of a suggested design. One reason could be that CFD approaches provide too many degrees of freedom for the user. For example, the proper choice of the grid resolution and the choice of a suitable numerical discretization scheme are sometimes strongly case-dependent. Therefore, "best practice guides" can typically provide only hints instead of sustainable recommendations. In particular, thorough uncertainty quantification is mostly missing. With regard to cavitating flows, the choice of the cavitation model and of case-specific parameters enhances the complexity of modeling and simulation. Of course, expert knowledge is one important key to interpret and to evaluate numerical predictions. Surely, this knowledge will not be replaced by "computer decisions" within the next decade.

Our objective is to develop numerical methods and physically motivated models that reduce uncertainty as much as

possible. Additionally, widely applicable numerical methods must be robust with respect to varying operating conditions, and they should require as few predefined parameters as possible. Even if parameter-based models may outperform parameter-free models for selected test-cases, the quality of the prediction is often strongly dependent on a proper choice of the (mainly unknown) parameters. Hence, our focus relies on parameter-free models such as the thermodynamic equilibrium model.

During the last two decades, a wide variety of physical models have been developed for simulating cavitating flows. Typically, these models are incorporated into finite volume methods to obtain approximate solutions of the balance laws of mass, momentum and (sometimes) energy, together with the vapor volume fraction for each computational cell. Thereby, Eulerian-Eulerian approaches are predominant.

We define the following length-scale ratio  $\psi := \Delta_{\text{flow}} / \Delta_{\text{CFD}}$  where  $\Delta_{\text{flow}}$  is the characteristic length of two-phase structures and  $\Delta_{\text{CFD}}$  corresponds to the characteristic length of a computational cell. In case of  $\psi = \Delta_{\text{flow}} / \Delta_{\text{CFD}} \gg 1$ , two-phase structures are perfectly resolved by the computational cells, while for  $\psi = \Delta_{\text{flow}} / \Delta_{\text{CFD}} \ll 1$  the structures might be approximated as homogeneous mixture. A particular difficulty arises for  $\psi = \Delta_{\text{flow}} / \Delta_{\text{CFD}} \approx 1$ , since two-phase details are neither resolved, nor can they be represented as dispersed mixture. For simulation of cavitating flows, three entirely different Eulerian-Eulerian two-phase approaches will be briefly discussed.

#### **1) Sharp interface models (require $\psi = \Delta_{\text{flow}} / \Delta_{\text{CFD}} \gg 1$ )**

Sharp interface techniques are preferred to investigate the physics of a small number of bubbles in detail. Since the objective of sharp interface methods is to resolve physical phenomena within the bubble as well as along the bubble surface, the required numerical resolution  $\Delta_{\text{CFD}}$  is at least one or two orders of magnitude smaller than the typical diameter of a bubble  $\Delta_{\text{flow}}$ . However, this requirement results in an infeasibility of sharp interface methods to simulate cavitating flow problems with several thousands of bubbles, such as common cloud cavitation. Yet they might be perfectly adequate to simulate pure sheet cavities, as long as the sheets do not disintegrate into clouds.

## 2) Mixture models assuming a homogeneous dispersion of bubbles (require $\psi = \Delta_{\text{flow}} / \Delta_{\text{CFD}} \ll 1$ )

Mixture models are typically based on the assumption that the size of a computational cell  $\Delta_{\text{CFD}}$  is sufficiently larger than the diameter of a typical bubble  $\Delta_{\text{flow}}$ . If this assumption is justified, one could model the fluid as dispersed mixture within each computational cell (bubbly flow model). In this case, the temporal evolution of the bubble diameter is often approximated by a modified Rayleigh-Plesset equation (or by simple finite-rate equations). Obviously, the approach is questionable as soon as the size of the bubbles reaches or even exceeds the cell-size of the adopted computational grid. Therefore, these methods are neither designed to simulate clear sheet cavities nor to simulate the collapse of a (resolved) bubble.

## 3) Thermodynamic equilibrium models (no requirement on $\psi$ )

Thermodynamic equilibrium models are based on the assumption that for each computational cell the density  $\rho$  and the internal energy  $e$  determine the condition of aggregation, as well as unknown thermodynamic states, such as pressure and temperature. The evaluation of unknown states requires either closed-form equations or tabulated data. Since thermodynamic equilibrium models are free of intrinsic length and time scales, they provide an interesting option for simulating cavitating flows. If a flow detail (for example a single bubble) is resolved by the applied computational grid, then the thermodynamic equilibrium model implicitly captures the interface and performs comparable to a sharp interface technique. If the grid is too coarse to capture the detail, then the model behaves similar to a mixture approach. As a matter of principal, physical effects such as surface tension or finite-rate evaporation cannot be incorporated into thermodynamic equilibrium models.

Our current research focuses on the assessment of the ability of thermodynamic equilibrium approaches to predict the characteristics of cavitating flows, especially the formation of sheet and cloud cavitation as well as collapsing clouds of vapor bubbles and generated shock waves. In this investigation we evaluate the sensitivity of a thermodynamic equilibrium model with respect to the applied computational grid. In particular, we investigate the collapse characteristics of a cloud of vapor bubbles by resolved simulations and by under-resolved numerical simulations.

## 2. DESCRIPTION OF THE METHODOLOGY

### 2.1 Cloud Generation

We apply a numerical procedure to generate a random distribution of spherical bubbles. Although experimentally observed clouds certainly show a random character, we assume that the following additional properties are reasonable:

1) The “numerical cloud” consists of 125 spherical vapor bubbles with radii between  $R_{\text{min}} \approx 0.70$  mm and  $R_{\text{max}} \approx 1.65$  mm. The average radius is  $R_{\text{av}} \approx 0.95$  mm. The total vapor volume fraction is 5.8% with respect to the small domain.

2) The bubbles do not intersect; the minimum distance between two bubbles is 0.2 mm.

3) We assume that bubbles are larger around the center of the cloud and that they are spaced more densely than at the outer regions

4) The cloud is located within a liquid-filled cubic domain of  $20 \times 20 \times 20$  mm<sup>3</sup> – see **Figure 1**. This domain is embedded into a larger rectangular domain of  $4 \times 4 \times 2$  m<sup>3</sup>. The bottom faces of both domains are coplanar and impermeable for representing a solid wall. The other faces of the outer domain correspond to far-field boundaries.

Since we apply a thermodynamic equilibrium approach, we need to simplify the test-case by neglecting surface tension and non-condensable gas content, and we assume the following properties:

1) The initial pressure  $p_B$  inside the bubbles is equal to the vapor pressure  $p_{\text{sat}} = 2340$  Pa at  $T = 293$  K.

2) The initial pressure within the surrounding liquid satisfies a Laplace law, where the pressure sufficiently far away from the bubbles is  $p_{\infty} = \text{const.} = 40$  bar, and the pressure at the bubble surfaces is equal to the vapor pressure  $p_{\text{sat}} = 2340$  Pa.

3) The velocity field is initially at rest.

4) The initial temperature is  $T = 293$  K.

5) Viscous effects are negligible.

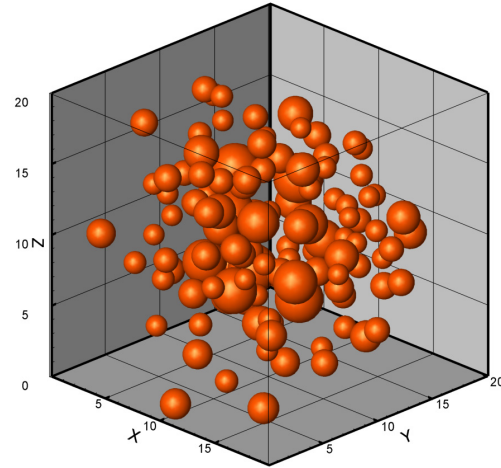


**Figure 1:** Cloud with 125 spherical non-intersecting vapor bubbles within the small cubic domain of  $20^3$  mm<sup>3</sup>. The total vapor volume fraction is 5.8% with respect to the volume of the small domain. The lower boundary at  $z=0$  is modeled as solid wall; the other boundaries are connected to a huge outer domain of  $4 \times 4 \times 2$  m<sup>3</sup> (not shown here).

## 2.2 Discretization of the cloud and applied grids

The simulation of the collapse of the previously described “numerical cloud” requires a discrete representation of the specified properties. We adopt 6 different computational grids to discretize the small domain where the cloud is located. The grids consist of uniform hexahedrons and the resulting numerical resolutions  $\Delta_{\text{CFD}}$  are listed in **table 1**.

	Number of cells	$\Delta_{\text{CFD}}$	$\psi := \Delta_{\text{flow}}/\Delta_{\text{CFD}}$
Grid 1	$220^3 \approx 1.1 \cdot 10^7$	0.09 mm	$\approx 16 - 36$
Grid 2	$110^3 \approx 1.3 \cdot 10^6$	0.18 mm	$\approx 8 - 16$
Grid 3	$55^3 \approx 1.7 \cdot 10^5$	0.36 mm	$\approx 4 - 8$
Grid 4	$28^3 \approx 2.2 \cdot 10^4$	0.71 mm	$\approx 2 - 4$
Grid 5	$14^3 \approx 2.7 \cdot 10^3$	1.43 mm	$\approx 1 - 2$
Grid 6	$7^3 \approx 3.4 \cdot 10^2$	2.86 mm	$\approx 0.5 - 1$

**Table 1:** Properties of the applied computational grids to discretize the small domain.  $\Delta_{\text{CFD}}$  is the cell length;  $\psi$  is the ratio of diameters of the bubbles and the cell length.

On the finest computational grid (Grid 1) each of the smallest bubbles is resolved by at least 2000 cells and each of the largest bubbles is resolved by about 25000 cells.

The analytically defined initial conditions are mapped to the grids by the following approach. First, we detect all computational cells that are either completely inside or completely outside of the bubbles. These cells are marked as “pure state cells”. The remaining cells are necessarily “cut cells” that contain liquid and vapor. In case of a “cut cell” we perform an accurate evaluation procedure to obtain the vapor volume fraction  $\alpha$  within the cell. Since we assume that the initial temperature field is  $T=293$  K within the whole domain, the thermodynamic properties of a cut cell are obtained by tabulated relations  $e=e(\alpha, T)$ ,  $\rho=\rho(\alpha, T)$ ,  $p=p_{\text{sat}}(T)$ . If a “pure state cell” contains vapor, then the thermodynamic properties of vapor at  $T=293$  K and  $p=p_{\text{sat}}(T)$  are prescribed. If a pure cell contains water, then the initial temperature  $T=293$  K is assigned. The initial pressure field is determined by solving a Laplace equation within the complete domain (including the large outer region) where the pressure at the far-field is  $p_{\infty}=40$  bar. Only the pure liquid domain is altered since the properties of cut cells or “pure vapor cells” are kept constant. Once the discrete pressure field is available, the thermodynamic properties are specified by evaluating tabulated relations  $e=e(p, T)$ ,  $\rho=\rho(p, T)$ . The described procedure is employed to provide the initial fields for each computational grid. The resulting discrete representations are shown in **Figure 2**. One horizontal cut plane depicts the initial vapor volume fraction by using continuous coloring, and the remaining cut planes show the vapor volume fraction by using cell center coloring. The colored bottom plane indicates the initial pressure field. It can be seen that the bubble shapes are sharply represented by the fine grids 1 and 2, while they are completely under-resolved by the coarse grids 5 and 6. The grids 3 and 4 allow for partial resolution of the bubble shapes.

## 2.3 Numerical Method

We apply our flow simulation code CATUM (CAvitation Technische Universität München [1, 2]), which is a density based finite volume method employing a Low-Mach-number consistent flux function and an explicit time marching procedure. The spatial reconstruction of the velocity field is a WENO-3 procedure; density and internal energy are reconstructed by monotonic TVD limiters (“minmod”). Time marching is performed through an explicit low storage 4-step Runge-Kutta method with an optimized stability region. The combination of both methods results in a 2<sup>nd</sup> order numerical approach in space and time for smooth flow while ensuring a sharp representation of discontinuous flow features such as shocks and contact waves. In this investigation we focus on the simulation of inertia-driven effects and wave dynamics wherefore we neglect viscous effects. Hence, the governing equations are the compressible Euler equations.

The working fluids can be characterized by closed-form equations of state, or for complex fluids by look-up tables. In this investigation we use tabulated thermodynamic relations  $p=p(\rho, e)$ ,  $T=T(\rho, e)$ ,  $\alpha(\rho, e)$ . The tables are obtained from the IAPWS database [3] of equilibrium states of water and water vapor. In order to allow for the simulation of shock formation and wave propagation, the compressibility of the fluids (liquid and vapor) is taken into account. Hence, the numerical time step is necessarily proportional to the ratio of the smallest length scale (minimum grid size) and the fastest signal speed ( $\sim$  speed of sound of the liquid).

The phase transition model is based on local equilibrium assumptions for pressure, temperature and specific Gibbs functions.

Previous investigations [4, 5] showed that **CATUM** allows for the reliable prediction of erosion-sensitive areas by 3-D unsteady simulations of compressible cavitating flows including collapse-induced shock formation and propagation.

## 2.4 Simulation of the cloud collapse

The adopted explicit time marching scheme is subject to a numerical constraint on the time-step size (CFL condition). The constraint ensures that even the fastest information (propagating shocks) does not pass more than one computational cell per time step. For the present investigation, the CFL-number is kept constant at  $\text{CFL}=1.4$  (4 stage low storage Runge-Kutta). Hence, the time-step sizes are proportional to the size of the cells of the adopted grid. The finest grid (grid 1) requires a time-step size of  $1.95 \cdot 10^{-8}$  s, while for the coarsest grid (grid 6) the resulting time-step size is  $6.24 \cdot 10^{-7}$  s. The remaining time-step sizes are as follows:  $3.90 \cdot 10^{-8}$  s (grid 2),  $7.80 \cdot 10^{-8}$  s (grid 3),  $1.56 \cdot 10^{-7}$  s (grid 4),  $3.12 \cdot 10^{-7}$  s (grid 5).

We adopt two “numerical pressure transducers” located at the center of the bottom wall. The larger transducer records the average static pressure on an area of  $1 \times 1$  cm<sup>2</sup> while the smaller one covers an area of  $1 \times 1$  mm<sup>2</sup>. Both transducers store the static pressure for each instant in time, resulting in a maximum sampling frequency of  $5.1 \cdot 10^7$  Hz (grid 1).



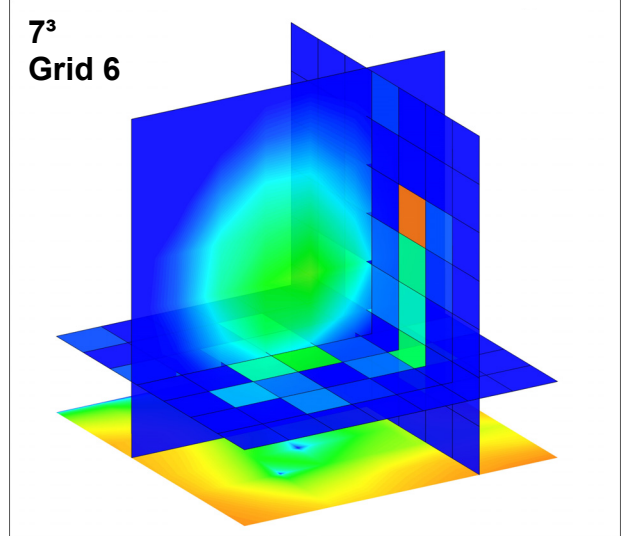
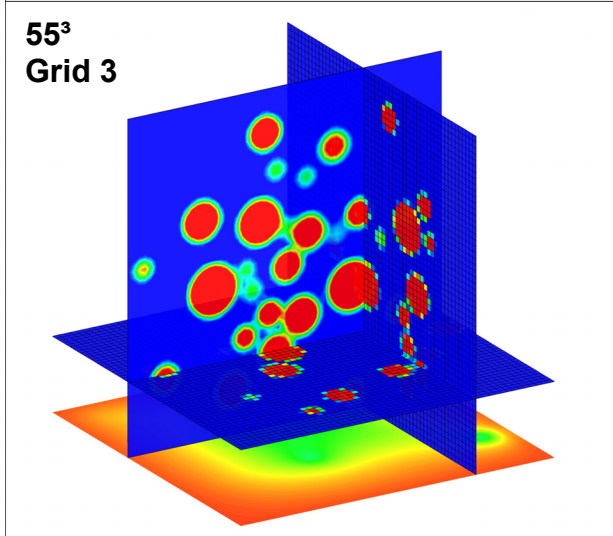
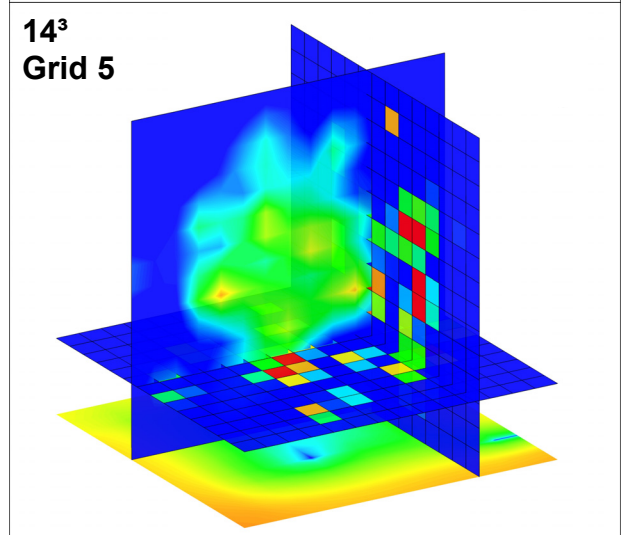
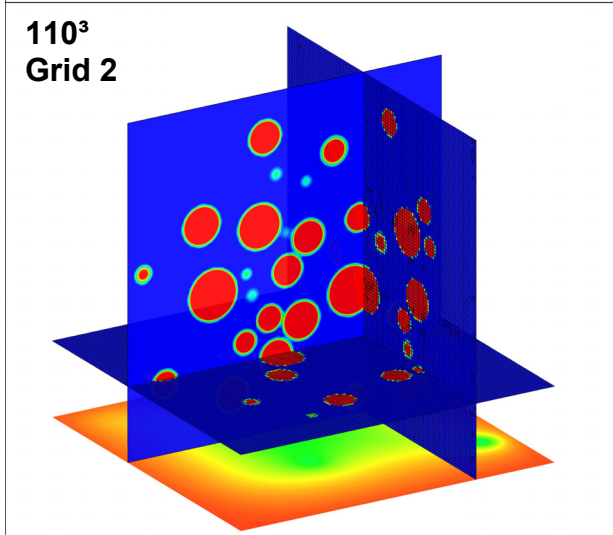
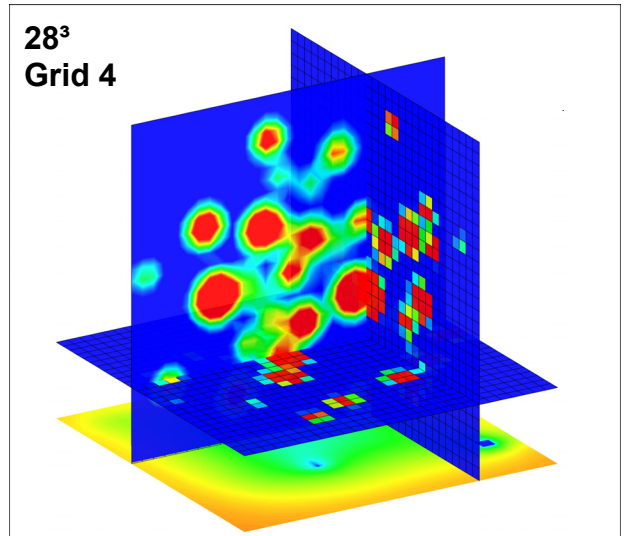
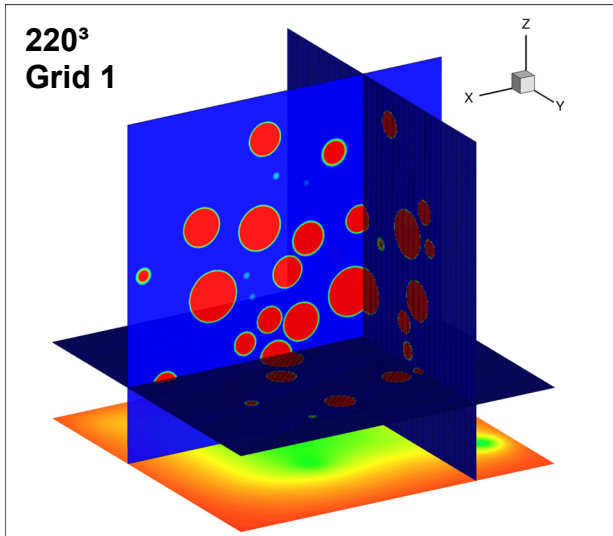


**Figure 2:** Discretization of the cloud by different computational grids. The forward faced plane depicts the vapor volume fraction  $\alpha$  by using continuous coloring (red = pure vapor, blue = pure liquid, other colors represent mixtures). The remaining cut planes are colored by cell value coloring. At the bottom plane, the initial static pressure is depicted.

Aside from the “numerical pressure transducers”, the maximum pressure within the complete flow field during each simulation is monitored. Furthermore, we analyze the time history of the total vapor volume within the domain.

The computations are performed on Intel Nehalem-EP based 8-way nodes and consumed 512 CPU-hours on grid 1, 21 CPU-hours on grid 2, 1 CPU-hour on grid 3, and negligible computation times on the coarse grids.

### 3. ANALYSIS OF THE NUMERICAL RESULTS

The analysis of the simulations focuses on the following characteristics. We evaluate the duration of the collapses by monitoring the total vapor volume. Only the first collapse is taken into account to determine the collapse duration. Since the observed rebounds are relatively weak, this criterion is justified. **Figure 3** depicts the time history of the vapor volume as predicted by the simulations. One observes that the predicted durations agree well for all resolutions. The maximum deviation from the predicted mean collapse duration occurs for grid 3 and is less than  $\pm 6\%$ . **Table 2** provides an overview of the observed collapse durations. Since experimental data are not available for the specific cloud and the specific boundary conditions, we utilize a simplified analytical estimate to evaluate the order of magnitude of the collapse duration. Therefore, we consider the Besant problem (collapse of a single spherical bubble within an infinitely large domain) of an “equivalent bubble”. Based on the initial vapor volume of the cloud we obtain the radius  $R_{\text{equiv}}=4.8$  mm of a single large bubble with equal vapor volume. This radius is applied to estimate the Rayleigh time (time required for the complete collapse, no gas content, no surface tension, incompressible liquid, spherical collapse). One obtains the analytical expression [6]

$$\tau_{\text{tc}} \approx 0.915 \cdot R_0 \cdot \sqrt{\frac{\rho_L}{p_\infty - p_v}}$$

where  $\tau_{\text{tc}}$  is the collapse duration,  $R_0$  the initial bubble radius,  $\rho_L$  the constant density of the liquid,  $p_\infty$  the constant far-field pressure and  $p_v$  the constant vapor pressure within the bubble. Using  $R_0=R_{\text{equiv}}=4.8$  mm,  $p_\infty=40$  bar,  $\rho_L=1000$  kg/m<sup>3</sup> and  $p_v=0.023$  bar one finds a collapse duration of  $\tau_{\text{tc}}=6.94 \cdot 10^{-5}$  s, which agrees well with the numerically predicted durations.

In the following, the instantaneous maximum pressures within the flow field as well as at the bottom wall of the small domain are analyzed. **Table 2** shows the grid dependence of the maximum pressure within the domain. We observe that the instantaneous maximum pressure within the domain varies by approximately two orders of magnitude. However, the maximum pressure at the wall shows only a weak variation of a factor of about two (see **Figure 4**). To examine the numerical predictions we consider the propagation of a linear spherical pressure wave. The amplitude of a linear spherical wave decays inversely proportional to the radius of the wave front [7]. As soon as the wave impinges on the wall, it is reflected and the amplitude after the impingement is about twice the amplitude before the impingement.

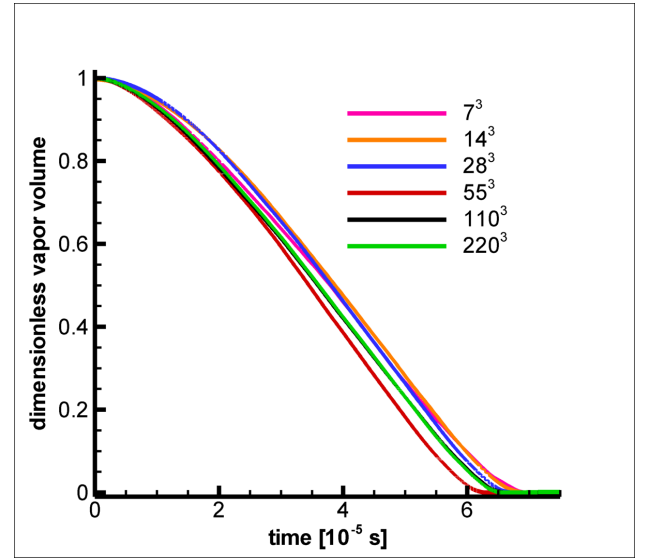


**Figure 3:** Time history of the dimensionless vapor volume as obtained with 6 different resolutions of the small domain.

	$P_{\text{max}}$ (domain)	$P_{\text{max}}$ (wall)	Collapse duration
Grid 1	$3.14 \cdot 10^9$ Pa	$4.1 \cdot 10^7$ Pa	$6.5 \cdot 10^{-5}$ s
Grid 2	$1.17 \cdot 10^9$ Pa	$3.9 \cdot 10^7$ Pa	$6.6 \cdot 10^{-5}$ s
Grid 3	$0.63 \cdot 10^9$ Pa	$3.6 \cdot 10^7$ Pa	$6.3 \cdot 10^{-5}$ s
Grid 4	$0.34 \cdot 10^9$ Pa	$3.5 \cdot 10^7$ Pa	$6.7 \cdot 10^{-5}$ s
Grid 5	$0.12 \cdot 10^9$ Pa	$2.8 \cdot 10^7$ Pa	$6.9 \cdot 10^{-5}$ s
Grid 6	$0.07 \cdot 10^9$ Pa	$1.9 \cdot 10^7$ Pa	$7.0 \cdot 10^{-5}$ s

**Table 2:** Comparison of the maximum pressure within the flow field as well as at the wall (small sensor) and duration of the collapse as observed for different numerical resolutions.

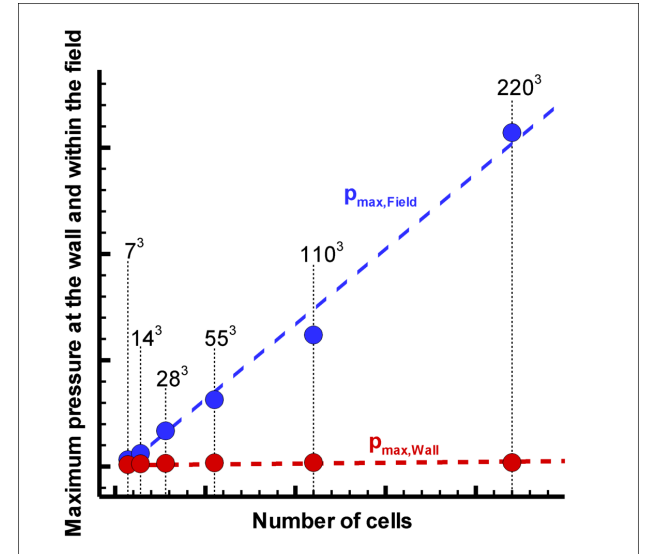


**Figure 4:** Scaling of the maximum pressures within the flow field (blue) and at the wall (red) with respect to the applied grid resolution.



By combining the linear decay law and the linear wave reflection at solid walls we obtain a (strongly) simplified relation of the maximum wall pressure to the maximum pressure within the flow field. We assume that the maximum wall pressure  $p_{\text{wall}}$  is the result of a reflected spherical wave at a distance  $D$  from its origin. Since the initial radius of the wave front cannot be smaller than half of the cell length  $\Delta_{\text{CFD}}$ , we obtain the relation

$$\frac{p_{\text{max,Field}}}{p_{\text{max,Wall}}} \approx \frac{D}{\Delta_{\text{CFD}}}.$$

Assuming that the collapse is perfectly focused into one fixed point independently of the applied grid, one would expect that  $D$  is approximately constant (if nonlinear effects are negligible). By evaluating  $D$  we find the following distances of the assumed focus point to the bottom wall:  $D=7.0$  mm (grid 1),  $D=5.5$  mm (grid 2),  $D=6.4$  mm (grid 3),  $D=6.9$  mm (grid 4),  $D=6.1$  mm (grid 5),  $D=10.6$  mm (grid 6). All estimates are in a reliable range. Through this simple analysis we demonstrate that the increase of the observed maximum pressure within the flow field is not a numerical artifact but a physical property that is well captured by the applied methodology.

**Figure 5** shows the output of the large pressure sensor (sensor area  $1 \times 1 \text{ cm}^2$ , located at the center of the bottom wall). The black line is the signal obtained for grid 1 and the signal obtained with grid 6 is shown in red. The numerical sampling frequencies are 51 MHz (grid 1) and 1.6 MHz (grid 6). One can observe that the peak is more pronounced with the fine grid and the high temporal resolution. In the present case, the duration of the shock-induced peak pressure is only about  $5 \mu\text{s}$  (grid 1). On the coarse grid 6 the amplitude of the peak is reduced and the peak is smeared. In order to compare the transducer signals for all 6 grid resolutions we evaluate the time integral of the pressure. Three evaluations are performed:

$$\text{Impulse Strength 1} := \int_0^{10^{-4}} p dt$$

$$\text{Impulse Strength 2} := \int_{5 \cdot 10^{-5}}^{8.5 \cdot 10^{-5}} p dt$$

$$\text{Impulse Strength 3} := \int_0^{10^{-4}} (p \geq 80 \text{ bar}) dt$$

The first value corresponds to the impulse strength during  $10^{-4}$  seconds and covers the complete collapse. Impulse strength 2 corresponds approximately to the time interval where the collapse-induced peak pressure is observed. The third value is obtained by integrating the pressure during the time interval where the pressure exceeds 80 bars (twice the far-field value). Although the specific threshold is somewhat arbitrarily chosen, it should allow for comparison of the pressure peaks. The obtained results are listed in **table 3**.

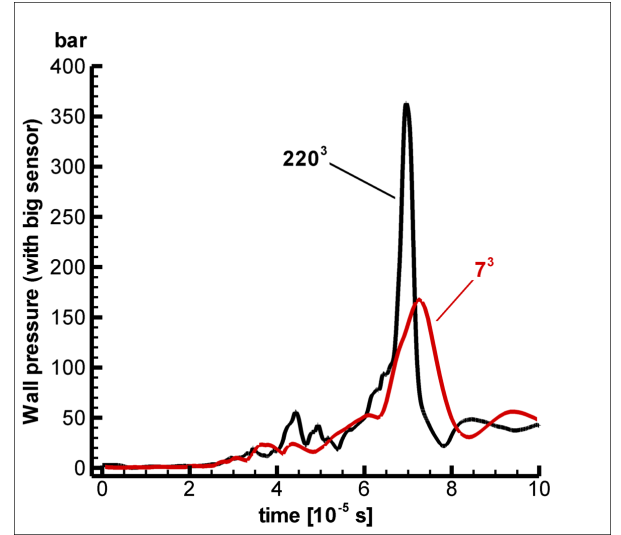


**Figure 5:** Comparison of the wall pressure as recorded by the numerical pressure sensor (area  $1 \times 1 \text{ cm}^2$ ) by applying grid 1 (finest) and grid 6 (coarsest).

	Imp. Strength 1	Imp. Strength 2	Imp. Strength 3
Grid 1	$3.94 \cdot 10^2 \text{ Pa} \cdot \text{s}$	$2.86 \cdot 10^2 \text{ Pa} \cdot \text{s}$	$1.82 \cdot 10^2 \text{ Pa} \cdot \text{s}$
Grid 2	$3.90 \cdot 10^2 \text{ Pa} \cdot \text{s}$	$2.79 \cdot 10^2 \text{ Pa} \cdot \text{s}$	$1.77 \cdot 10^2 \text{ Pa} \cdot \text{s}$
Grid 3	$3.77 \cdot 10^2 \text{ Pa} \cdot \text{s}$	$2.79 \cdot 10^2 \text{ Pa} \cdot \text{s}$	$2.12 \cdot 10^2 \text{ Pa} \cdot \text{s}$
Grid 4	$3.94 \cdot 10^2 \text{ Pa} \cdot \text{s}$	$2.94 \cdot 10^2 \text{ Pa} \cdot \text{s}$	$1.99 \cdot 10^2 \text{ Pa} \cdot \text{s}$
Grid 5	$3.81 \cdot 10^2 \text{ Pa} \cdot \text{s}$	$2.83 \cdot 10^2 \text{ Pa} \cdot \text{s}$	$1.84 \cdot 10^2 \text{ Pa} \cdot \text{s}$
Grid 6	$3.74 \cdot 10^2 \text{ Pa} \cdot \text{s}$	$2.76 \cdot 10^2 \text{ Pa} \cdot \text{s}$	$1.84 \cdot 10^2 \text{ Pa} \cdot \text{s}$

**Table 3:** Comparison of the impulse strength as obtained with three different evaluation procedures. Criteria are specified above.

Finally, we present a series of snapshots (**Figure 6**) of the collapse as predicted by using grid 1. The snapshots do not show equidistant time instants but provide an overview about the observed physical processes. **Pic 1** of **Figure 6** shows the initial distribution of the bubbles, together with the static pressure on the wall. In **Pic 2** a relatively isolated bubble has collapsed and a spherical shock is indicated by its footprint on the wall. **Pic 3** shows partially deformed bubbles and a slight increase of the pressure on the wall. In **Pic 4** some of the bubbles are impinged by liquid jets (thus forming tori). **Picture 5** is the time instant of the final collapse and the occurrence of the maximum pressure within the complete flow field. However, the maximum pressure at the wall is observed slightly afterwards in **Pic 6**. Here, already rebounding vapor structures are formed. The rebounding structures reach the maximum vapor volume at **Pic 8** and collapse again at **Pic 10**. **Picture 11** corresponds to the second rebound and **Pic 12** shows the final stage after the third collapse.

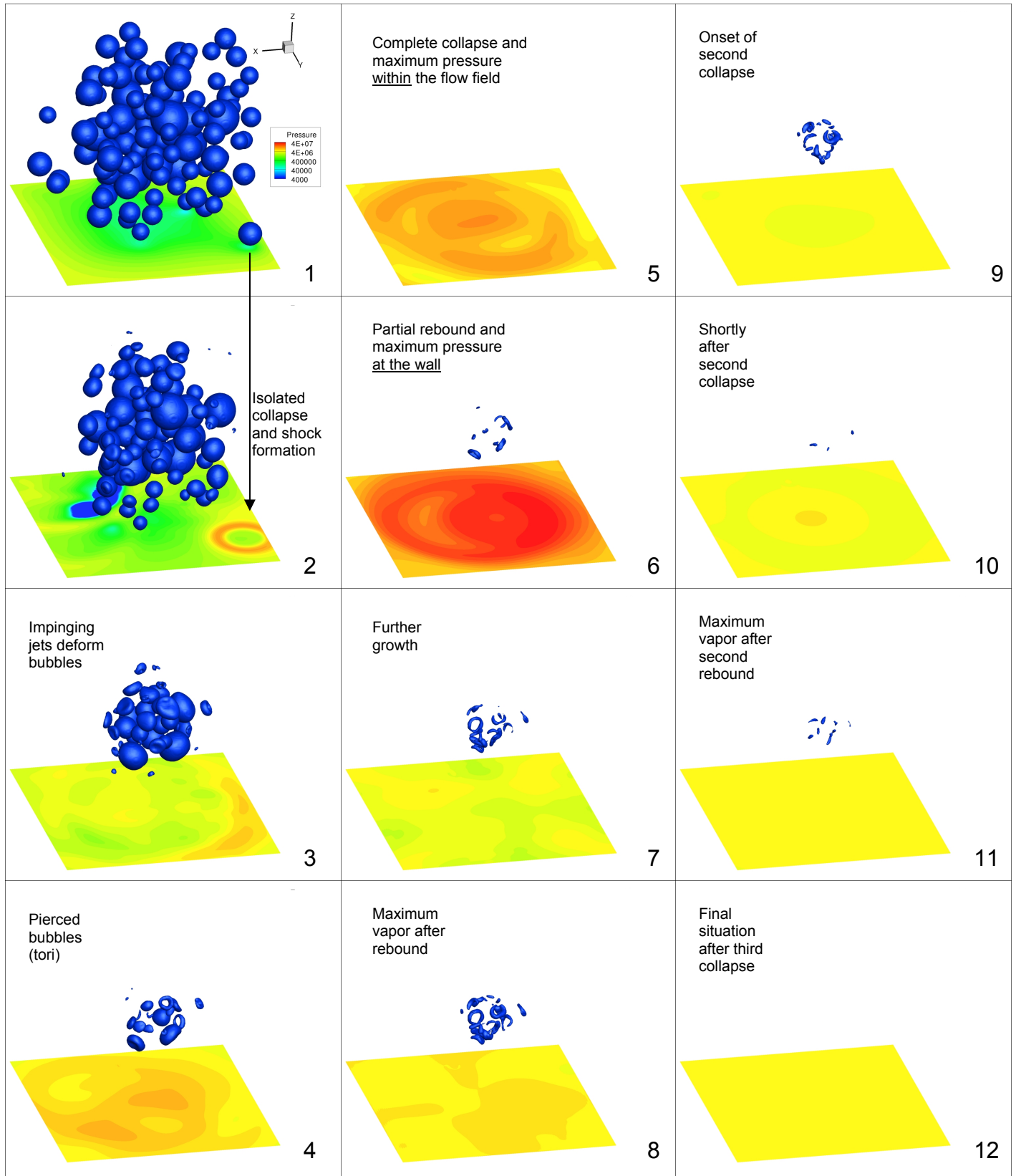


**Figure 6:** Snapshots of the numerically predicted collapse of the cloud (grid 1 was used).

Time instants:  $t_1=0 \mu s$ ,  $t_2 \approx 28 \mu s$ ,  $t_3 \approx 52 \mu s$ ,  $t_4 \approx 60 \mu s$ ,  $t_5 \approx 64 \mu s$ ,  $t_6 \approx 68 \mu s$ ,  $t_7 \approx 80 \mu s$ ,  $t_8 \approx 84 \mu s$ ,  $t_9 \approx 90 \mu s$ ,  $t_{10} \approx 96 \mu s$ ,  $t_{11} \approx 102 \mu s$ ,  $t_{12} \approx 116 \mu s$ .

#### 4. DISCUSSION AND FUTURE PROSPECTS

Our numerical investigation of the collapse characteristics of a cloud of bubbles leads to the following conclusions.

- 1) The combination of a thermodynamic equilibrium model with a density based finite volume method enables the simulation of collapsing vapor bubbles including the subsequent formation of strong shock waves. We suppose that taking compressibility effects into account and providing high temporal resolution are necessary to investigate cloud collapse phenomena.
- 2) The influence of the spatial resolution on the collapse duration, the maximum pressure at the wall and on the impulse strength is examined. We conclude that the thermodynamic equilibrium model allows for reliable predictions of collapse phenomena even if the spatial resolution is insufficient to resolve single bubbles. The obtained maximum pressure at the wall, the impulse strength and the collapse duration are nearly independent of the applied spatial resolution. This finding is of great importance since it substantiates the methodologies investigated in [4, 5] and [8, 9] to predict erosion-sensitive areas.
- 3) Although viscosity, surface tension, non-condensable gas content and non-equilibrium physics are neglected, detailed features of cloud collapses are predictable. A comparison of our results with a sharp interface method is planned.

Our current research focuses on the prediction of cavitation erosion by means of numerical simulations. We investigate break-up patterns of unstable sheet cavitation [2] as well as flow features that may be responsible for cavitation erosion. Aside of cavitating water flows [5] we consider cavitation of Diesel-like fluids in high-speed micro channels [8, 9]. Recent results promisingly indicate that the reliable prediction of cavitation erosion could be possible [8, 9]. Additional numerical investigations of the experiments discussed in [10, 11] are currently performed.

Further numerical developments will be the inclusion of viscous effects and of non-condensable gas content.

#### REFERENCES

- [1] Schnerr, G.H., Sezal, I.H., Schmidt, S.J., “*Numerical Investigation of Three-dimensional Cloud Cavitation with Special Emphasis on Collapse Induced Shock Dynamics*”, Physics of Fluids, Vol. 20, Issue 4, 040703, 2008.
- [2] Schmidt, S.J., Thalhamer, M., Schnerr, G.H., “*Inertia Controlled Instability and Small Scale Structures of Sheet and Cloud Cavitation*” Proc. 7th CAV 2009 - 7th International Symposium on Cavitation, Ann Arbor, Michigan, USA, 16.8.- 21.8.2009, paper 17, CD-ROM publication, 2009.
- [3] The International Association for the Properties of Water and Steam, <http://www.iapws.org/>
- [4] Schmidt, S.J., Sezal, I.H., Schnerr, G.H., Thalhamer, M., “*Numerical Analysis of Shock Dynamics for Detection of Erosion Sensitive Areas in Complex 3-D Flows*”, Proc. WIMRC Cavitation Forum 2008, pp. 107-120, July 7 - 9, 2008, Warwick, UK, 2008.
- [5] Schmidt, S.J., Mihatsch, M., Thalhamer M., Egerer, C., Hickel, S., Adams, N.A., “*Assessment of Erosion Sensitive Areas via Compressible Simulation of Unsteady Cavitating Flows*”, International Workshop on ADVANCED EXPERIMENTAL AND NUMERICAL TECHNIQUES FOR CAVITATION EROSION PREDICTION, Grenoble, France, 1.3-2.3.2011, Post-Workshop CD.
- [6] Franc, J.-P., Michel, J.-M., “*Fundamentals of Cavitation*”, Kluwer Academic, Dordrecht, 2004
- [7] Whitham, G.B., “*Linear and Nonlinear Waves*”, John Wiley and Sons, New York, 1999
- [8] Mihatsch, M., Schmidt, S.J., Thalhamer, M., Adams, N.A., Skoda, R., Iben, U., “*Collapse Detection in Compressible 3-D Cavitating Flows and Assessment of Erosion Criteria*”, WIMRC Cavitation Forum 2011, Warwick, UK.
- [9] Skoda, R., Iben, U., Morozov, A., Mihatsch, M., Schmidt, S.J., Adams, N.A., “*Numerical simulation of collapse induced shock dynamics for the prediction of the geometry, pressure and temperature impact on the cavitation erosion in micro channels*”, WIMRC Cavitation Forum 2011, Warwick, UK.
- [10] Iben, U., Morozov, A., Winklhofer E., Skoda, R., “*Optical investigations of cavitating flow phenomena in micro channels using a nano second resolution*”, WIMRC Cavitation Forum 2011, Warwick, UK.
- [11] Franc, J.P., Riondet, M., “*Incubation Time and Cavitation Erosion Rate of Work-Hardening Materials. CAV2006*”, Wageningen, The Netherlands, September 2006.

# INERTIAL CAVITATION BUBBLE IN PROXIMITY TO A QUIESCENT BUBBLE

BING HUI TERENCE GOH

*NUS Graduate School of  
Integrative Sciences and  
Engineering, Singapore*

EVERT KLASEBOER

*Institute of High Performance  
Computing, Singapore*

BOO CHEONG KHOO\*

*Department of Mechanical  
Engineering, National University of  
Singapore, Singapore  
&  
Singapore MIT Alliance, Singapore*

\*mpekbc@nus.edu.sg

## ABSTRACT

The problem of an inertia cavitation bubble collapsing close to an initially stationary bubble is numerically investigated by means of a boundary element method (BEM) model. Results are obtained by varying the quiescent bubble radius and centre-to-centre distance between the bubbles. We deduce that the occurrence of bubble jet(s) and the corresponding jet velocity are highly dependent on these parameters. Our observations are compared with experiments of spark-generated bubble and a neighbouring quiescent bubble. We report a good degree of coherency between the empirical results and our numerical predictions.

## NOMENCLATURE

$c$	Solid angle on $S$
$G$	Green function
$p$	Pressure just outside bubble
$p_g$	Pressure inside bubble
$p_v$	Vapour pressure
$p_0$	Reference pressure
$S$	Bubble surface
$t$	Time
$\mathbf{u}$	Velocity
$V$	Volume of bubble
$V_0$	Initial volume of bubble
$\nabla$	Gradient operator, $\nabla = (\partial/\partial x, \partial/\partial y, \partial/\partial z)$
$\gamma$	Ratio of specific heats, $\gamma = C_p/C_v$
$\phi$	Velocity potential
$\rho$	Density of water

## 1. INTRODUCTION

Cavitation bubbles have been demonstrated to behave differently when in proximity to different materials. For example if a bubble oscillates beside an interface, jets towards or away from the interface may occur [1]. Multiple bubbles may also generate jets towards or away from each other depending on their oscillation phase difference [2]. However, the behaviour of an inertia cavitation bubble near an equilibrium bubble is not extensively studied upon. This problem is pertinent to a wide range of applications such as ultrasound treatments in the biomedical field and damage to industrial propellers and pumps

due to cavitation. The interaction of the oscillating bubbles with stationary bubbles present in these systems may induce strong jets and possibly lead to undesirable collateral damage to neighbouring structures. Thoroddsen et al. [3] reported micro-jets from stationary micro-bubbles on a liquid drop surface by laser-produced cavitation within the drop. Our motivation is therefore to predict the occurrence of the jets through the stationary bubble induced by a nearby cavitation bubble, and the jet velocities, according to the bubbles' separation, and their relative sizes.

## 2. METHODOLOGY

An axisymmetric boundary element method was used based on the potential flow theory (since the phenomena investigated are basically inertia controlled). It transforms the Laplace equation ( $\nabla^2 \phi = 0$ ) for the velocity potential in a fluid domain to a surface integral as:

$$c\phi + \int_S \phi \frac{\partial G}{\partial n} dS = \int_S G \frac{\partial \phi}{\partial n} dS. \quad (1)$$

Here,  $G$  and  $S$  comprises of two parts in this work, the oscillating bubble surface and the stationary bubble surface.  $\partial/\partial n = \mathbf{n} \cdot \nabla$  represents the normal derivative on the surface  $S$  ( $\partial\phi/\partial n$  is the normal velocity, where the velocity itself is given by  $\mathbf{u} = \nabla\phi$ ). On both bubble surfaces, the potential is updated at each time step using the Bernoulli equation by setting the pressure just outside each bubble surface equal to the pressure inside each bubble,  $p = p_g$ , as:

$$\rho \frac{D\phi}{Dt} = p_0 + \frac{\rho}{2} |\nabla\phi|^2 - p_g. \quad (2)$$

For simplicity, surface tension and gravity effects have been neglected. The material derivative is defined as  $D/Dt = \partial/\partial t + \mathbf{u} \cdot \nabla$  (the bubbles follow the flow). The reference pressure is  $p_0 = 1$  bar. More information concerning the numerical details can be found in Wang *et al.* [4]. The

pressure inside the oscillating bubble is assumed to follow an adiabatic law as

$$p_{g,o} = p_{g,o0} (V_{o,0} / V_o)^\gamma + p_v, \quad (3)$$

where  $V_o$  and  $V_{o,0}$  are the volume and the initial volume of the oscillating bubble. The initial pressure of the oscillating bubble is taken as  $p_{g,o0} = 100 (p_0 - p_v)$  where the vapour pressure  $p_v$  is chosen as 0 bar unless otherwise specified. The ratio of specific heats  $\gamma = 1.25$  is chosen to be similar as the value for an explosion bubble [5-6]. The initial radius of the bubble is chosen to be 0.1485 times the maximum bubble radius in order to get a maximum dimensionless bubble radius of about 1.00 for the chosen values of  $\gamma$  and  $p_{g,o0}$ . For the stationary bubble the pressure is also assumed to behave adiabatically as

$$p_{g,s} = p_0 (V_{s,0} / V_s)^\gamma, \quad (4)$$

$V_s$  and  $V_{s,0}$  are the instantaneous volume and the initial volume of the initially stationary bubble. A time discretization of eqn. (2) is used to obtain the potential on each bubble surfaces for the next time step (assuming the right hand side of eqn. (2) to be known from the previous time step). 51 nodes were used on each bubble. The unknown normal velocity can hence be computed using eqn. (1). To update the positions of each bubble surface, the velocity vector constructed from the normal velocity  $\partial\phi/\partial n$  and the tangential velocity (obtained from the distribution of the potential on the bubble surface) is used.

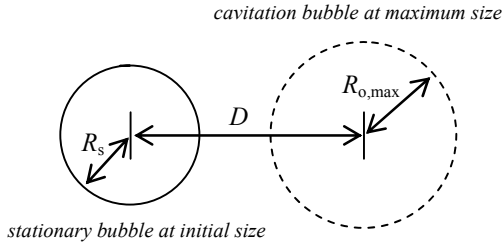


Fig. 1. Schematic diagram of problem setup

Seen above in Fig. 1, we define the initial distance between the centres of the two bubbles as  $D$ , the initial bubble radius of the stationary bubble as  $R_s$  and the maximum bubble radius of the oscillating bubble as  $R_{o,max}$ , then we can define two dimensionless distances as:

$$D' = D / R_{o,max}, \quad (5)$$

&

$$R'_s = R_s / R_{o,max}. \quad (6)$$

From a dimensional analysis [7], time is scaled as  $t' = \frac{t}{R_{o,max}} \sqrt{\frac{p_0 - p_v}{\rho}}$  and the velocity as  $u' = u \sqrt{\frac{\rho}{p_0 - p_v}}$ . This implies that if a jet is generated, its velocity does not depend on  $R_{o,max}$  whereas the timing of the problem does. This allows us to present our results of jet velocity in m/s.

### 3. RESULTS

To determine the interaction physics involved between a cavitation bubble and nearby quiescent bubble, we conduct simulations for a variance of initial stationary bubble size  $R'_s$  and the bubbles' centre-to-centre distance  $D'$ .

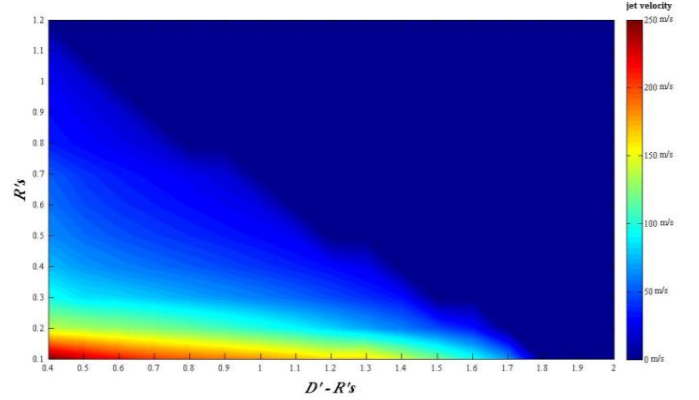


Fig. 2. Plot of  $R'_s$  against  $D' - R'_s$  with corresponding predicted jet velocities

Under certain parameters, we observe a jet from the stationary bubble away from the cavitation bubble at varying velocities. In Fig. 2, we present the jet velocity as a function of scaled initial stationary bubble radius  $R'_s$ , and shortest distance between the initial stationary bubble surface and the cavitation bubble centre, represented by  $(D' - R'_s)$ . The dark blue shaded region encompassing the top right hand half of the figure signifies that no jet is observed (0 m/s) from the stationary bubble under the corresponding parameters. Conversely, a jet with velocities of up to 250 m/s (region shaded in red) is predicted in the alternately coloured area.

It is shown that the stationary bubble jet due to nearby cavitation is only for comparable or smaller quiescent bubble with respect to the maximum dimension of the cavitation bubble. We also notice that with increasing  $R'_s$ , the  $(D' - R'_s)$  range whereby a jet is observed decreases almost linearly, until a certain critical radius,  $R'_{s,crit} = 1.20$ , where the budding jet no longer exits the stationary bubble. For example, when  $R'_s = 0.10$ , the maximum  $(D' - R'_s)$  for an observable jet in our simulations is 1.70. When  $R'_s = 1.00$  however, the maximum  $(D' - R'_s)$  for an observable jet in our simulations decreases to 0.50. Further, we also notice that for  $R'_s \leq 0.30$ , there is minimal disturbance to the spark bubble (i.e. the spark bubble collapses spherically).

For  $(D' - R'_s) < 0.40$ , the bubbles' surface are almost in contact during the expansion of the cavitation bubble with which coalescence may occur. As such, the results are omitted for the purpose of this study. For the remaining  $0.40 < (D' - R'_s) < 1.80$ , if there is a marked jet from the stationary bubble, the jet velocity increases with decreasing  $R'_s$ . At  $(D' - R'_s) > 1.80$  in our study, no jet is observed. Rearranging, we deduce that there will no apparent jet for  $D$  greater than approximately twice of  $R_{o,max}$  (i.e. the maximum diameter of the cavitation bubble).

To validate our predictions, we compare our results with representative experiments describing the jetting and non-jetting scenarios respectively. In these experiments, the cavitation bubble is generated by electrical discharge through a spark in water and the quiescent air bubble is held stationary in place by encapsulating it in a silicone oil droplet. For spark-generated



bubbles, it is known that the vapour pressure can be significant [7,8]. To match the cavitation bubble's expansion and collapse, we take  $p_v$  as 0.47 bar for our simulations.

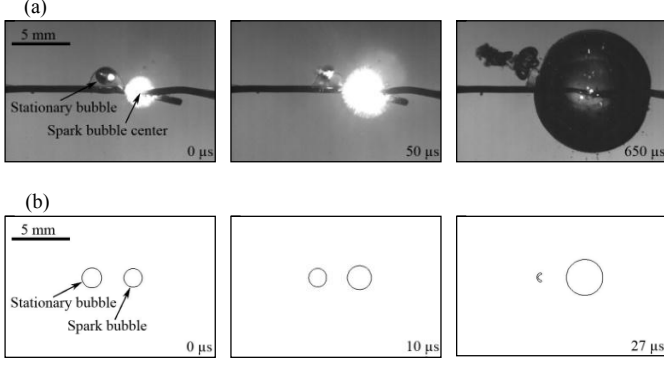


Fig. 3. Numerical comparison with experiment case 1: bubble jet observed (Top (a): experiment results, bottom (b): our numerical results).

The first experimental results of interest have the following parameters:  $R_{o,max} = 5.15$  mm,  $R'_s = 0.16$ ,  $D' = 0.67$ . Fig. 3a and Fig. 3b show the experimental observations and numerical predictions of the jet formation respectively. At 650  $\mu$ s in the experiments, the cavitation bubble reaches its maximum size. At 20 000 frames per second (fps), the experiment shows that a jet has departed the stationary bubble surface in the direction away from the cavitation bubble on the second frame at 50  $\mu$ s. We conduct numerical simulations with the same parameters and compute the respective dimensional time for better comparison. We can predict from Fig. 2 that a high velocity jet will leave the stationary bubble. Indeed, we notice that the jet occurs at 27  $\mu$ s as in Fig. 3b. This seems consistent with the experiment although it is unfortunate that there is a lack of experimental images taken at a higher fps to identify the actual time of jetting.

The next set of experimental results are obtained with these parameters:  $R_{o,max} = 4.81$  mm,  $R'_s = 0.20$ ,  $D' = 2.08$ . Fig. 4a shows experimental observations and this time, the stationary bubble does not generate a jet, but develops into a bean-like shape (e.g. 400  $\mu$ s frame) instead. Some protrusions on the left hand side of the stationary bubble can be seen at the 900  $\mu$ s frame that develops from 750  $\mu$ s (when the cavitation bubble reaches its maximum size). During the collapse of the spark bubble, the smaller bubble starts to disintegrate and is also slightly attracted towards the spark bubble. In Fig. 4b, the corresponding numerical simulations are shown. During the expansion of the spark bubble, the quiescent bubble shows the beginning of a jet formation, this jet does not develop further, but stops halfway within the bubble instead. The bubble then starts to develop a protrusion at the left hand side (750  $\mu$ s and 900  $\mu$ s frames). We notice that this protrusion disappears at time greater than 950  $\mu$ s both from the experiment and numerical simulations. Similar to the experiments, the left bubble grows slightly in volume when the spark bubble has reached its maximum size. This is due to the fact that the pressure in the spark bubble becomes very low. The pressure in the surrounding fluid near the spark bubble also will become lower, resulting in the observed volume oscillation of the left bubble. The closing

in movement of the stationary bubble during the collapse of the cavitation bubble is also evident in the Fig. 4b.

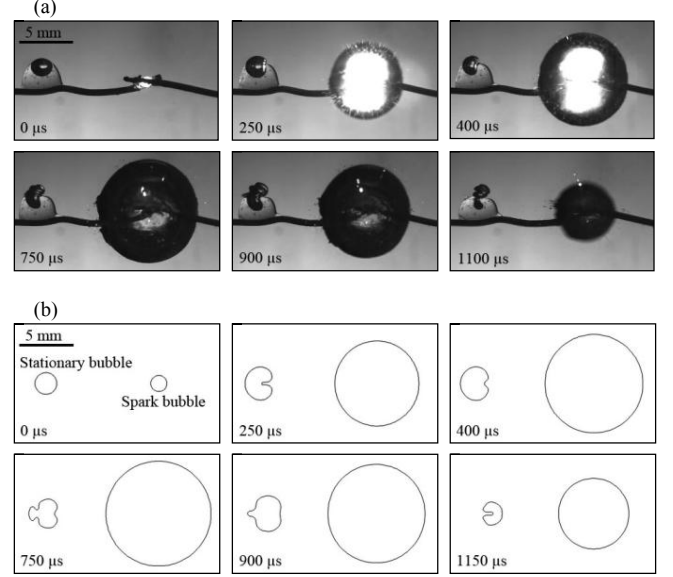


Fig. 4. Numerical comparison with experiment case 2: no bubble jet observed (Top (a): experiment results, bottom (b): our numerical results).

#### 4. DISCUSSIONS AND CONCLUSION

With BEM numerical simulations for different initial stationary bubble size and distance away from the cavitation bubble, we present a comprehensive plot to predict the occurrence of a stationary bubble jet and its velocity. Our results show that for an initial stationary bubble radius lesser than the critical ( $R'_{s,crit} = 1.20$ ), a jet will develop and exit the stationary bubble at the direction away from the nearby cavitation bubble. It was also seen that the velocity of this becomes higher when  $D'$  and/or  $R'_s$  becomes smaller. The jet velocity can reach up to 250 m/s or possibly higher for small stationary bubbles in proximity with a cavitation bubble. Also, if the two bubbles are separated at a centre-to-centre distance greater than the maximum cavitation bubble diameter ( $D > 2 R_{o,max}$ ), no jet from the stationary bubble can be observed.

Comparing the current numerical results with selected experimental results concerning the interaction of a stationary bubble with an oscillating bubble, it does appear that the theoretical framework and our numerical model correctly describe the physics of the problem as the experimental results are consistent with our numerical predictions. It should be noted that the shockwave that is being emitted from the bubble is not taken into account in the model. In summary, the required conditions to avoid the jetting phenomenon are either ( $R'_s \geq R'_{s,crit}$ ) or ( $D > 2 R_{o,max}$ ).

These observations could have some important practical implications. For example, we now have an understanding of the conditions required to prevent collateral damage in bio-applications whereby ultrasonically generated bubbles may induce jets to form on nearby stationary bubbles.

## REFERENCES

1. Blake J.R. and Gibson D.C. (1981). Growth and collapse of a vapour cavity near a free surface. *J. Fluid Mech.* **111**, 123-140.
2. Fong S.W, Adhikari D, Klaseboer E. and Khoo B.C. (2009). Interactions of multiple spark-generated bubbles with phase differences. *Exp. Fluids* **46**, 705-724.
3. Thoroddsen S.T, Takehara K, Etoh T.G. and Ohl C.-D. (2009). Spray and microjets produced by focusing a laser pulse into a hemispherical drop. *Physics of Fluids* **21**, 112101.
4. Wang Q.X, Yeo K.S, Khoo B.C. and Lam K.Y. (1996). Strong interaction between buoyancy bubble and free surface. *Theor. Comput. Fluid Dyn.* **8**, 73-88.
5. Cole R.H. (1948). Underwater explosions. *Princeton University Press*, New Jersey.
6. Lee M., Klaseboer E. and Khoo B.C. (2007). On the boundary integral method for the rebounding bubble. *J. Fluid Mech.* **570**, 407-429.
7. Turangan C.K, Ong G.P, Klaseboer E. and Khoo B.C. (2006). Experimental and numerical study of transient bubble-elastic membrane interaction. *J. Appl. Phys.* **100**, 054910.
8. Buogo S. and Cannelli G.B. (2002). Implosion of an underwater spark-generated bubble and acoustic energy evaluation using the Rayleigh model. *J. Acoust. Soc. Am.* **111**, 2594-2600.